Particle Orbit Analysis under Equilibrium Configuration for Evaluating the Orbit Current Distribution driven by Electron Cyclotron Heating on QUEST

エムディ, マハブブ, アラム

https://doi.org/10.15017/1866333

出版情報：九州大学, 2017, 博士（学術）, 課程博士
バージョン：
権利関係：

Particle Orbit Analysis under Equilibrium Configuration for Evaluating the Orbit Current Distribution driven by Electron Cyclotron Heating on QUEST

（QUEST における電子サイクロトロン加熱による駆動プラズマ

電流分布評価のための平衡配位での粒子軌道解析）

Doctoral Thesis

2017

By

MD MAHBUB ALAM

（エムディ　マハブブ　アラム）

Abstract

Radio frequency (RF) waves have been widely used for the non-inductive plasma current drive. Among all the RFs, the electron cyclotron heating and current drive (ECH/CD) is one of the intense methods of non-inductive plasma current drive. The plasma sustainment with RF or ECH waves is a key issue for the steady state operation in the tokamak configuration. The plasma was sustained for more than 2 hours by the ECH/CD non-inductive method in the Q-shu University experiment with steady-state spherical tokamak (QUEST). The ECH waves accelerated the electrons with the Doppler-shifted electron cyclotron resonance (ECR) interactions, and effectively ramped and sustained the plasma current non-inductively for long discharge duration.

In the QUEST, 28 GHz and 8.2 GHz ECH waves have been used to attain the plasma current start-up and sustainment. The plasma current was generated with the abundant high-energetic electrons in the ECH/CD plasmas. The plasma current generation is strongly related to the ECR conditions and confinements of the electrons in the magnetic field. The plasma current fitting analyses for the ECH/CD plasmas showed that the plasma current existed in the open magnetic fields outside the last closed flux surface (LCFS). In this thesis, the guiding center orbits of the ECR electrons were calculated and analyzed under equilibrium magnetic configuration to consider the current distribution outside the LCFS. A framework with several sets of calculation codes accordingly for various theoretical models was developed with the EFIT (Equilibrium Fitting) plasma equilibrium to calculate and analyses guiding center orbits as well as to evaluate orbit current distribution. The plasma equilibrium and shaping calculated by the EFIT code were properly taken into account for the orbit analyses and the current evaluation, but the evaluated current was not included in the plasma equilibrium and shaping self-consistently.

The guiding center orbits of the resonant electrons were calculated and analyzed for the 8.2 GHz ECH waves in non-relativistic and relativistic ECR. The up-shifted and down-shifted fundamental and second (2^{nd}) harmonic resonances were considered separately. Various parallel and perpendicular velocities to the magnetic field, $v_{||}$ and $v_{\perp}$, were considered from the Doppler-shifted ECR condition for the electrons to be resonant with the ECH waves. Orbit trajectories of the resonant electrons were obtained for various positions of the coordinates (R,Z), pitch angles and the refractive indexes in a direction parallel to the magnetic field $N_{||}$ in the multiple-wall

reflection model. The number of the stepped parameters was more than 5,200000. A number of orbit trajectories were plotted as contour plots of the resonant electrons' energy on the equilibrium magnetic configuration. The energy was expressed in terms of magnetic moment μ and toroidal angular momentum p_φ . The energy, magnetic moment, and toroidal angular momentum were conserved in the orbit trajectories. Depending on the ECR for various conditions, the resonant electrons were travelled both in the parallel and the antiparallel directions to the magnetic field. The resonant electrons with initial positive $v_{||}$ were travelled in the parallel direction to the magnetic field, while the resonant electrons with initial negative $v_{||}$ were travelled in the antiparallel direction to the magnetic field. A large number of passing resonant electrons with initial positive $v_{||}$ starting from the high field side were maintained their orbits outside the LCFS, while all the passing resonant electrons with initial negative $v_{||}$ starting from the high field side were maintained their orbits inside the LCFS. The trapped resonant electrons only being the 2^{nd} harmonic ECR were maintained banana orbits at the low field side of the torus where most of the portions of the banana orbits of positive $v_{||}$ were placed outside the LCFS.

The orbit current distributions were evaluated from the electrons' orbital distributions along with the drift toroidal velocities, v_φ throughout the orbit. The electrons with initial positive $v_{||}$ were contributed positive current while the electrons with initial negative $v_{||}$ were contributed negative current. The trapped electrons with initial positive and negative $v_{||}$ were contributed both the positive and negative currents. The direction of the positive current was opposite to the toroidal magnetic field i.e. co-current direction of QUEST plasma current while the direction of the negative current was parallel to the toroidal magnetic field i.e. counter-current direction of QUEST plasma current. A significant amount of the positive current by the passing resonant electrons with initial positive $v_{||}$ appeared outside the LCFS, while the entire negative current by the passing resonant electrons with initial negative $v_{||}$ appeared inside the LCFS. The trapped electrons contributed both the positive and negative currents. The positive current portion was distributed outside the LCFS while the negative current portion was evaluated inside the LCFS.

In the summary, several codes required to evaluate the orbits have been developed with the EFIT code. Various criteria of non-relativistic and relativistic ECR conditions were properly taken into consideration for the orbit analysis. The current contribution appeared outside the LCFS could be qualitatively explained by the developed codes. Additionally, the developed code could be applicable to analyze the α -particle orbits of the burning plasmas.

Table of Contents

Chapter 1

Introduction

1.1 Energy and Nuclear Fusion

World energy demand to sustainability receives much interest in research and development communities since last few decades. Due to the increasing of human population, urbanization and modernization in all over the world, the growth in global energy demand is projected to rise sharply over the coming years [1, 2]. Since world energy demand cannot be satisfied much longer with fossil fuels [3] and fossil fuels have significant environmental impacts; large-scale and sustainable energy generation satisfying environmental requirement has to be developed. Nuclear energy, in particular fusion energy has the potential to become most promising energy source. It could utilize seawater as fuel, produce no CO_2 or any other harmful chemicals into the environment and radioactive waste would be very low. In fact, fuel reserves, environmental impact, and safety are definitely remarkable of fusion energy.

Nuclear fusion is the most fundamental form of energy in the universe. It is exactly on how the sun and all the stars produce their energy since their birth to the billions of years. It is produced by a nuclear reaction. When two light nuclei approach sufficiently close to each other against their electric repulsive force, they fuse and produce a new nucleus. The total mass of the two fused nuclei is slightly larger than the total mass of the new nucleus and by product. The different of the mass, Δm, between the two nuclei and reaction product nucleus is converted into kinetic energy E, according to $E = \Delta m c^2$, where c denotes the velocity of light. Several fusion reactions are possible such as Hydrogen (H) - Hydrogen (H), Deuterium (D) - Deuterium (D), Deuterium (D) - Tritium (T) and so on. However, the most important parameter of nuclear fusion reactions is the cross-section, which measures the probability per-pair of reactant for the occurrence of the reaction. Among all of the possible fusion reactions, Deuterium (D) - Tritium (T) fusion reaction is the most suitable candidate, because of large cross-sectional value and less energy requirement to overcome the repulsive force compare to others [4]. Deuterium (D)-Tritium (T) fusion reaction can be expressed as,

$$D + T \rightarrow He^4\left(3.5MeV\right) + n\left(14.1MeV\right) \tag{1.1}$$

If a nucleus of Deuterium (D) and a nucleus of Tritium (T) fuse together, a Helium (He^4) also known as α-particle is produced and a neutron is released. The rearrangement of these two nucleus results in a reduction in the total mass and consequently releases energy in the form of kinetic energy as the reaction products. The neutron receives the kinetic energy of 14.1 MeV and the α-particle receives the kinetic energy of 3.5 MeV. The total energy released per reaction is 17.6 MeV [5]. Figure 1.1 shows a schematic of a fusion reaction of the deuterium and tritium nuclei with their fusion product and released energies.

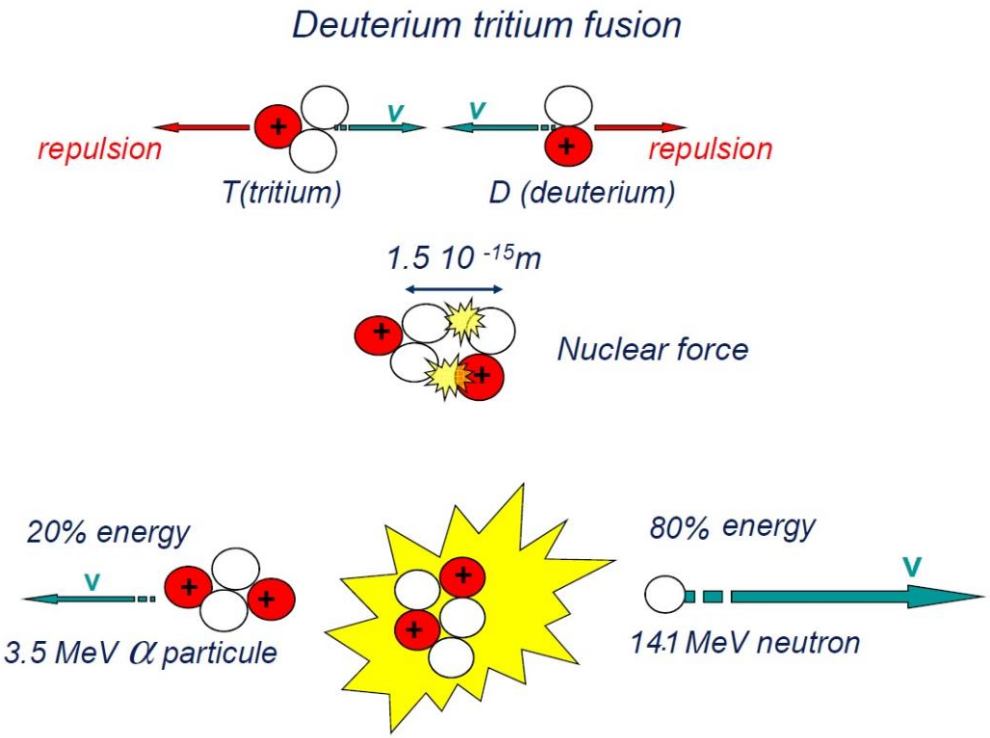

Figure 1.1: Fusion reaction of two nuclei. The nucleus of deuterium and the nucleus of tritium approach sufficiently close to each other against their electric repulsive force; they fuse and produce a new nucleus and a neutron along with 17.1 MeV kinetic energy. *[Figure courtesy: S. Benkadda]*

The resources necessary for fusion reaction as well as fusion reactor are well studied since last few decades. It is found that the required fuel for deuterium-tritium reactor is sufficiently resourceful. An abundant amount of Deuterium is reserved in the sea water which occurs naturally. The ration of deuterium and hydrogen in the sea water is 1: 6700. Also deuterium can be easily extracted at a very low cost. It will take about two billion years to consume all the deuterium, if all the deuterium stored in the sea is used in fusion reactors according to the present rate of total world energy consumption [6]. Since tritium, another fuel of deuterium-tritium reactor is not found naturally on earth, it can be obtained from the lithium isotope Li^6, where the lithium isotope is used as one of the components in the fusion blanket [7]. The extraction of tritium from lithium can be expressed as,

$$Li^6 + n \rightarrow He^4\left(2.05MeV\right) + T\left(2.75MeV\right) \tag{1.2}$$

Although lithium does not occur naturally in elemental form due to its high reactivity but it is widely distributed on the earth. By assuming the total world energy consumption at the present rate, it takes about 20000 years to consume all the abatable Li^6 on earth [6]. Figure 1.2 shows a schematic of how the tritium fuel can be produced inside the reactor by using Li^6 blanket.

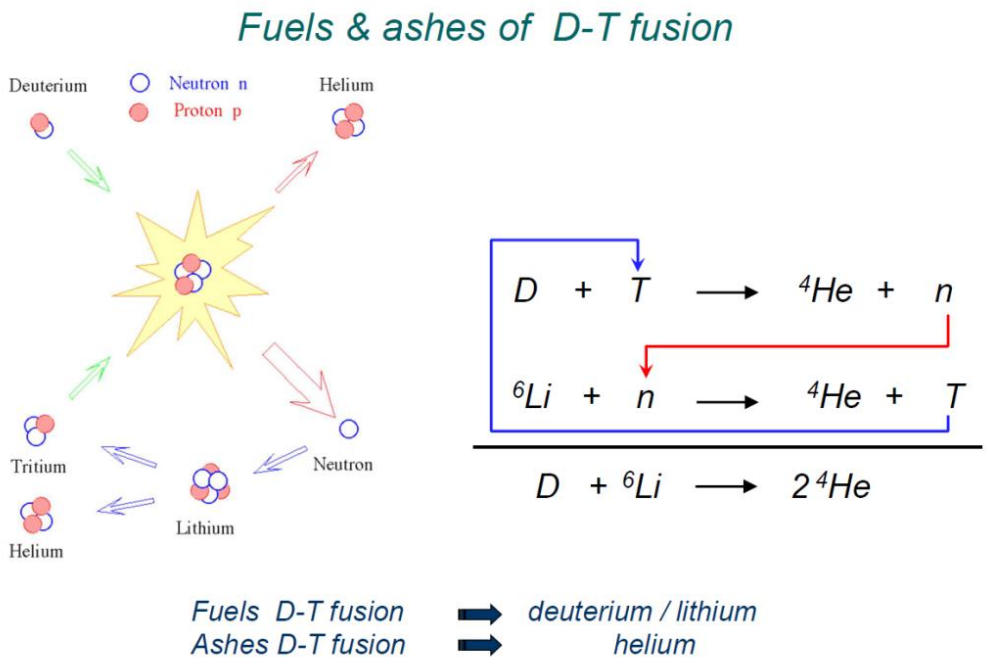

Figure 1.2: Fuel and ashes of the deuterium-tritium fusion. Tritium fuel can be produced inside the reactor by using Li^6 blanket. *[Figure courtesy: S. Benkadda]*

However, both the nuclei of deuterium and tritium are positively charged and they repel each other due to Coulomb's force. For that reason fusion reaction does not occur naturally. In order to induce fusion reaction among these two nuclei, it is necessary to overcome this repulsive force. In addition, the reactant nuclei should stay in the reacting region for a sufficient time for positive energy balance as well as the density of the reacting population must be large enough for the sufficient collision. All of the above mentioned criterions can be achieved by heating the deuterium-tritium mixture of gas at a temperature of about 100 million degrees centigrade. At such a high temperature, the kinetic energy of the reactant nuclei becomes high enough to produce the required reaction. At this high temperature the fuel also becomes fully ionized and becomes a mixture of equal number of negative electrons and positive nuclei. The resulting neutral gas is called plasma. The fusion carried out in this way is called thermonuclear fusion. Since, the burning process should be self-sustainable without further heating, the thermonuclear fusion must achieve a single criterion known as ignition and expressed approximately by $\hat{n}\tau_E\hat{T} > 5\times10^{21} m^{-3} sKeV$, where, $\hat{n}$ and $\hat{T}$ are the pick ion density and the temperature in the plasma, respectively and τ_E is the plasma confinement time [5].

The temperature of the thermonuclear fusion or the plasma is so high that there is no possibility of containing such hot plasma in any conventional vessel. One of the most promising ways to hold the plasma is using magnetic field. The magnetic field guides the charged particles and prevents them from hitting the surrounding solid walls. This is called magnetic confinement. The device that offers such type of confinement is known as Tokamak, a chamber of powerful magnetic field in the shape of a torus. Since the toroidal magnetic field of the tokamak is continuous along the center path, so charged particles of the plasma follow the magnetic field lines and travel a very long distance before reaching at the wall of the vessel. Thus, the tokamak is being developed to contain the hot plasma and it is the leading candidate for a practical fusion reactor. Tokamak attracts much attention to the fusion research communities to carry out various types of experiments and researches to understand the physics, technological and engineering challenges to achieve fusion energy [8]. A significant progress of fusion research has been achieved during the last 50 years and the research communities have reached at the stage to demonstrate the scientific and technological feasibility of fusion energy through International Thermonuclear Experimental Reactor (ITER) being constructed in France [9]. ITER is scheduled to produce first plasma in 2025 and start deuterium-tritium operation in 2035 [10].

1.2 Tokamak and Confinement of Plasma

The tokamak is a toroidal plasma confinement device with strong toroidal magnetic field (B_t) along its toroidal direction (φ) with reference of cylindrical coordinate system. Since the tokamak plasma is not exactly cylinder but torus, the strength of the toroidal magnetic field is inversely proportional to the major axis (R) from the torus axis and encircles the torus axis. In tokamak, the charged particles of the plasma gyrate and the guiding center of the particles move along the toroidal magnetic field. But due to the inhomogeneity and curvature of the toroidal magnetic field the guiding center of the charged particles drift. This drift of the guiding center depends on the charged of the particles. The ions and electrons drift in opposite direction. Thus, charge separation occurred inside the tokamak and these charge separation generates vertical electric field. However, due to the presence of the electric field, both the electrons and the ions are again drift towards the outer region of the confined plasma because of the $E \times B$ drift. For these reasons the plasma can't be confined in the tokamak by only the toroidal magnetic field. To overcome this problem, poloidal magnetic field (B_θ or B_p) should be introduced. The poloidal magnetic field prevents the separation of the charged particles to occur. It makes magnetic field line curved around the magnetic axis, and the magnetic field line becomes spiral. As a result, the magnetic surface is created. Though the charged particles can move freely along the magnetic field lines, spiral magnetic field lines enable charge separation to be short-circuited.

On the other hand, in order to have an equilibrium in which the plasma pressure (p) is balanced by the magnetic pressure $\left(B^2 / 2\mu_0\right)$, it is also necessary to have a poloidal magnetic field in the tokamak. The efficiency of the plasma confinement depends on the plasma beta $\left(\beta = 2\mu_0 p / B^2\right)$, defined as the ratio of the plasma pressure to the magnetic pressure. Since, both for the equilibrium and confinement of the plasma, two independent magnetic fields namely B_t and B_p are required in the tokamak. The plasma beta β can be also expressed as the toroidal beta $\left(\beta_t = 2\mu_0 \langle p \rangle / B_{t0}^2\right)$ and the poloidal beta $\left(\beta_p = 2\mu_0 \langle p \rangle / B_p^2\right)$ for respective fields. However, the main objective of the tokamak research is to generate electricity by using fusion energy. The tokamak should be economically cost effective compare with the fusion power output. The maximum fusion power output is proportion to $\beta_t^2 B_{t0}^4$. In addition, good confinement and steady-state operation of the tokamak is required. Therefore, the highest achievable β_t can be the solution of the effective tokamak for fusion power. The most accepted upper limit of β_t is the Troyon limit $\left(\beta_{tc} = I_p / aB_{t0}\right)$, which suggest that β_t can be increased by increasing the toroidal plasma current $\left(I_p\right)$ [11]. But it is extremely expensive to construct a machine with higher B_t.

On the other hand, MHD stability calculations show that the maximum I_p is restricted by the edge safety factor (q_a). Again, q_a can be increased by reducing the aspect ratio (A= major radius (R)/minor radius (a)) of the plasma. Such a tokamak with small aspect ratio $(A<2)$ is known as Spherical Tokamak (ST).

1.3 Spherical Tokamak

Though the world magnetic confinement fusion program is entering into the ITER and led to the ITER EDA (Engineering Design Activity), which began in 1992 [12]. But by reducing aspect ratio, plasma exhibits a natural elongation along the vertical direction and this elongation enhances β_{tc} as well as I_p. So, spherical tokamak (ST) becomes potentially more efficient alternative magnetic confinement fusion concept rather than the standard tokamak. Spherical tokamak is a kind of fusion power device with a very low aspect ratio, forming a more compact and cored apple shape plasmas. The spherical torus plasmas with an edge safety factor $q_a > 2$ can be characterized by high toroidal beta $(\beta_t > 0.2)$ and low poloidal beta $(\beta_p < 0.3)$. In addition, the spherical torus should be naturally large elongated as approximately $\kappa \cong 2$ with large plasma current as $I_p/(aB_t)$ up to about 7 $MA.mT^{-1}$, strong paramagnetism $(B_t / B_{t0} > 1.5)$, and strong magnetic helical pitch [13]. Figure 1.3 shows the comparison between the conventional and spherical tokamak (ST) with respect to their shape and size. The magnetic topology of ST remains the same as that of conventional tokamak. The toroidal field is generated mainly by the toroidal field coils and the poloidal field is generated mainly by the I_p. The poloidal filed in the outer region of the ST can be comparable with the toroidal field. But in standard tokamak the toroidal field is much stronger than the poloidal field. This significant change in the ratio of the field components allows larger I_p for a given toroidal field. In case of fusion energy development, the ST has potential advantages due to its compact geometries, which reduce the unit size and the overall development cost significantly [14]. In addition, due to their compactness, STs are able to achieve higher magnetic pressures at a given magnetic field. At present, comprehensive and significant progress in plasma tests, theory, new experiments, and future vision of ST have been performed on more than twenty ST devices all over the word [15]. The National Spherical Torus Experiment (NSTX) and the Mega Amp Spherical Tokamak (MAST) are the largest two spherical tokamak devices of with aspect ratio of about 1.3, toroidal field of about 0.5 T, and mega-ampere level plasma current. Broad study of the potential properties of the ST plasmas, fusion physics principles and engineering are performed on these

two devices [16-18]. Now to obtain more plasma current of about 2 MA and to establish efficient power exhauster, the NSTX has recently upgraded as NSTX-U and the MAST is still continuing its upgrading.

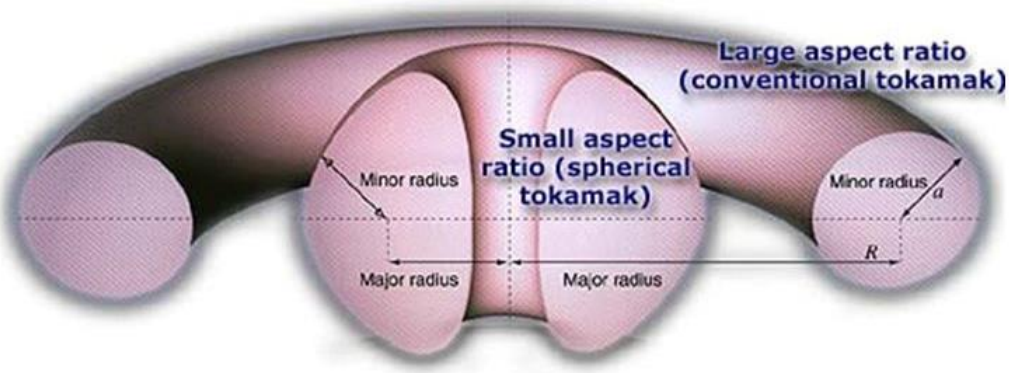

Figure 1.3: Spherical tokamaks in comparison to the conventional doughnut-shaped tokamaks. [*Figure Source: Culham Centre of Fusion Energy*]

However, to ionize the fusion fuels and to reach at the fusion condition, tokamak plasmas must be heated to extremely high temperature no matter it is based on large aspect ratio conventional tokamak or ST. Additionally, tokamaks require a source of high power current drive system to drive the I_p for the sustainment of the plasma for a long period of time [19]. These heating and current drive sources must be cost effective, efficient, operate constantly, and predictably generate the required plasma conditions. The usual Ohmic heating and current drive mechanism is characteristically pulsed and does not allow continuous plasma operation. Therefore, it becomes ineffective for steady-state operation of the tokamak. Hence, non-inductive current drive is necessary for achieving steady-state operation of the tokamak. Several non-inductive heating and current drive methods such as neutral beam injection (NBI), radiofrequency (RF) have been used to heat and drive the plasma current. Among them RF heating and current drive is recognized as essential tools for steady-state tokamak operation. Without these technologies, the tokamak concept as the basis for a steady-state, electricity producing power plant cannot be achieved [20]. Though the core physics, theory, modeling, engineering and infrastructure of the RFs heating and current drives are well established but still they focusing some challenging issues for demonstration in physics and engineering solutions for a reactor environment [21].

1.4 RF Heating and Current Drive

The theory and technological development of RF heating and current drive for tokamak plasmas during the last 40 years reach in a great success in the field of plasma science [22]. In RF heating and current drive methods, radiofrequency (RF) waves penetrate the plasma from an external source by means of electromagnetic waves and deposit momentum and energy to the selected resonant ions or electrons of the selected resonant regions [23]. When the electromagnetic waves are injected asymmetrically with respect to the toroidal direction in tokamaks, they can raise the temperature to the level required for ignition and drive a steady-state non-inductive toroidal electric current. This current is known as plasma current (I_p). In the tokamak plasmas, the ions and electrons gyrate around the magnetic field lines with specific frequencies and directions which depend on the strength of the magnetic field as well as their charge and mass. The injected electromagnetic waves of the right frequency with the plasma particles can resonate or damp their waves' power into the plasma. In addition, as the gyro-frequencies of the ions and electrons are different, one can target certain particles either ions or electrons by injecting waves of the respective frequency. However, three schemes of RF heating and current drive have emerged as the most successful, namely, electron cyclotron heating (ECH), ion cyclotron heating (ICH) and lower hybrid heating (LHH) [24].

The basic mechanism of RF heating and current drive is; a source sends electromagnetic waves along a transmission line to a launching structure at the plasma edge, the launching structure launch the electromagnetic wave in the plasma in such a way so that the wave-particle resonance occurs and the plasma absorbs energy from the RF waves. The type of source depends upon the operating frequencies. For a magnetic field of $B_0 = 5\,\mathrm{T}$, requires electron cyclotron frequency $f_{ce} = \omega_{ce}/2\pi = 140$ GHz, ion cyclotron frequency $f_{ci} = \omega_{ci}/2\pi = 38$ MHz and lower hybrid frequency $f_{LH} = 3\,\mathrm{GHz}$. These several types of frequencies can be generated by high power vacuum tubes ($f < 100\,\mathrm{MHz}$), klystrons ($f \approx 1-10\,\mathrm{GHz}$) and gyrotrons ($f \approx 10-300\,\mathrm{GHz}$). The transmission line for transmitting electromagnetic energy can be the waveguides. But proper choice of the waveguides depends on the wavelength of the RF power with the characteristic dimensions of the waveguides. Lastly, for launching the waves at the edge of the plasma waveguide array, antenna and mirroring system are used depending on the chosen frequency. On the other hand, a wave-particle resonance is the basic mechanism for absorbing energy from the RF waves to produce heat and to drive current. The general condition for a wave-particle resonance is $\omega = k_{\|} v_{\|} + n\omega_c$, where, n is the harmonic number. The wave-particle resonance

occurs when the parallel Doppler sifted frequency matches with the cyclotron frequency of the ions or electrons at a particular harmonic.

On LATE device, spherical torus plasma was obtained by electron cyclotron heating where the aspect ratio and elongation were approximately 1.4 and 1.3, respectively. After injecting a 2.45 GHz radio frequency of 10 kW for 4 seconds, the plasma current was initiated and ramped up to 4 kA [25]. On CDX-U device, toroidal plasma was obtained by pressure driven current in electron cyclotron heating. After applying microwave pulse up to 8 kW, a significant net toroidal current of about 1.05 kA was observed. This current level was significantly good enough to produce closed flux surfaces in small aspect ratio tokamak geometry [26]. On Tokamak Fusion Test Reactor (TFTR), ion cyclotron heating was conducted including mode conversion heating and current drive method. A central electron temperature of 10 keV was attained and up to 130 kA of plasma current was non-inductively driven in mode conversion heating [27]. On TST-2 spherical tokamak, lower-hybrid waves (200 MHz frequency) were used for non-inductive plasma current start up and sustainment. The maximum plasma current of about 16 kA was achieved by using 13-element capacity-coupled combine antenna system [28].

1.5 QUEST Spherical Tokamak

QUEST Device

The researches described in the thesis were performed for the QUEST (Q-shu University Experiment with Steady-State Spherical Tokamak). QUEST is a relatively compact medium-sized spherical tokamak device with improved high beta (high β) stability compared with the conventional tokamak. The main objective of the QUEST is to obtain steady-state operation as to study plasma wall interaction and non-inductive current drive phenomena [29]. The device parameters are; major radius $R = 0.68\,\mathrm{m}$, minor radius $a = 0.40\,\mathrm{m}$, aspect ratio $A = 1.70$, the toroidal magnetic field strength $B_t = 0.25\,\mathrm{T}$ (steady-state) and $B_t = 0.5\,\mathrm{T}$ (pulse) at $R = 0.64\,\mathrm{m}$. 16 turns toroidal field (TF) coil are set at outside of the vacuum vessel to produce the toroidal magnetic field. The vacuum chamber radius and height are 1.4 m and 2.8 m respectively. The center stack (CS) of outer diameter 0.4 m holds the Ohmic and toroidal field coils. Two flat divertor plates are set at vertical position of $Z = \pm 1$ m from the mid-plane, which are used for single/double null configurations for plasmas. In the present experiment, these flat plates are

being using as protector to terminate the open field lines outside the confined plasma. The inboard plasma boundary is controlled by a set of water cooled tungsten limiters on the CS at $R_{cs} = 0.22\,\text{m}$ which help to remove excess heat load. The working gas is basically Hydrogen (H), supplied from electrically controlled piezo valves located on the CS or the outboard side. Four pairs of poloidal field (PF) coils are used to generate different curvature of the field lines characterized by the magnetic mirror ratio $M = B_{t\_end} / B_{t\_start}$ along a field line, where, B_{t_start} and B_{t_end} are B_t at starting and ending points of on a particular B_z field line [30]. Figure 1.4 shows a schematic of the inside of the vacuum vessel and the toroidal and the poloidal field coils of QUEST spherical tokamak (*left*). The right part of the figure shows the poloidal cross-sectional side view of QUEST spherical tokamak including poloidal field (PF) coils. In QUEST, during non-inductive discharge energetic electrons at the resonance layer create initial plasma current (I_p) before formation of the closed flux surface due to high magnetic ratio. This initial seed current is enhanced with suitable ramping up of the B_z strength which enhanced the trapped electron energy [31]. Finally, the closed flux surfaces are formed at $I_p \geq 5\,\text{kA}$.

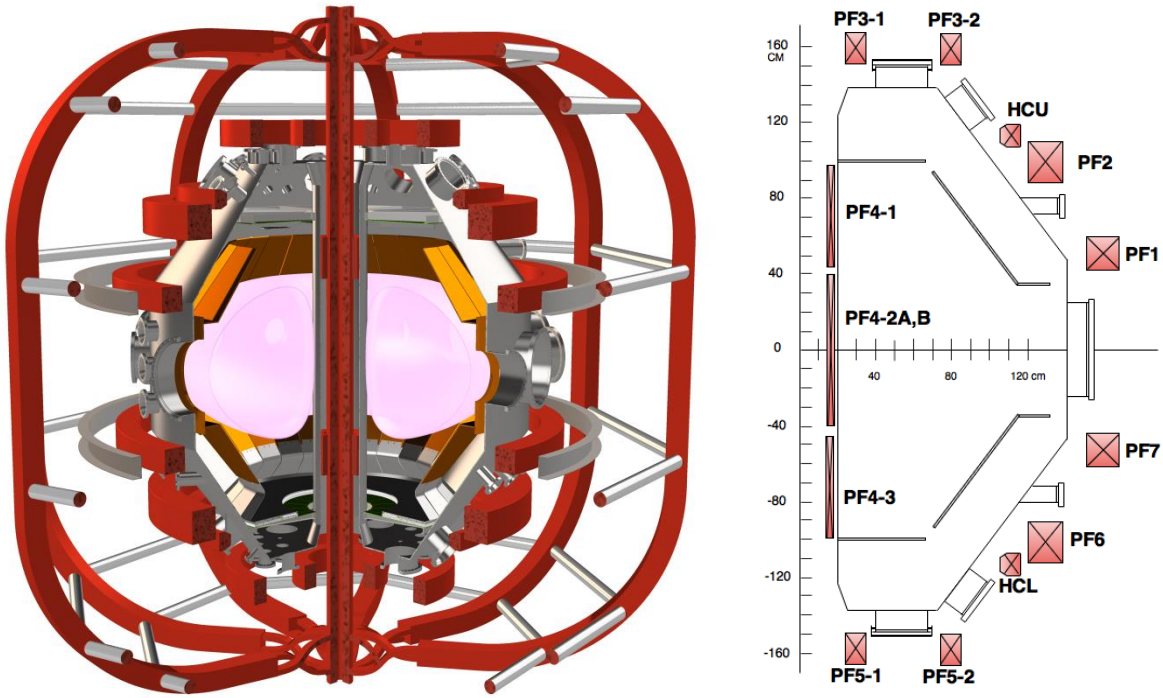

Figure 1.4: A schematic of the inside of the vacuum vessel and the toroidal and the poloidal field coils of QUEST spherical tokamak (*left*). A poloidal cross-sectional side view of QUEST including poloidal field (PF) coils (*right*). [*Left figure courtesy: Arseniy Kuzmin*]

In QUEST, plasma is initiated and sustained by electron cyclotron heating and current drive (ECH/CD) or ECH/CD assisted Ohmic heating (OH) discharge schemes. The ECH/CD system consists of two toroidally opposite 8.2 GHz Klystron systems ($2\times8\times25\,\mathrm{kW}$) corresponding to the off-axis and on-axis heating scenarios. Sixteen (16) waveguide transmission lines are prepared to take the phased-array conditions for the orthogonal electric fields. A phase array antenna of 16 waveguides elements is developed to obtain a focusing and steering beam for the ECH/CD. Additionally, 28 GHz gyrotron system (1 MW) is also reinstalled as a second harmonic off-axis start up and current drive system [32]. Recently, 70 kA of fully non-inductive plasma current is obtained by the 28 GHz ECH/CD discharge scheme for the 1.25 second pulse duration [33].

1.6 Motivation and Objectives

From the above discussion, it is now known that the fusion fuel heating and magnetic confinement is the basis of thermonuclear fusion. The Plasma Magneto-Hydro Dynamics (MHD) equilibrium and stability in magnetic field allowing fusion reactions to continuous as well as steady-state mode of operation. For stable plasma, the plasma particles need to be confined by the magnetic field in the tokamak and the plasma pressure should be balanced by the magnetic pressure. But according to the physics of the charged particles motion in the magnetic field, the toroidal magnetic field of the tokamak can't confine the plasma particles. To overcome this problem, additional magnetic field known as poloidal magnetic field (B_p) should be introduced which makes magnetic field line curved around the magnetic axis, and the magnetic field line becomes spiral. This poloidal magnetic field is usually produced by the plasma current $\left(I_p\right)$, a toroidal electric current inside the plasma. Additionally, continuous plasma current is essential for steady-state operation of tokamak. There are several methods to drive continuous plasma current. Radio frequency (RF) waves have been widely used for the non-inductive plasma current drive. Among all the RFs, the electron cyclotron heating and current drive (ECH/CD) is one of the intense methods of non-inductive plasma current drive. The plasma sustainment with RF or ECH waves is a key issue for the steady state operation in the tokamak configuration. The plasma was sustained for more than 2 hours by the ECH/CD non-inductive method in the Q-shu University experiment with steady-state spherical tokamak (QUEST). The ECH waves accelerated the electrons with the Doppler-shifted electron cyclotron resonance (ECR) interactions and effectively ramped and sustained the plasma current non-inductively for long discharge duration.

In the QUEST, 28 GHz and 8.2 GHz ECH waves have been used to attain the plasma current start-up and sustainment. The plasma current was generated with the abundant high-energetic electrons in the ECH/CD plasmas. The plasma current generation is strongly related to the ECR conditions and confinements of the electrons in the magnetic field. The plasma current fitting analyses for the ECH/CD plasmas showed that the plasma current existed in the open magnetic fields outside the last closed flux surface (LCFS). In the amount of the total current outside the LCFS, the orbit-driven current is dominant [34]. In this thesis, the guiding center orbits of the ECR electrons were calculated and analyzed under equilibrium magnetic configuration to consider the current distribution outside the LCFS.

The objectives of this research are therefore;

(1) Calculate equilibrium magnetic configuration from the plasma equilibrium solution of a discharge using EFIT code.
(2) Calculate and analyze the guiding center orbits of the ECR electrons under the equilibrium magnetic configuration.
(3) Evaluate orbit current distribution from the calculated the guiding center orbits of the resonant and confined electrons.

A framework with several sets of codes accordingly various theoretical model required to achieve above mentioned objectives are developed.

Various criteria of the plasma equilibrium solution, non-relativistic and relativistic ECR conditions are properly taken into consideration. Since a few limited Klystrons are only operated at the time, and any focusing and steering beam could not be obtained due to insufficient phased-array condition for the 8.2 GHz ECH/CD. The incident waves are very expanding from the launcher due to improper phased-array condition. In this research, the refractive indexes in a direction parallel to the magnetic field $N_{||}$ from -1 to $+1$ with step 0.1 are taken into account, when the multiple wall reflection effect on the wave absorption should be dominant due to improper incident electric polarization [32].

1.7 Thesis Organization

The thesis is organized as follows:

Chapter 2 discusses the development of the guiding center theory to understand the details behaviors of the guiding center orbits of charged particles in tokamak. At the beginning of this chapter several general properties of a charged particle's motion and behaviors of the guiding center are discussed in tokamak magnetic configuration. Then these general properties are discussed in combined to explain how magnetic fields confine charged particles in tokamak. The last part of this chapter covers the description about the physical appearance of the drift guiding center orbits on the poloidal flux surfaces.

In chapter 3, a brief description of the plasma equilibrium solution for a discharge by the equilibrium fitting (EFIT) code is given. In the first half of this chapter, the mathematical model and the algorithms of the EFIT code are discussed. Then various plasma experimental parameters of QUEST plasma discharge are discussed. These experimental data are fitted to the EFIT code to calculate the plasma equilibrium solution. Finally, a brief description is given at the last part of this chapter about the obtained equilibrium solution from EFIT code. The orbits are calculated and analyzed under the obtained equilibrium magnetic configuration.

Chapter 4 deals with the calculations and characteristics analysis of the guiding center orbits of ECR electrons. In first part, non-relativistic Doppler shifted waves-electrons resonance condition, waves' energy absorption, pitch angles distribution and the equations for the guiding center orbits of the non-relativistic electrons are discussed. Then the characteristics and the effects of the obtained orbits are discussed both for the fundamental and the 2^{nd} harmonic resonant electrons separately. In the last part of this chapter, relativistic Doppler shifted waves-electrons resonance condition, waves' energy absorption, pitch angles distribution and the equations for the guiding center orbits of the relativistic electrons are discussed. Then the characteristics and the effects of the obtained orbits are also discussed both for the fundamental and the 2^{nd} harmonic resonant electrons separately.

Chapter 5 describes the electron orbital distribution and the orbit current distribution calculations processes as well as the obtained results. The orbit current distributions were obtained as the contour plots of the positive and negative currents distribution on the poloidal cross-section, the positive and negative currents distribution profiles of the equatorial plane current on R and the

surface-averaged current distribution profiles of the closed flux surfaces on the square root of the normalized poloidal flux index. In the first half, the features and significances of the obtained current distribution are discussed for the non-relativistic fundamental and 2^{nd} harmonic resonant electrons. In the last half, the features and significances of the obtained current distribution are discussed for the relativistic fundamental and 2^{nd} harmonic resonant electrons.

In Chapter 6, the summary of the thesis and future work are listed.

Chapter 2

Guiding Center Theory for Tokamaks

2.1 Introduction

The development of guiding center theory provides the basic intuition necessary to understand the charged particle confinement by the magnetic field in tokamak. This chapter discusses the development of the guiding center theory to understand the details behaviors of the guiding center orbits of the charged particle by considering several general properties of a charged particle's motion and behaviors in tokamak magnetic field. Finally, in this chapter the general properties of a charged particle are discussed in combined to explain how magnetic fields confine charged particles in tokamak as well as the physical appearance of the drift guiding center orbits on the poloidal flux surfaces.

2.2 Single Particle's Equations of Motion

The equation of motion for a particle of mass m and charge q, under the influence of the Lorentz force due to electric (E) and magnetic field (B) fields can be written as,

$$\begin{aligned} F &= m\frac{dv}{dt} = q\left(E + v \times B\right) \\ \frac{dr}{dt} &= v \end{aligned} \tag{2.1}$$

The behavior of a charged particle in a uniform, time independent magnetic field is the basic building block of the magnetic confinement and the basis of the guiding center theory. The particle orbit in such magnetic configuration shows good confinement perpendicular to the direction of the magnetic field and no confinement parallel to the magnetic field. This behavior can be clearly demonstrated by solving the equation of motion (2.1) assuming $E = 0$, $B = |B|e_z$ and $B = \text{const.}$

The equation of motion can be reduced in components form and can be expressed as,

$$\begin{aligned} dv_x / dt &= \omega_c v_y & v_x(0) &= v_{x0} \equiv v_\perp \cos\varphi \\ dv_y / dt &= -\omega_c v_x & v_y(0) &= v_{y0} \equiv v_\perp \sin\varphi \\ dv_z / dt &= 0 & v_z(0) &= v_{z0} \equiv v_\parallel \\ dx / dt &= v_x & x(0) &= x_0 \\ dy / dt &= v_y & y(0) &= y_0 \\ dz / dt &= v_z & z(0) &= z_0 \end{aligned} \tag{2.2}$$

Here, $\omega_c = q|B|/m$ is the gyro frequency also known as cyclotron frequency, $v_\perp$ and $v_\parallel$ are constants and denote the initial perpendicular and parallel velocities of the charged particle, respectively, x_0, y_0 and z_0 denote the initial positions of the charged particle.

Consider the charged particle motion in parallel to the magnetic field. The associated components of the equation of motion are,

$$\begin{aligned} dv_z / dt &= 0 & v_z(0) &= v_{z0} \equiv v_\parallel \\ dz / dt &= v_z & z(0) &= z_0 \end{aligned} \tag{2.3}$$

The solution of the component of the equation of motion in (2.3) is,

$$\begin{aligned} v_z(t) &= v_\parallel \\ z(t) &= z_0 + v_\parallel t \end{aligned} \tag{2.4}$$

The above equation (2.4) shows that the parallel motion of the charged particle is constant and uniform along the magnetic field. There are no parallel forces for the confinement of the charged particle parallel to the magnetic field and the particle simply continues without any interrupt. Thus, the motion of the charged particle is consequently unconfined along a given magnetic line. The magnetic force always acts perpendicular to the particle velocity (v) which leads to a circular-type motion.

Consider the associated components of the equation of motion for the velocity,

$$\begin{aligned} dv_x / dt &= \omega_c v_y & v_x(0) &= v_{x0} \equiv v_\perp \cos\varphi \\ dv_y / dt &= -\omega_c v_x & v_y(0) &= v_{y0} \equiv v_\perp \sin\varphi \end{aligned} \tag{2.5}$$

By replacing v_x constituent, the equation (2.5) can be expressed as,

$$\begin{aligned} &d^2 v_y / dt^2 + \omega_c^2 v_y = 0 \\ &v_y(0) = v_\perp \sin\varphi \\ &dv_y(0)/dt = -\omega_c v_x(0) = -\omega_c v_\perp \cos\varphi \end{aligned} \tag{2.6}$$

Equation (2.6) describes a simple harmonic oscillator at the cyclotron frequency ω_c . The equation is also a linear ordinary differential equation with constant coefficients. The general solution of this equation is then,

$$\begin{aligned} v_y(t) &= -v_\perp \sin(\omega_c t - \varphi) \\ v_x(t) &= v_\perp \cos(\omega_c t - \varphi) \end{aligned} \tag{2.7}$$

The equation (2.7) demonstrates that the particles rotate with an angular frequency equal to the gyro frequency. Also, for a uniform magnetic field, not only the total kinetic energy is conserved, but also the separate parallel and perpendicular energies are individually conserved; $v_z^2(t) = v_\parallel^2 =$ const. and $v_x^2(t) + v_y^2(t) = v_\perp^2 =$ const. The particle trajectory $x(t), y(t)$ can be obtained by integrating the velocity component of equation (2.7) as,

$$\begin{aligned} x(t) &= x_g + r_L \sin(\omega_c t - \varphi) \\ y(t) &= y_g + r_L \cos(\omega_c t - \varphi) \end{aligned} \tag{2.8}$$

Here, $r_L = v_\perp / \omega_c = m v_\perp / q|B|$ is the gyro radius also known as Larmor radius. The quantities x_g, y_g are defined as the guiding center position of the particle. The terminology of the equation (2.8) presents the trajectory of the charged particle as,

$$(x - x_g)^2 + (y - y_g)^2 = r_L^2 \tag{2.9}$$

The orbit of the particle is circular with a radius equal to the gyro radius r_L . The center of the orbit (x_g, y_g) is known as guiding center. By following the velocity and position of the guiding center, it is easy to obtain a precise picture of the average particle location, the difference between each orbit even in a small deviation of order of gyro radius. In fact, guiding center motion provides a powerful intuition into the motion of charged particles in tokamak. However,

since the electrons and ions have opposite sign charges, they rotate in the opposite direction. The gyro frequency is propositional to the magnetic field strength. The electron gyro frequency is much larger than the ion gyro frequency by the ratio $\left(m_i / m_e\right)$. In addition, the gyro radius increases with the perpendicular velocity $v_\perp$ and decreases as the magnetic field strength increases. The ion gyro radius is larger than the electron gyro radius by the ratio $\left(m_i / m_e\right)^{1/2}$. The combination of the perpendicular and parallel motion of a charged particle represents a helical trajectory, where particle twisting and traveling along field line with a small perpendicular excursion equal to the gyro radius. This gyro motion of the charged particles in a static, homogeneous magnetic field represents the basic building block for magnetic confinement of the fusion plasma.

2.3 Drift of Guiding Center

Tokamak is chamber of toroidal magnetic field $\left(B_t\right)$ along its toroidal direction $\left(\phi\right)$ with the reference of cylindrical coordinate system. Since the toroidal magnetic field is not exactly a cylinder but torus, the strength of the toroidal magnetic field is inversely proportional to the major axis $\left(R\right)$ and encircles the torus axis. In tokamak, the charged particles of the plasma gyrate and the guiding center of the particles move along the toroidal magnetic field. Due to inhomogeneity and curvature of the magnetic field, the guiding center of the charged particle drifts. These drifts are classified in several ways such as gradient drift and curvature drift.

2.3.1 Grad-*B* drift $\left(B\times\nabla B\right)$

In general, introducing inhomogeneity is too complicated to obtain exact solutions for guiding center's drift. Therefore, orbit theory of approximation is used: for one Larmor orbit, B is nearly uniform. The magnetic field B varies for the typical length-scale L, where $L \ll r_L$ and the gyro-orbit is nearly circle. Here, L denotes the scale length of the inhomogeneity. Assume the lines of force are straight, but their density increase in *y*-direction so spatially-varying magnetic field $B=\left(0,0,B_z\left(y\right)\right)$, i.e. B has only z component and the strength of the magnetic field varies in the *y*-direction and $E=0$. The equation of motion can be reduced in components form according to the Newton's laws which can be expressed as,

$$
\begin{aligned}
F_x &= q\left(v_y B_z\right) \\
F_y &= -q\left(v_x B_z\right) \\
F_z &= 0
\end{aligned}
\tag{2.10}
$$

Since, L is the scale length of the inhomogeneity $\left(L >> r_L\right)$, the gradient of B_z can be written as $dB_z / dy \cong B_z / L << B_z / r_L$. Hence the magnetic field strength can be expanded in a Taylor expansion around the value at $y = 0$, for distance $y \le r_L$. So, expanding B_z in a Tailor expansion to the first order $\left(B_z\left(y\right) = B_0 + y dB_z / dy\right)$ and substituting the value into the equation (2.10),

$$
\begin{aligned}
F_x &= q v_y \left(B_0 + y \frac{dB_z}{dy} \right) \\
F_y &= -q v_x \left(B_0 + y \frac{dB_z}{dy} \right)
\end{aligned}
\tag{2.11}
$$

As $x - x_g = r_L \sin\left(\omega_c t - \varphi\right)$ and $y - y_g = \pm r_L \cos\left(\omega_c t - \varphi\right)$ describes a circular orbit of particle at guiding center $\left(x_g, y_g\right)$ of the helical trajectory, the velocity components can be written as,

$$
\begin{aligned}
x &= r_L \sin\left(\omega_c t\right) & \qquad v_x &= v_\perp \cos\left(\omega_c t\right) \\
y &= \mp r_L \cos\left(\omega_c t\right) & \qquad v_y &= -v_\perp \sin\left(\omega_c t\right)
\end{aligned}
\tag{2.12}
$$

Substituting equation (2.12) into the equation (2.11), the equation (2.13) can be obtained,

$$
\begin{aligned}
F_x &= -q v_\perp \sin\left(\omega_c t\right)\left(B_0 \mp r_L \cos\left(\omega_c t\right) \frac{dB_z}{dy} \right) \\
F_y &= -q v_\perp \cos\left(\omega_c t\right)\left(B_0 \mp r_L \cos\left(\omega_c t\right) \frac{dB_z}{dy} \right)
\end{aligned}
\tag{2.13}
$$

If consider only the guiding center motion, the time-averaged force in the *x*-direction is $\langle F_x \rangle = 0$ and the time-averaged force in the y-direction is obtained from equation (2.13) as,

$$
\langle F_y \rangle = \pm q v_\perp \frac{1}{2} r_L \frac{dB_z}{dy}
\tag{2.14}
$$

In general, the guiding center drift equation due to the gradient of the magnetic field can be written as,

$$
v_{\nabla B} = \pm \frac{1}{2} v_\perp r_L \frac{B \times \nabla B}{\left|B^2\right|}
\tag{2.15}
$$

The positive charged particles drift in $+x$ direction and negative charged particles drift in $-x$ direction. Consider, $r_L = mv_\perp / qB$, local gyro-radius is larger where B is small and local gyro-radius is smaller where B is large.

2.3.2 Curvature drift

There is also additional drift specifically associated with non-uniform B and $E = 0$. This is known as curvature drift of the guiding center, where the lines of forces to be curved with a constant radius of curvature R_c. When a charged particles move along a curved magnetic field lines, experience centrifugal force $F = mv^2 / r$ perpendicular to the magnetic field lines, here F is the centrifugal force, v is the constant speed, m is mass of the rotating body and r is the radius of the path.

Assume, radius of the curvature is R_c, where $R_c >> r_L$. The outward centrifugal force is,

$$F_{cf} = \frac{mv_\parallel^2}{R_c}\hat{r} = \frac{mv_\parallel^2}{R_c}\frac{R_c}{|R_c|} = mv_\parallel^2\frac{R_c}{|R_c^2|} \tag{2.16}$$

If the value of F_{cf} directly inserted into general form for the guiding center drift, the below equation for the curvature drift can be obtained,

$$v_R = \frac{mv_\parallel^2}{q|R_c^2|}\frac{R_c \times B}{|B^2|} \tag{2.17}$$

In practice, curved field lines will always be converging/ diverging. Thus, the curvature drift is always accompanied with grad-*B* drift. As ∇B is in opposite direction to R_c, the grad-*B* and the curvature drifts act in the same direction.

2.3.3 Combined Gradient and Curvature Drifts in a Vacuum Magnetic Field

In a steady-state fusion plasma with $E = 0$, the inhomogeneous and curved magnetic field produce two types of drifts of the guiding center; the ∇B drift and the curvature drift. For special situation where the plasma currents are small, the magnetic field becomes approximately a vacuum magnetic field and both the gradient and the curvature drifts act in the same direction. And hence there is no way of their resulting current to cancel.

For vacuum magnetic field $\nabla \times B = 0$. In the cylindrical coordinate $\nabla \times B$ has only the z component. Since, B has only θ component and ∇B has r component. The below vector identity can be written,

$$\begin{aligned} \left(\nabla \times B\right)_z &= \frac{1}{r}\frac{\partial}{\partial r}\left(rB_\theta\right) = 0 \\ \left(\nabla B\right)_{perp} &= -\frac{\left|B\right|\bar{R}_c}{\left|R_c^2\right|} \end{aligned} \tag{2.18}$$

Using this relation in the expression of the ∇B drift in the equation (2.15) leads a simple expression for the combined gradient and curvature drifts $\left(v_{\nabla B} + v_R\right)$ as,

$$v_{\nabla B} + v_R = \pm\frac{m}{q}\frac{R_c \times B}{\left|B^2\right|\left|R_c^2\right|}\left(v_\parallel^2 + \frac{1}{2}v_\perp^2\right) \tag{2.19}$$

2.4 Guiding Center Motion in Fields with Parallel Gradients

In a uniform magnetic field, a charged particle gyrates around a magnetic field line and the guiding center of the particle moves with constant velocity along the magnetic field. But the charged particle's moving parallel to a magnetic field is not subject (related) to any magnetic force. So, magnetic field has no effect on the parallel velocity of the particle. Only has an effect on perpendicular velocity of the particle. Since, the toroidal magnetic field of the tokamak is proportional to $1/R$, the field is smaller on the outer side of the torus. Particles in this region having a small velocity parallel to the magnetic field undergo a magnetic force as they move into the region of higher field due to the drift of the guiding center. In the absence of collisions the particles are trapped in the low field side region and undergo repeated reflection between turning points (go forward and backward).

Consider a magnetic field in *z*-direction and whose magnitude varies in the *z*-direction. Let, the magnetic field is axisymmetric with $B_\theta = 0$ and $\partial/\partial\theta = 0$. The line of force is converge and diverge i.e. increasing field strength, so there is a component B_r. As the divergence of B is 0, calculates B_r as a function of B_z from $\nabla.B = 0$, the equation (2.20) is obtained,

$$\frac{1}{r}\frac{\partial}{\partial r}\left(rB_r\right) + \frac{\partial B_z}{\partial z} = 0 \tag{2.20}$$

Assume $\partial B_z / \partial z$ is almost constant with r (compared to the gyro-scale) and is specified a position at r_0. Approximately, from the equation (2.20) the below equation can be written,

$$\begin{aligned} rB_r &= -\int_0^r r \frac{\partial B_z}{\partial z} \partial r = -\frac{1}{2} r^2 \frac{\partial B_z}{\partial z} \\ B_r &= -\frac{1}{2} r \frac{\partial B_z}{\partial z} \end{aligned} \tag{2.21}$$

Here, B_r can be expressed in terms of B_z. In cylindrical (r, θ, z) coordinate system, the components of the Lorentz force are,

$$\begin{aligned} F_r &= q v_\theta B_z \\ F_\theta &= q\left(v_z B_r - v_r B_z\right) \\ F_z &= -q v_\theta B_r \end{aligned} \tag{2.22}$$

The first two terms of the equation (2.22) gives rise to the usual Larmor gyration. Substituting the value of B_r in the third term of equation (2.22) and averaging the equation over one gyro-orbit by putting $v_\theta = v_\perp$ and $r = r_L$, the equation of the mirror force is obtained as define in the equation (2.23). Here $(\pm)$ arises because particles orbits of opposite charged rotated in the opposite direction in the magnetic field.

$$F_z = \pm \frac{1}{2} q \frac{v_\perp^2}{\omega_c} \frac{\partial B_z}{\partial z} \tag{2.23}$$

The equation (2.23) can be expressed in terms of magnetic moment $\mu = m v_\perp^2 / 2B$, which is the product of current and area enclosed by particle undergoing gyro-motion as,

$$F_\parallel = -\mu \nabla_\parallel B \tag{2.24}$$

Where, $F_\parallel$ is the mirror force, acting in the direction parallel to B and s is the line element directed along B and $|B|$. As the particle moves into the region of stronger or weaker magnetic field, its Larmor radius changes but magnetic moment μ remains constant. As magnetic field strength B increase, the perpendicular component of the particle velocity increases. Since we have $E = 0$, the total energy of the particle can't increase. Thus as $v_\perp$ increase, $v_\parallel$ must decrease, means the particle slows down in its motion along the field. If the field convergence is strong

enough at some point the particle may have $v_{\parallel} = 0$. But since the mirror force is still acting in the $-B$ direction, the particle will turned around. This is called magnetic mirror.

2.5 Guiding Center Orbit

As discuss above, it has been assumed that in a tokamak the inhomogeneity and curvature of the magnetic field lead to the drifts of the guiding center. In the absence of collisions these drifts create two types of the guiding center orbit; passing particle orbit and trapped particle orbit. Figure 2.1 shows the drifts directions of guiding centers of the ion and electron in tokamak (*left*) and the drift guiding center orbit of an electron in a circular and nonuniform magnetic field (*right*). Figure 2.2 shows the poloidal projection of the drift guiding center orbits of the passing and trapped electrons. In electron cyclotron heating, the resonant electrons also travel to antiparallel direction of the magnetic field. In the figure 2.2 the drift guiding center orbits of the electron is also shown that travels to the anti-parallel direction of the magnetic field *(middle*).

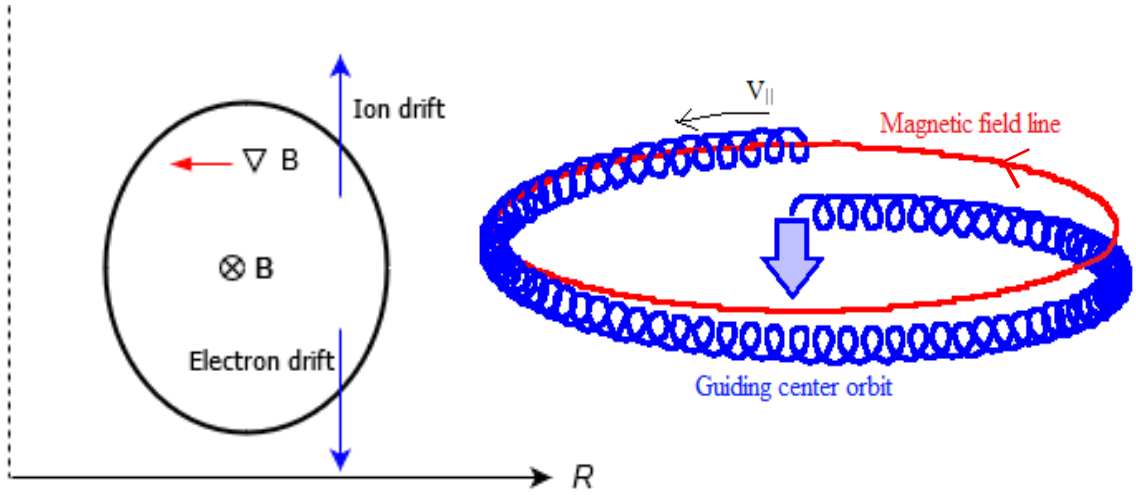

Figure 2.1: Drifts directions of the guiding centers of the charged particles, when particles gyrate and travel in nonuniform and curvature magnetic field. The directions of the drifts depend on the charge of the particle. The Ion drifts upward while the electron drifts downward in tokamak magnetic configuration (*left*). The drift guiding center orbit of an electron in a circular and nonuniform magnetic field (*right*).

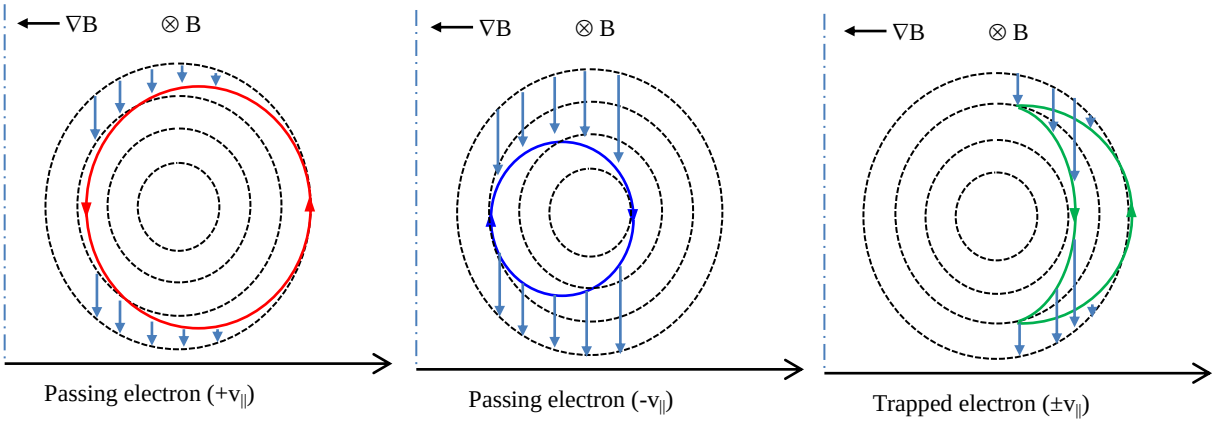

Figure 2.2: Poloidal projection of the drift guiding center orbits of the passing and trapped electrons. The dotted circles denote the flux surfaces and the solid circles denote the guiding center orbit on the poloidal cross-section. The guiding center orbit of a passing electron travels in the parallel direction to the magnetic field (*left*). The guiding center orbit of a passing electron travels in the antiparallel direction to the magnetic field (*middle*) and the guiding center orbit of a trapped electron that is trapped on the outer side of the torus by the magnetic mirror. The poloidal projection of the orbit creates banana-shaped (*right*).

The distance of the drift-orbit from magnetic surface can be calculated by the conservation of the canonical angular momentum which follows from the toroidal symmetry. The conservation of canonical angular momentum can be obtained by calculating the change of the angular momentum using the equation of motion in the toroidal direction. The equation of motion in the toroidal direction in (R,φ,Z) coordinate system can be expressed as,

$$m\frac{d}{dt}\left(Rv_{\varphi}\right)=qR\left(v\times B\right)_{\varphi} \tag{2.25}$$

In the cylindrical coordinate system (R,φ,Z), the poloidal magnetic field is related to ψ by $B_R=-(1/R)\partial\psi/\partial Z$ and $B_Z=(1/R)\partial\psi/\partial R$, where ψ is the poloidal flux per radian. The equation of motion in the toroidal direction can be written as,

$$m\frac{d}{dt}\left(Rv_{\varphi}\right)=-qv.\nabla\psi \tag{2.26}$$

Since, $d\psi / dt = v.\nabla\psi$ and ψ is the poloidal flux function.

The equation of (2.26) becomes,

$$\frac{d}{dt}\left(mRv_{\varphi} + q\psi\right) = 0$$
$$\frac{dp_{\varphi}}{dt} = 0 \tag{2.27}$$

Here the toroidal angular momentum p_{φ} is given by,

$$p_{\varphi} = mRv_{\varphi} + q\psi \tag{2.28}$$

The constancy of the toroidal angular momentum p_{φ} implies that orbit involves a change in ψ. This means that the displacement of the orbit occurs across the flux surface. Figure 2.3 shows a schematic about the changing of ψ by the orbit due to constancy of p_{φ}.

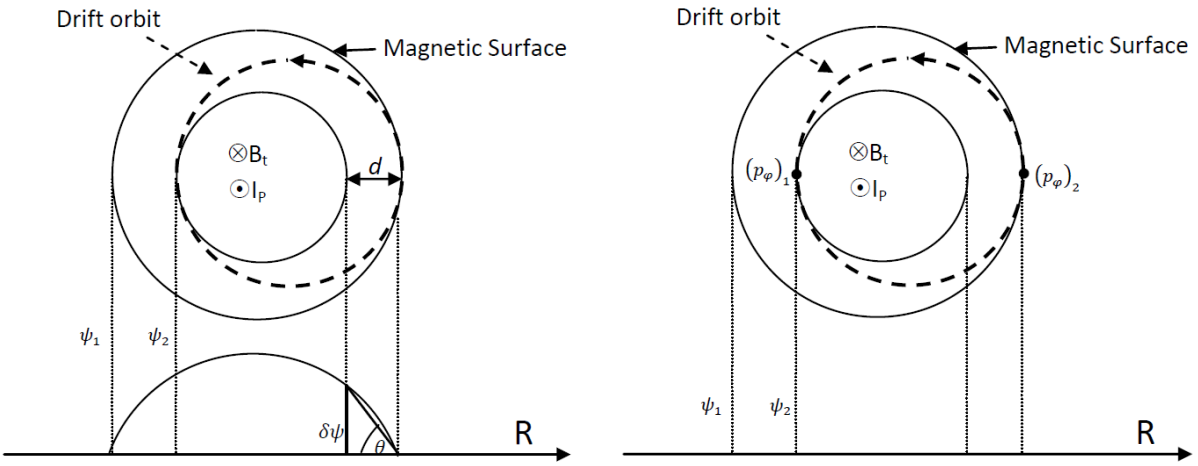

Figure 2.3: The constancy of the canonical momentum, p_{φ} implies that orbit involves a change in flux function, ψ. For a small displacement d from the flux surface changes in the flux function is $|\delta\psi| = |\nabla\psi| d$ (*left*). The constancy of p_{φ} implies that p_{φ} at position 1 is equal to p_{φ} at position 2 which means that the displacement of the orbit occurs across the flux surface (*right*).

For a small displacement d from the flux surface, the change in the flux function is $|\delta\psi| = |\nabla\psi| d$. And the constancy of p_φ implies that $\left(p_\varphi\right)_1 = \left(p_\varphi\right)_2$, which leads to write,

$$d = \left| \frac{m\delta\left(Rv_\varphi\right)}{q|\nabla\psi|} \right| \tag{2.29}$$

The drift surfaces of the passing particles are determined by the parallel motion to the magnetic field which also gives rise to a poloidal rotation and vertical drift due to gradient and curvature. The resulting equation of the drift surface and the displacement from the magnetic surface are,

$$\begin{aligned} &\left(R - R_c - \frac{v_d}{\omega_c} \right)^2 + Z^2 = a^2 = const. \\ &d = \frac{v_d}{\omega} \cong \frac{v_\parallel r}{R\omega_{c\theta}} + \frac{v_\perp^2 r}{2v_\parallel R\omega_{c\theta}} \end{aligned} \tag{2.30}$$

The drift surface on which the trapped particle orbit existed is obtained by including the r component of the vertical drift due to the gradient and the curvature of the toroidal magnetic field. For $v_\perp >> v_\parallel$, this drift becomes $v_d = mv_\perp^2 / 2qRB_\varphi$. This drift is almost constant.

$$\left(r - r_0\right)^2 = \left(\frac{\theta_b v_d}{\omega_b} \right)^2 \left(1 - \left(\frac{\theta}{\theta_b} \right)^2 \right) \tag{2.31}$$

The above equation (2.31) is the drift surface equation. This surface has the shape of banana and the orbits are called banana orbits.

Chapter 3

The Equilibrium Fitting Code (EFIT Code)

3.1 Introduction

The equilibrium magnetic configuration for the calculations and analyses of the electron cyclotron resonant electrons' guiding center orbits was obtained from the EFIT plasma equilibrium solution of a discharge. The plasma equilibrium solution for QUEST plasma discharge was calculated using EFIT (equilibrium fitting) code. The EFIT code computed the plasma equilibrium and shaping as well as equilibrium magnetic configuration in the (R,Z) plane by solving the Grad-Shafranov equation from the external magnetics for constraint of a discharge. A mathematical model and set of calculation codes were developed with the basic framework of EFIT code for the equilibrium solution of the QUEST plasma discharge. The obtained plasma equilibrium and shaping were properly taken into account for the orbits analyses and current evaluation, but the evaluated current was not included in the plasma equilibrium and shaping self-consistently. The features of the EFIT code are discussed in this chapter.

3.2 The EFIT code and its Structures

The EFIT code is a computer programming code basically based on the Grad-Shafranov plasma equilibrium equation that has been developed to reconstruct the plasma shape as well as the flux surfaces from the experimental data of the tokamak. This code is used not only to reconstruct the plasma shape but also to analyze various plasma parameters such as the plasma boundary, the internal inductance, the average poloidal beta, the q-profile and the internal magnetic measurements [35]. The magnetic measurement, poloidal field coils' currents and tokamak geometry are the fundamental input of the EFIT code. This code can run either in equilibrium mode or in fitting mode. In the equilibrium mode, it acts as an equilibrium solver where the equilibrium can be computed either with a fixed specific boundary or with a free boundary when the shaping coils current are given. In fitting mode, it can grip all the available experimental and

diagnostic data such as external magnetic data, probes and flux loops data, kinetic profile, topological geometry and so on [36]. The data can be directly fitted inside the code or can be retrieved from the input data file or data bank directory. In the real-time equilibrium fitting (RTEFIT) model, data can be obtained directly from the tokamak during its operation via A/D converters [37]. Up to now the EFIT code becomes a strong tool to analyze plasma performance and to control the plasma operation for its remarkable capabilities. The capabilities of the EFIT code are; it can be used to get various information about the plasma such as plasma shape, current profiles, stored energy and so on. It can also be used to unfold the experimental measurements into useful physics knowledge, to reconstruct magnetic geometry, to develop shape control algorithm, and to upgrade the operation and control of the tokamak [36].

The basic equation of the EFIT code is the Grad-Shafranov equation where the poloidal flux $\psi(R,Z)$ can be written as,

$$\Delta^* = \frac{1}{R}\left(R\frac{\partial}{\partial R}\frac{1}{R}\frac{\partial \psi}{\partial R} + \frac{\partial^2 \psi}{\partial Z^2} \right) = -\mu_0 J_T \tag{3.1}$$

$$F(\psi) = \mu_0 f(\psi) = RB_T \tag{3.2}$$

$$J_T = RP'(\psi) + \frac{FF'(\psi)}{\mu_0 R} \tag{3.3}$$

Here, operator Δ^* is equal to $\left(-(\nabla \times B)_T\right)$, J_T is the toroidal component of the plasma current density, ψ is the poloidal flux per radian, $P = P(\psi)$ is the pressure of the plasma expressed in terms of flux function, $F = RB_T$ is related to the poloidal current density, $f(\psi)$ is the current flux function [38].

The particular method to compute the Grad-Shafranov equation is the Green's function approach. The function $G(\bar{r},\bar{r}')$ is called Green's function for the operator Δ^*. The equilibrium Grad-Shafranov equation can be expressed by the equations (3.1) and (3.3) and recast into the integral form of the toroidal Green's function as $G(\bar{r},\bar{r}_{en})$ and the solution is then obtain by Picard iterations process as,

$$\psi^{(m+1)}(\bar{r}) = \sum_{n=1}^{n_e} G(\bar{r},\bar{r}_{en}) I_{en} + \int_{\Omega^{(m)}} dR'dZ'G(\bar{r},\bar{r}')J_T\left(R',\psi^{(m)}\right) \tag{3.4}$$

where ψ is the flux function, m denotes the iteration cycle, n_e is the number of the external shaping coils, I_{en} is the current strength of the n-th external coil located at $\bar{r}_{en}$, Ω is the plasma volume and J_T is the toroidal current density. The Picard iteration process is based on,

$$\chi^2 = \sum_{i=1}^{n_M} \left(\frac{M_i - C_i}{\sigma_i} \right)^2 \tag{3.5}$$

where M_i, C_i and σ_i denote the measured value, the compute value and the error associated for the i-th measurements respectively, n_M denotes the number of the iteration cycle. During the iteration cycle, all the parameters are re-adjusted continuously until the minimizing value of χ^2 is obtained.

However, in order to minimize the process, the two functions of the equation (3.3), $P'(\psi)$ and $FF'(\psi)$ can be parameterized linearly in terms of α_n and γ_n using the basic function x^n, where α_n and γ_n are the linear coefficients with the distribution of J_T. Which are expressed as follows,

$$P'(\psi) = \sum_{n=0}^{n_P} \alpha_n x^n \tag{3.6}$$

$$FF'(\psi) = \sum_{n=0}^{n_F} \gamma_n x^n \tag{3.7}$$

Here, $x = (\psi - \psi_0)/(\psi_l - \psi_0)$ is the normalized poloidal flux enclosed by a particular flux surfaces, where ψ_0 is the value of ψ at the magnetic axis and ψ_l is the value of ψ for the last closed flux surface. n_P and n_F are the number of parameters which are determined depending on the amount of the experimental data available as well as on the sensitivity of the data.

3.3 EFIT code's Algorithm

There are eight steps to obtain the equilibrium solution by EFIT code; (1) read the magnetic data for fitting from input files that are created by the magnetic diagnostics during a pulse, (2) assumed the boundary value of the plasma, (3) assumed the plasma current profile, (4) compute the magnetic surface ψ_{ij}, (5) obtain the new boundary values of the plasma, (6) check the value of χ^2, for the minimum value of χ^2 end the process else go to next step, (7) recalculate the new boundary values of the plasma, and (8) update the plasma current profile then go to step (4) again.

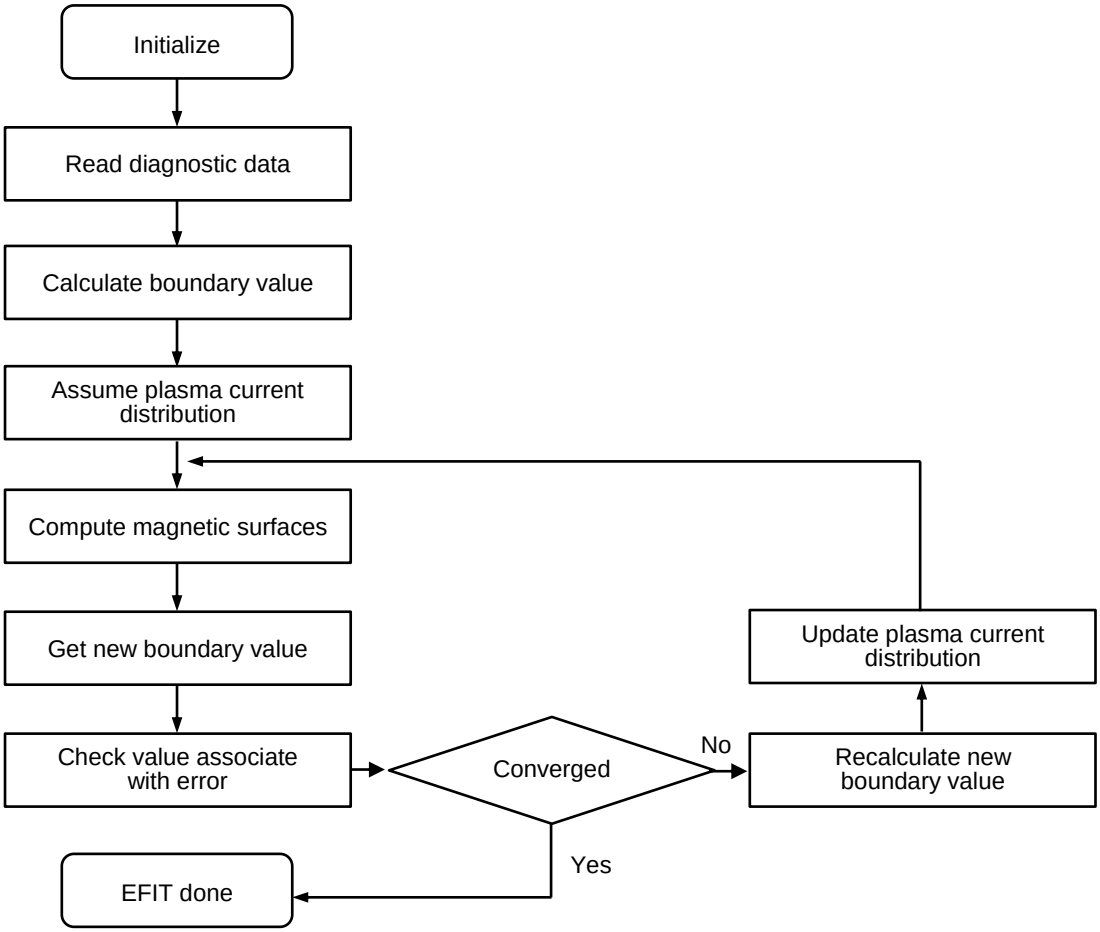

Figure 3.1: Flow chart of the EFIT code's steps to obtain equilibrium solution.

1. Initialization and read data

At this stage the code start to execute by choosing good initial approximation so that the entire computational time becomes less and read the external magnetic diagnostics data properly from the input file.

2. Assumed the boundary value of the plasma

In this process, the boundary values of the plasma are assumed. Here the poloidal flux ψ are divided into its two contributing parts as $\psi_b^{(m)} = \psi_b^{coils} + \psi_b^{(m,0)}$ in the computational domain, where the subscript b with ψ denotes the poloidal flux for the plasma boundary, ψ_b^{coils} denotes the poloidal flux contributed by the currents flowing in external toroidal coils and $\psi_b^{(m,0)}$ denotes the poloidal flux contributed by the plasma currents that is obtained using the latest

approximation of the J_T. Both terms are computed using the appropriate Green's function for toroidal current source. The contribution ψ_b^{coils} of the external coils is computed only at the beginning of the calculations. Thus, the matrices of the Green's functions need to be evaluated initially and stored for later using.

3. Assumed the plasma current distribution J_T

In this stage, the latest values of ψ obtained from the previous step are used to compute the values of current distributions. The current distribution estimation process is expressed in the equations (3.6) and (3.7) which can be written as,

$$J_T = R\sum_{n=0}^{n_P}\alpha_n x^n + \frac{1}{\mu_0 R}\sum_{n=0}^{n_F}\gamma_n x^n \tag{3.8}$$

The α_n and γ_n are the linear coefficients at the grid points of the EFIT code with the distributed plasma current. The poloidal flux ψ and toroidal current density J_T are calculated by dividing the poloidal (R,Z) plane from $R=0.15\,\text{m}$ to $R=1.4\,\text{m}$ and from $Z=-1\,\text{m}$ to $Z=+1\,\text{m}$ with 129×129 grid points where the plasma current is modeled as being distributed among these set of elements of the grid points with linear coefficients α_n and γ_n. These linear coefficients are determined from the diagnostics and the imposed constraints. The value of α_n and γ_n are adjusted at each step of the calculation to keep the total toroidal current I_T constant by evaluating the integral over the plasma cross-section.

4. Compute magnetic surface

To calculate the magnetic surfaces, the central difference equation can be used to represent the partial derivatives. In this case, the operator Δ^* can be written in the form as shown below,

$$\frac{\psi_{i-1,j}-2\psi_{i,j}+\psi_{i+1,j}}{(\Delta R)^2}+\frac{1}{R_i}\frac{\psi_{i-1,j}-\psi_{i+1,j}}{2\Delta R}+\frac{\psi_{i,j-1}-2\psi_{i,j}+\psi_{i,j+1}}{(\Delta Z)^2}=-2\pi\mu_0 R_i J_{T(i,j)} \tag{3.9}$$

where $\psi_{i,j}$ are the boundaries. The subscript, (i,j) denote the grid points. Since in the EFIT code, the poloidal plane (*R*,*Z*) is defined with 129×129 grid points from *R*=0.15 m to *R*=1.4 m and from $Z=-1\,\text{m}$ to $Z=+1\,\text{m}$. However, this equation is solved using double cyclic reduction in a form only slightly different from the usual application to Poisson's equation in cylindrical coordinate.

5. Compute the new boundary values of the plasma

To compute the new boundary value of the plasma in divertor configuration, first the possible X-points need to calculate. For the calculation of the possible X-points two regions are defined on the (R,Z) plane in case of double null divertor discharge where the X-point could appear. Then B_R and B_Z of the grid points inside the regions are calculated using the expression $B_R = -(1/R)(\partial\psi/\partial Z)$ and $B_Z = (1/R)(\partial\psi/\partial R)$. From the calculated magnetic field components, identified the grid point which has minimum, $B_R^2 + B_Z^2$. Then the accurate poloidal field B_R^a and B_Z^a on these two grid points and their adjunct grid points are computed using the pre-computed Green's function matrix multiply by the current vector. For every grid point, execute first order Taylor expansion of B_R^a and B_Z^a . Then a linear equation group is solved to locate the precise position of X-points. The poloidal flux at the X-point would be taken as the new boundary flux.

6. Check χ^2 value

In this stage, the equation (3.5) is executed to test the convergence of the inner repetition loop, if the error is less than a fixed number usually 10^{-6}, then the inner loop convergence test has been passed and the fitting is finished.

7. Recalculate the new boundary values of the plasma

The boundary values are considered to have converged when,

$$\left|\frac{\psi^{(m)} - \psi^{(m-1)}}{\psi_l - \psi_0}\right| \le \varepsilon_b \tag{3.10}$$

where ε_b is an input tolerance (usually 10^{-3}), m is the number of iteration process, ψ_0 is the value of ψ at the magnetic axis and ψ_l is the value of ψ for the last closed flux surface. If equation (3.10) is not satisfied, then calculate ψ_l again.

8. Update J_T

The step is similar as the step in (3).

3.4 Equilibrium Magnetic Fields

The tokamak equilibrium magnetic fields in the cylindrical coordinate (R,φ,Z), where the vertical *Z*-axis pointing in the direction of the torus axis of symmetry can be written as,

$$\bar{B} = \nabla\psi \times \nabla\varphi + g\nabla\varphi \tag{3.11}$$

Here, $\psi = \psi(R,Z)$ is the poloidal magnetic flux per radian, g is related to the poloidal current density which is defined as $g = RB_{\varphi}(R,Z)$.

The equation (3.11) can be written in the form of separate three components of the magnetic field as,

$$\bar{B} = B_R\hat{R} + B_Z\hat{Z} + B_{\varphi}\hat{\varphi} \tag{3.12}$$

where B_R and B_Z are the R and Z components of the magnetic field and B_{φ} is the toroidal magnetic field. All components are related to the plasma current and external coils currents.

The components of the magnetic field B_R, B_Z and B_{φ} of the axisymmetric equilibrium magnetic field can be written as,

$$\begin{aligned} B_R &= -\frac{1}{R}\frac{\partial\psi}{\partial Z} \\ B_Z &= \frac{1}{R}\frac{\partial\psi}{\partial R} \\ B_{\varphi} &= \frac{g(\psi)}{R} \end{aligned} \tag{3.13}$$

The poloidal flux function $\psi(R,Z)$ and g were calculated by the EFIT code. The magnetic field components B_R, B_Z and B_{φ} $\left(B_{\varphi} = B_T\right)$ defined in equation (3.13) were also calculated from the output of the poloidal flux function $\psi(R,Z)$ and g of the EFIT code.

Finally, the absolute value of the total magnetic field $\bar{B}$ was calculated also in the EFIT code according to the equation written as,

$$|B| = \frac{1}{R}\sqrt{\left(\frac{\partial\psi}{\partial R}\right)^2 + \left(\frac{\partial\psi}{\partial Z}\right)^2 + g^2} \tag{3.14}$$

3.5 Experimental Plasma Parameters for the EFIT code

The equilibrium reconstruction for QUEST plasma discharge was performed for the shot no.16499. In the discharge, the plasma was initiated by the electron cyclotron heating of 8.2 GHz ECH/CD waves and the plasma current was started-up, ramped-up and sustained by the 8.2 GHz ECH/CD waves where the toroidal magnetic field was $B_t = 0.125\,\mathrm{T}$ at the major radius $R = 0.68$ m. Figure 3.2 (a) shows the toroidal magnetic field at $R = 0.68\,\mathrm{m}$ and figure 3.2 (b) shows the injected power of ECH waves where the input power and net power are shown in different curves.

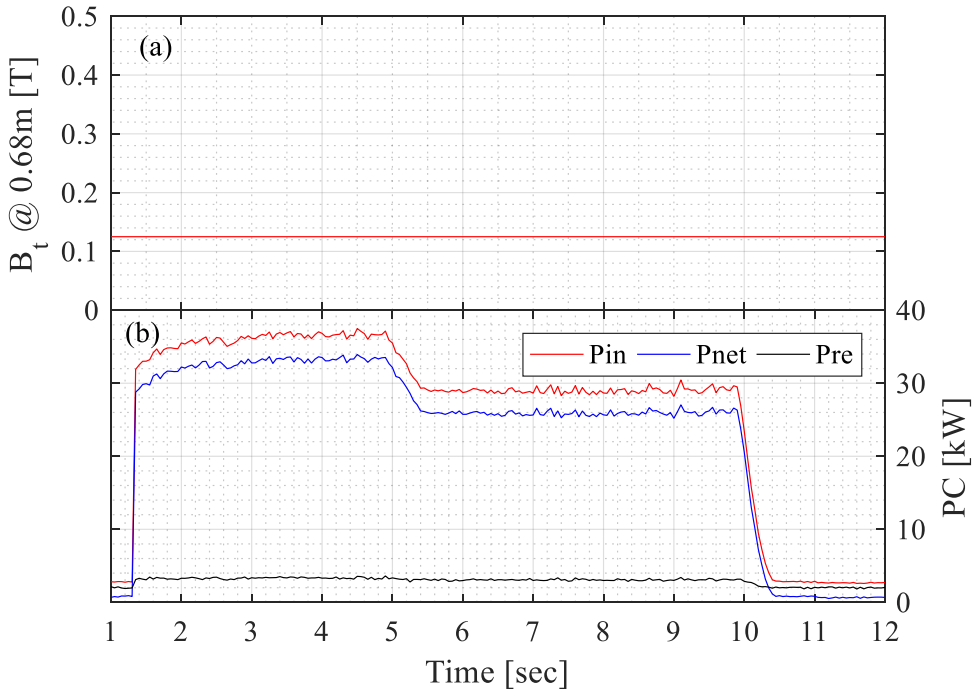

Figure 3.2: The toroidal magnetic field and the injected power of the ECH waves of the discharge of shot no. 16499. (a) The toroidal magnetic field B_t at the major radius $R = 0.68\,\mathrm{m}$, (b) the injected power of the waves of the ECH/CD where the input power and net power are shown in different curves.

Figure 3.3 shows time evaluation graphs of the plasma current and the external coils currents during the discharge. The plasma was started-up, ramped-up and sustained by the ECH waves. Figure (a) and (b) show the measured plasma current and the poloidal field coils currents, respectively. The plasma current and the poloidal field coils currents were recorded as $I_p = -14.243$ kA, $I_{PF17} = 0.2$ kA, $I_{PF26} = 0.5$ kA, $I_{PF35} = -0.29$ kA and $I_{PF4} = 0.35$ kA at

$t = 5.00$ sec., where PF4 denotes the center solenoid coils, PF17 denotes the vertical field coils with negative n-index, PF26 denotes the vertical field coils with positive n-index, PF35-1 denotes the inner divertor coils and PF35-2 denotes the outer divertor coils. In the discharged, the plasma was pulled by the PF35-12 divertor coils and pushed from the inside by PF4 center solenoid coils. These values of the plasma current and the toroidal field coils currents at $t = 5.00$ sec. were fitted to the EFIT code.

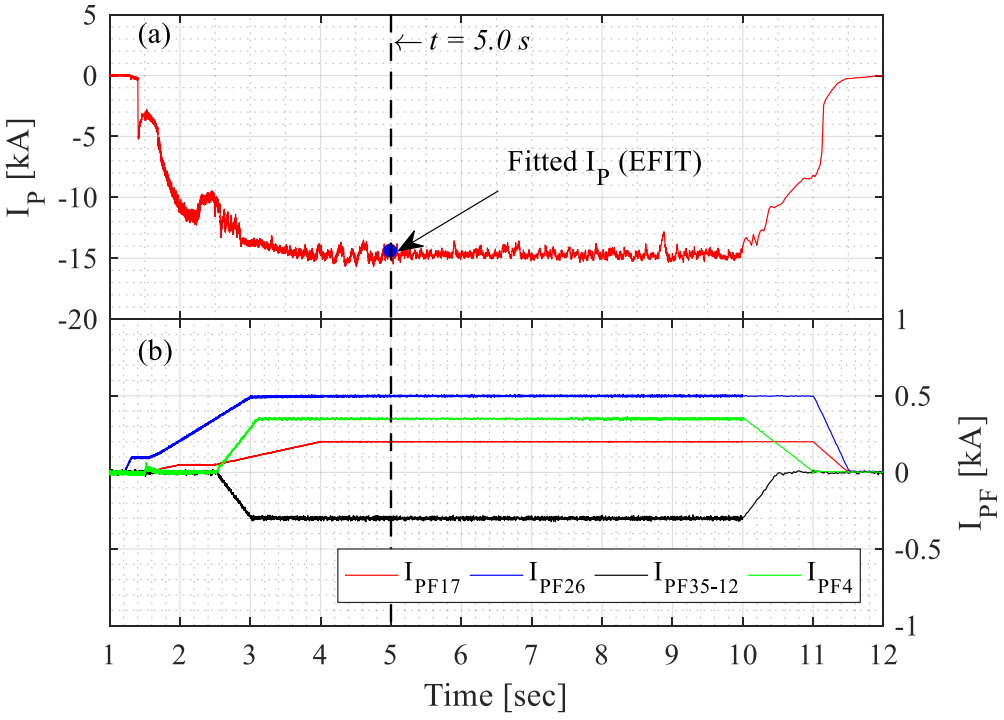

Figure 3.3: The plasma current and the poloidal field coils currents of the shot no. 16499. (a) Shows the measured plasma current and the fitted plasma current to the EFIT code. The fitted plasma current was -14.243 kA, which was obtained at $t = 5.00$ second. (b) Shows the poloidal field coils currents.

Figure 3.4 shows the vacuum magnetic fields of the shot no. 16499 where the n-index (decay index of the vertical magnetic field) of the vertical magnetic field was zero at $R = 0.60$ m. The n-index was negative in the high field side of $R = 0.60$ m and n-index was positive in the low field side. Figure 3.5 shows the time evaluation graphs of the emission of H_α and transport of the oxygen impurity on the wall. Figures (a) and (b) show the emission of H_α and the transport of the oxygen impurity, respectively.

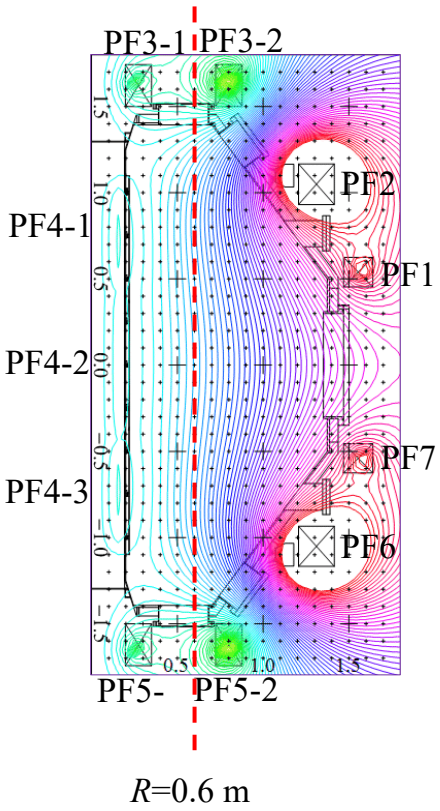

Figure 3.4: The vacuum magnetic fields of the shot no. 16499. The n-index (decay index of the vertical magnetic field) of the vertical magnetic field is zero at $R = 0.60\,\mathrm{m}$.

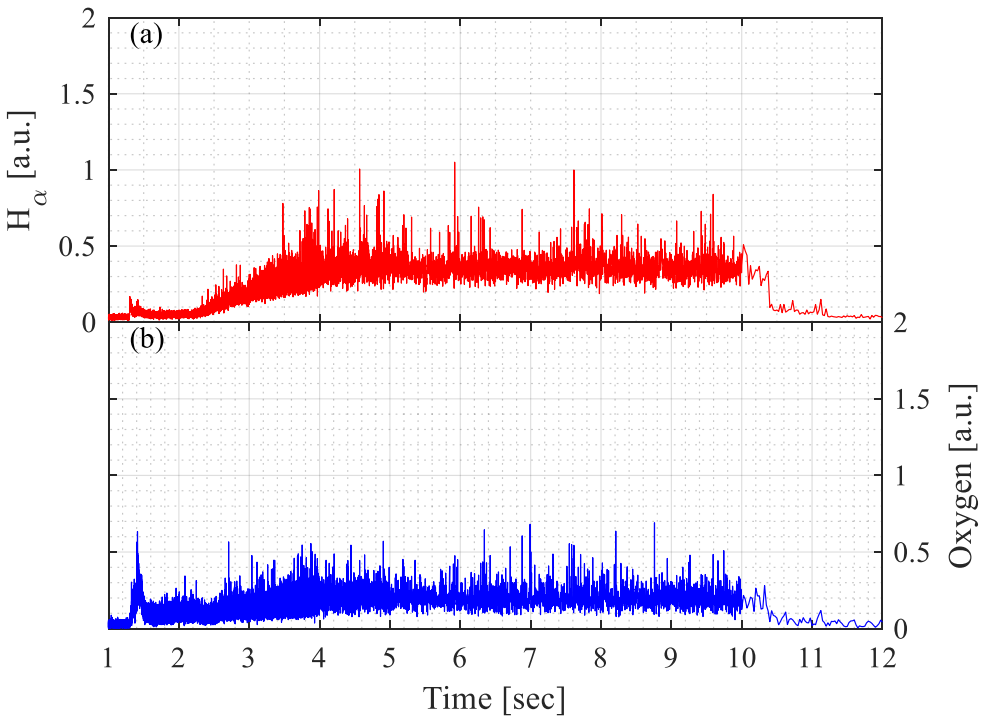

Figure 3.5: Time evaluation graph of the emission of H_α and transport of the oxygen impurity on the wall, (a) the emission of H_α, (b) the emission of oxygen.

3.6 Plasma Equilibrium Solution for QUEST plasma discharge

According to the algorithm of the EFIT code and depending on the fitted data of the shot no. 16499, the equilibrium parameters such as plasma pressure P, current flux function F, poloidal flux ψ, poloidal beta β_p and the other parameters of plasma shape and position are obtained [39]. Figure 3.6 shows the contour plot of B_φ obtained from the EFIT code where the deviation of the magnetic field indicated by the dotted circle appears due to the presence of the plasma, figure 3.7 shows the contour plot of B_R and figure 3.8 shows the contour plot of B_Z those are obtained from the output of the poloidal flux function of the EFIT code. In the figures 3.7 and 3.8, the red contours indicate positive n-index and blue contours indicate negative n-index of the magnetic field. Figure 3.9 shows the equilibrium magnetic configuration obtained from the EFIT code. The guiding center orbits calculations are carried out on this equilibrium magnetic configuration. The red-colored contours indicate the closed flux surfaces while the green-colored contours indicate the open magnetic surfaces which are terminated at the divertor plates.

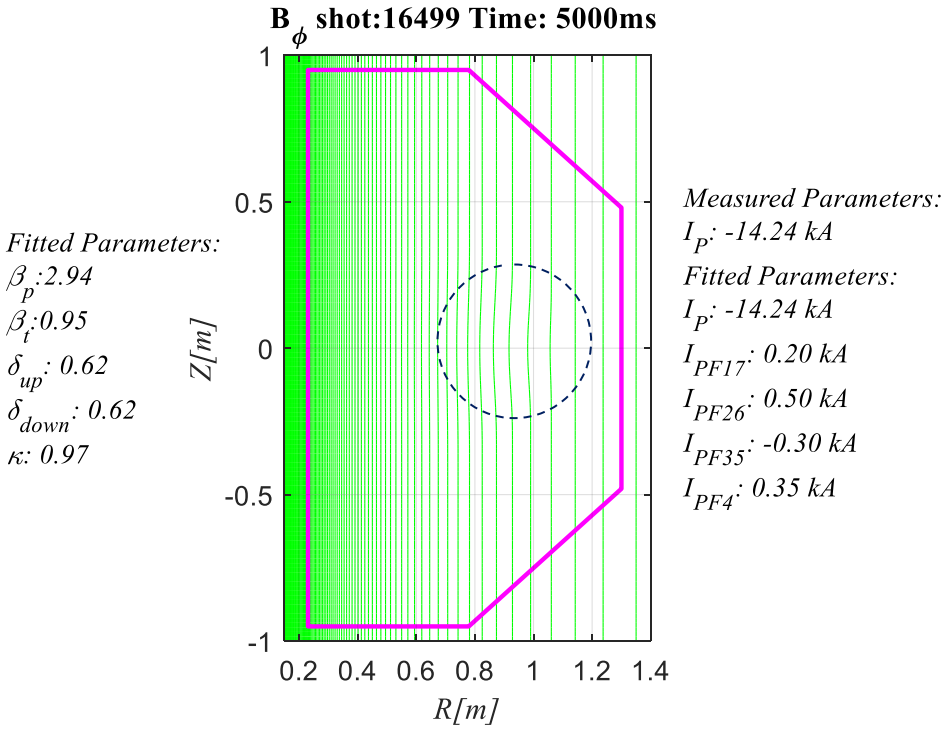

Figure 3.6: The contour plot of B_φ obtained from the EFIT code where the deviation of the magnetic field indicated by the dotted circle appears due to the presence of the plasma.

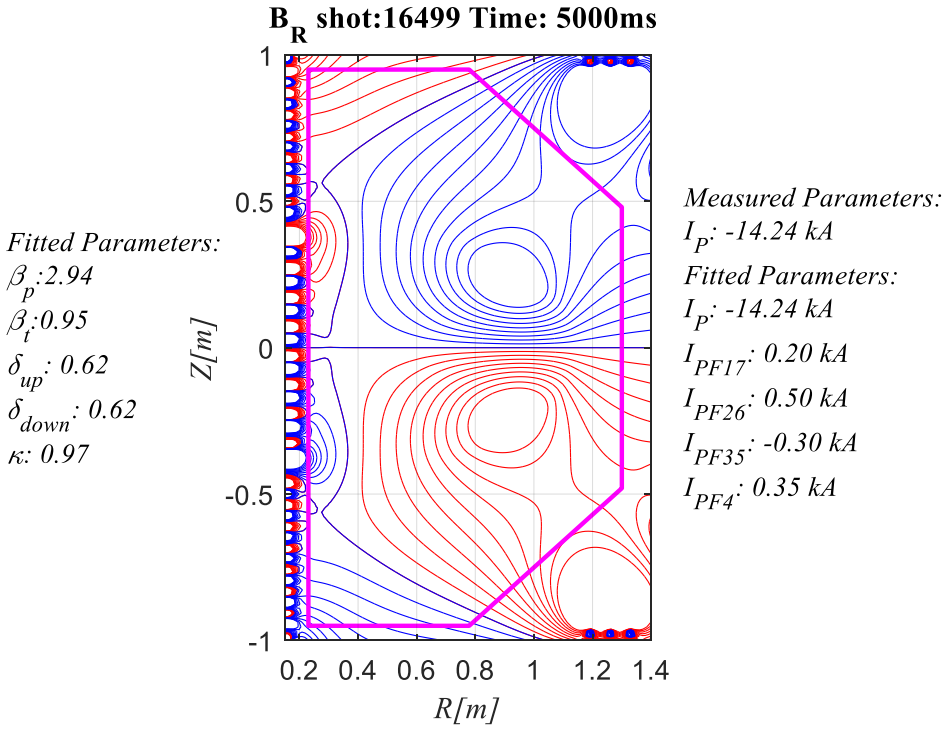

Figure 3.7: The contour plot of B_R obtained from EFIT code calculated from the poloidal flux function ψ (red indicates the positive and blue indicates the negative n-index).

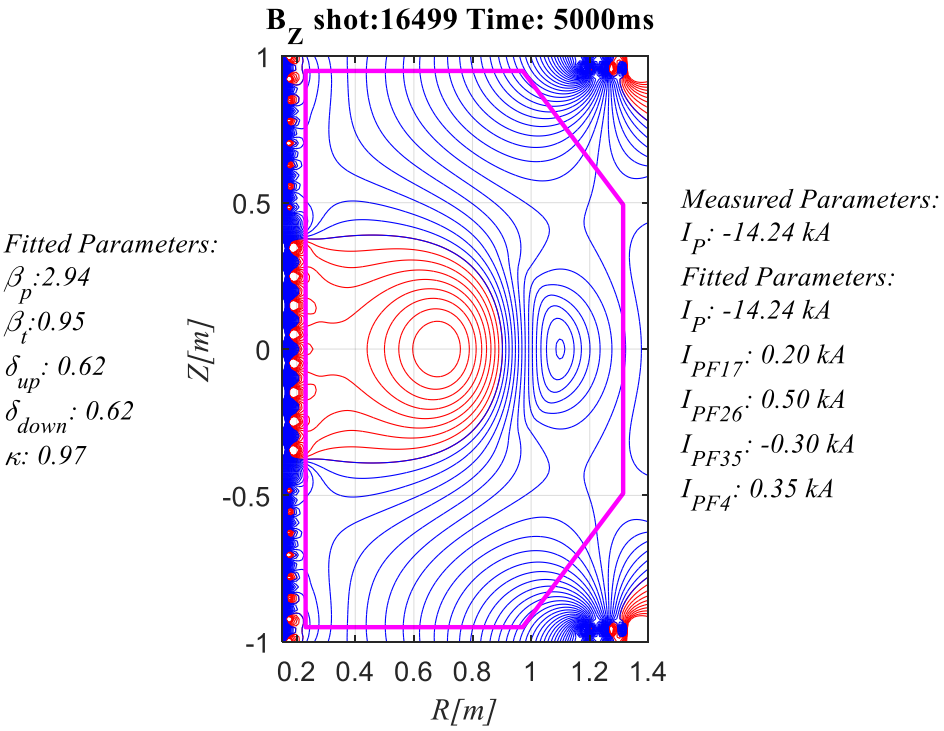

Figure 3.8: The contour plot of B_Z obtained from EFIT code calculated from the poloidal flux function ψ (red indicates the positive and blue indicates the negative n-index).

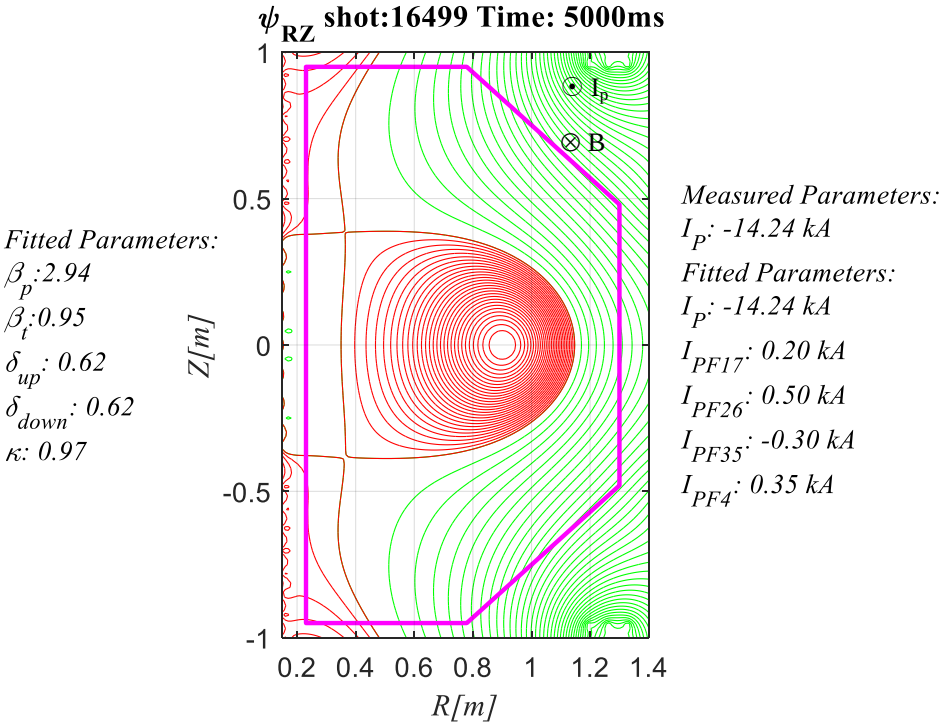

Figure 3.9: The equilibrium magnetic configuration obtained from the EFIT code. The red-colored contours indicate the closed flux surfaces while the green-colored contours indicate the open magnetic surfaces which are terminated at the divertor plates. Guiding center orbits calculations are carried out on this equilibrium magnetic configuration.

Chapter 4

Guiding Center Orbits Calculations

4.1 Introduction

The guiding center orbits of the electron cyclotron resonance (ECR) electrons were calculated and analyzed under equilibrium magnetic configuration for the 8.2 GHz electron cyclotron heating and current drive (ECH/CD) waves. The Doppler shifted fundamental and second (2^{nd}) harmonic as well as non-relativistic and relativistic ECR was considered separately. The parallel $v_{||}$ and perpendicular $v_{\perp}$ velocities to the magnetic field were considered from the Doppler-shifted ECR condition for the electrons to be resonant with the ECH waves. The parallel refractive index $N_{||}$ from -1 to $+1$ with step 0.1 was taken into account in the multiple-wall reflection model [40]. The maximum energy of the resonant electrons was restricted at 100 keV and calculated the orbits of those electrons whose energies were between 1 to 100 keV. Though it was observed that the electrons with energy of about several hundred MeV were also resonant with the ECH waves but the upper limit of the resonant energy was still critical and unknown. The orbit trajectory of an ECR electron was obtained as a contour plot of the resonant electrons' energy on the equilibrium magnetic configuration where the energy was expressed in terms of magnetic moment and toroidal angular momentum. The energy, magnetic moment and toroidal angular momentum were conserved in the orbit trajectories. All the resonant and confined electrons' orbits trajectories were obtained for various positions of the coordinates (R,Z), pitch angles and parallel refractive index. Depending on these initial conditions, the number of the step parameters was more than 5,200000. The toroidal magnetic field was $B_t = 0.125\,\mathrm{T}$ at $R = 0.68\,\mathrm{m}$. The fundamental and the second harmonic resonance layers were located at $R_{First} = 0.29\,\mathrm{m}$ and $R_{Second} = 0.58\,\mathrm{m}$ of the major radius respectively. Figure 4.1 shows the fundamental and the second harmonic electron cyclotron resonance frequencies f_{ce} and $2f_{ce}$ as a function of major radius R. From the mid-plane i.e. from $Z = 0$ two divertor plates were set after $\pm 1\,\mathrm{m}$ where the open magnetic field lines were terminated. The inboard and the outboard plasma boundaries were controlled by limiter placed at $R = 0.22\,\mathrm{m}$ and $R = 1.31\,\mathrm{m}$ of the major radius respectively.

In this chapter, the ECR electrons' guiding center orbits calculations processes as well as the characteristics of the obtained orbits were discussed for the non-relativistic and the relativistic electrons separately.

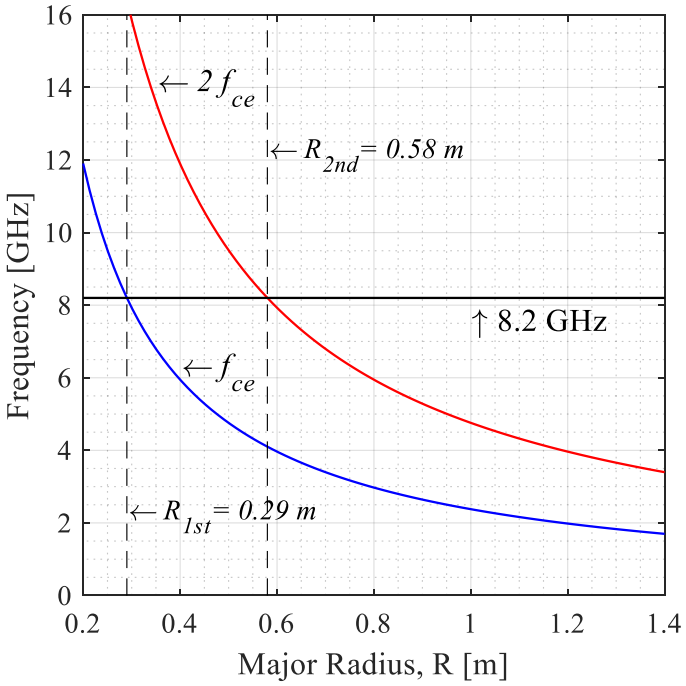

Figure 4.1: The fundamental and the second harmonic electron cyclotron resonance frequencies f_{ce} and $2f_{ce}$. The toroidal magnetic field was $B_t = 0.125\,\mathrm{T}$ at $R = 0.68\,\mathrm{m}$. The fundamental and 2nd harmonic resonance layers were located at $R_{First} = 0.29\,\mathrm{m}$ and $R_{Second} = 0.58\,\mathrm{m}$ respectively.

4.2 Non-Relativistic Electron Cyclotron Resonance

4.2.1 Wave-electron Resonance

In tokamak plasma, an electron gyrates around a magnetic field line and the guiding center of the electron moves along the magnetic field line which encircles the plasma torus by the Lorentz force. This gyro-frequency of the electron is known as electron cyclotron frequency f_{ce}, which is proportional to the strength of the magnetic field line [41]. As the strength of the magnetic field in tokamak decreases monotonically with the major radius, the electron cyclotron frequency also decreases consequently. In electron cyclotron heating (ECH), the waves are launched into the

plasma where the waves' frequency is chosen according to the cyclotron frequency for any specific position of major radius. Thus, the waves-electrons interactions are occurred and the waves' energies are absorbed by the resonant electrons. The width of the waves-electrons interactions area is affected by the frequency shifted through the Doppler effect, electron temperature, direction of the wave vector and the strength of the magnetic field. Here, two schemes are possible; downshift and upshift [42]. In the downshift scheme, the waves-electrons interactions as well as waves' energy absorption are occurred on the high field side from the resonance layer, while in the upshift scheme the waves-electrons interactions as well as waves' energy absorption are occurred on the low field side from the resonance layer. Both in the downshift and downshift schemes the absorption occurs on one side of the resonance surface but in combination of them, the absorption occurs on the both sides of the resonance surface.

However, the non-relativistic ECR condition can be written as,

$$\omega - n\omega_{ce} = k_{||} v_{||} \tag{4.1}$$

Here, ω is the angular frequency of the ECH waves, n is the harmonic number, ω_{ce} is the angular electron cyclotron frequency, $k_{||}$ is the parallel wave number and $v_{||}$ is the resonant electron's parallel velocity. In ECH, waves' energy transfer to the plasma by means of electromagnetic wave. The electric field of the electromagnetic wave is coupled with the electron when initial parallel velocity of the electron satisfied the parallel velocity $v_{||}$ obtain from the equation (4.1). In the equation (4.1), the value of the $v_{||}$ depends on the value of $k_{||}$. The value of $k_{||}$ can be obtained by the equation,

$$N_{||} = ck_{||} / \omega \tag{4.2}$$

Here, $N_{||}$ is the parallel refractive index, c is the velocity of the light. For a particular value of $N_{||}$, the value of the $k_{||}$ can be obtained from the equation (4.2). By using this value, the parallel velocity $v_{||}$ can be calculated by the equation (4.1) for a particular initial position in the real space. The obtained parallel velocity is the initial parallel velocity of the electron to be resonant with the ECH waves.

The waves' energy absorption region as well as minimum initial energy of an electron required to be resonant with the waves can be explained from the equation of the ECR condition. The waves' energy absorption region is increased as the value of the parallel refractive index $N_{||}$ increase.

Figure (4.2) and (4.3) show the waves' energy absorption region and minimum initial energy required to be resonant for the fundamental and 2nd harmonic ECR, respectively where the absorption regions are evaluated for the parallel refractive index $N_{||} = 0.50$ and $N_{||} = 0.99$ and the maximum energy is restricted at 100 keV. From the figure, it has been observed that the waves' energy absorption region as well as minimum initial energy required to be resonant for an electron are increased as the value of the $N_{||}$ increase. Compared with the fundamental resonance the absorption region is larger for the 2nd harmonic resonance for the same values of $N_{||}$ as shown in the two figures. Such phenomenon is also observed for the negative values of $N_{||}$.

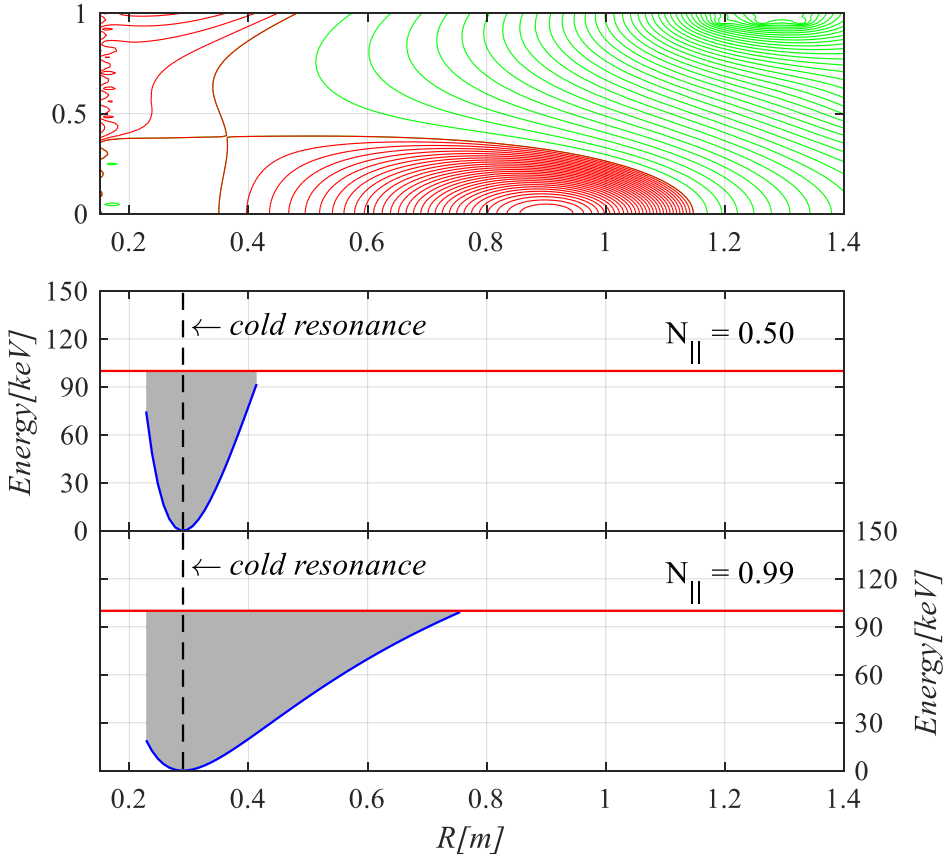

Figure 4.2: The waves' energy absorption region and minimum initial energy required to be resonant for the fundamental ECR. The absorption regions are evaluated for the parallel refractive index $N_{||} = 0.50$ and $N_{||} = 0.99$ and the maximum energy is restricted at 100 keV. The top figure shows the upper part of the equilibrium closed and opened magnetic surfaces on the poloidal cross-section, cutting along the equatorial plane.

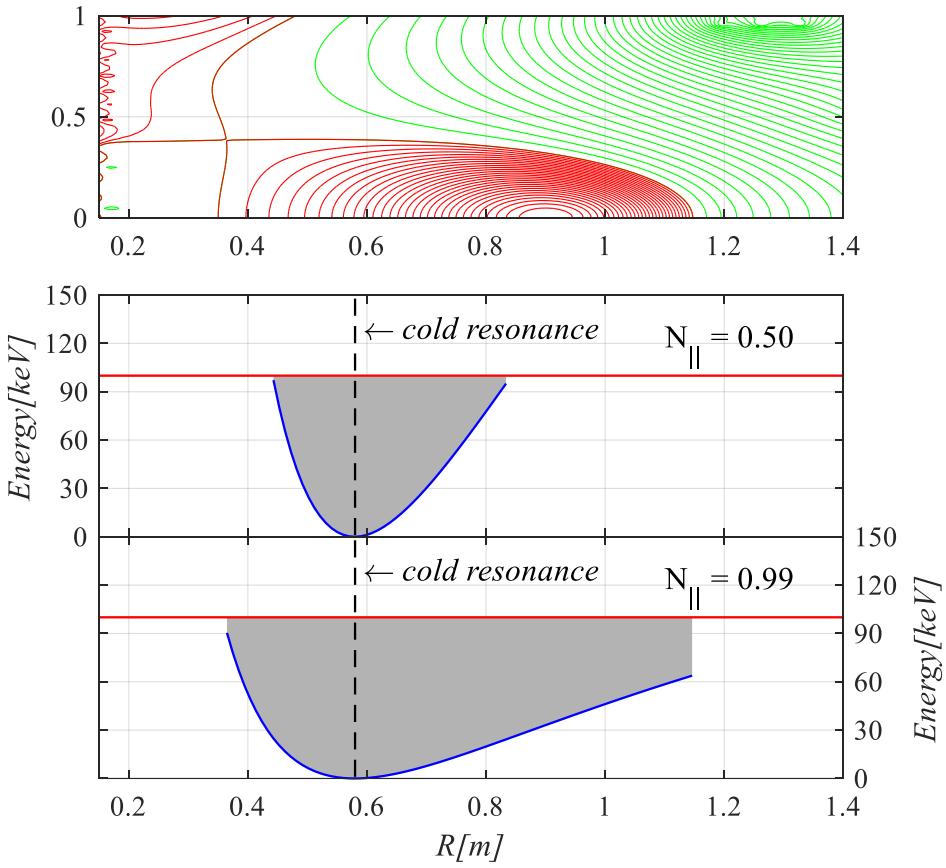

Figure 4.3: The waves' energy absorption regions and minimum initial energy required to be resonant for the 2nd harmonic ECR. The absorption regions are evaluated for the parallel refractive index $N_{||} = 0.50$ and $N_{||} = 0.99$ and the maximum energy is restricted at 100 keV. The top figure shows the upper part of the equilibrium closed and opened magnetic surfaces on the poloidal cross-section, cutting along the equatorial plane.

The pitch angles distribution of the resonant electrons can be also explained from the equation of the ECR condition. For a particular initial position on (R,Z), the parallel velocity $v_{||}$ is calculated from the equation (4.1). The obtained $v_{||}$ is the initial parallel velocity of the electron to be resonant with the waves. The pitch angle as well as $v_{\perp}$ of the electron of energy 100 keV is determined by the obtained $v_{||}$ for that initial position. Then for the different energies between 1 keV to 100 keV, the pitch angle as well as $v_{\perp}$ are determined. Figure 4.4 shows the pitch angles distribution of the resonant electrons in the velocity $(v_{||}, v_{\perp})$ space. The pitch angles distribution is evaluated for the down-shifted and up-shifted ECR separately. Figure 4.5 shows the pitch angles

distribution of the energy range 1 keV to 100 keV for the different initial positions on R for the 2nd harmonic ECR, where $R = 0.58$ m is the location of cold resonance.

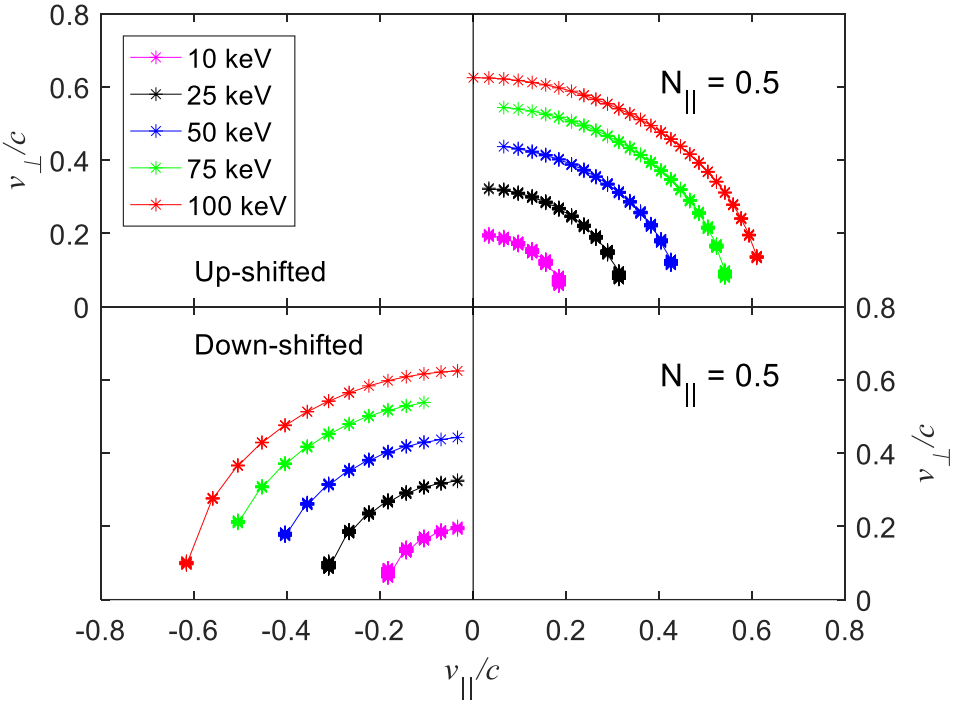

Figure 4.4: The pitch angles distribution of the resonant electrons in the velocity $(v_{\|}, v_{\perp})$ space for the 2nd harmonic ECR. The pitch angles distribution is evaluated for the down-shifted and the up-shifted ECR separately.

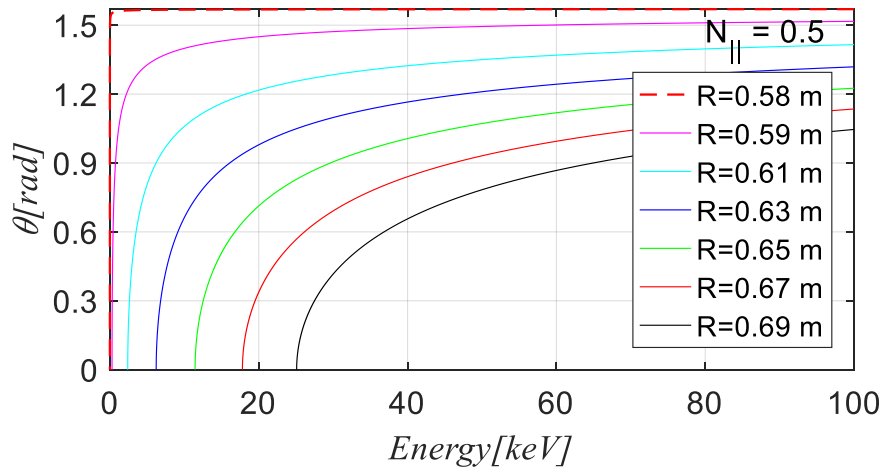

Figure 4.5: The pitch angles distribution of the energy range 1 keV to 100 keV for the different initial position on R for the 2nd harmonic ECR. $R = 0.58$ m is the location of the cold resonance.

4.2.2 Equations of the Guiding Center Orbit

The guiding center orbits for the non-relativistic ECR electrons were calculated from the conservation of the energy E, magnetic moment μ and toroidal angular momentum p_φ and by the equations expressed as follows,

$$E = \frac{1}{2} m\left(v_{\|}^2 + v_{\perp}^2\right) \tag{4.3}$$

$$\mu = \frac{m v_{\perp}^2}{2B} \tag{4.4}$$

$$p_\varphi = mRv_{\|}\frac{B_t}{B} + q\psi \tag{4.5}$$

where m and q are the mass and elementary charge of an electron, $v_{\|}$ and $v_{\perp}$ are the parallel and perpendicular velocities of the electron, B and B_t are the total and toroidal magnetic field strength, respectively. R is the major radius and ψ is the flux function. From equations (4.3) - (4.5) the following equation was obtained,

$$E = \frac{\left(p_\varphi - q\psi\right)^2}{2mR^2}\left(\frac{B}{B_t}\right)^2 + \mu B \tag{4.6}$$

The energy E in equation (4.6) was expressed in terms of the magnetic moment and the toroidal angular momentum. The contour line of this energy on equilibrium magnetic configuration was expressed the guiding center orbit of the resonant electron. The parallel and perpendicular, $v_{\|}$ and $v_{\perp}$ velocities as well as pitch angles distribution were obtain from the Doppler shifted non-relativistic ECR and B_t, B and ψ were obtained from the EFIT plasma equilibrium solution.

4.2.3 How to Calculate Orbits

To calculate resonant electron's guiding center orbits by the above equations, first, the orbit of the resonant electron of energy 100 keV was calculated because the maximum resonant energy of the electrons was set 100 keV for these calculations. In order to calculate the orbit of the resonant electron of energy 100 keV, the value of the parallel wave number $k_{\|}$ was determined for a particular value of the parallel refractive index $N_{\|}$ from the equation $N_{\|} = ck_{\|}/\omega$, where ω is angular frequency of the ECH waves and c is the velocity of the light. Then for a particular initial position on (R, Z) and for the obtained parallel wave number, the parallel velocity $v_{\|}$ was

calculated from the equation (4.1). The obtained $v_{\|}$ was the initial parallel velocity of the electron to be resonant with the ECH waves. After that the total velocity v for the electron of energy 100 keV was calculated from the equation, $v=\left(2E/m\right)^{1/2}$. Then by combining the obtained $v_{\|}$ from equation (4.1) and v for the electron of 100 keV, the perpendicular velocity $v_{\perp}$ as well as pitch angle were calculated from the equation $v^2=v_{\|}^2+v_{\perp}^2$ and $\theta=\cos^{-1}\left(v_{\|}/v\right)$, respectively. The obtained $v_{\|}$, $v_{\perp}$ and pitch angle θ were the initial conditions for the electron of energy 100 keV to be resonant. Then the magnetic moment μ and the toroidal angular momentum p_{φ} were calculated from the equation (4.4) and (4.5) by using these obtained values of $v_{\|}$ and $v_{\perp}$. Finally, by the equation (4.6), E was determined where the values of the B_t, B and ψ were obtained from the EFIT plasma equilibrium solution. The contour plot of the energy on the equilibrium magnetic configuration expressed the guiding center orbit of the resonant electron of energy 100 keV [43]. Here, the energy, magnetic moment and toroidal angular momentum were conserved throughout the orbit. Then by scanning the initial pitch angles from 0 to $\pi/2$ rad for up-shifted and $\pi/2$ to π rad for down-shifted ECR with a step of 0.1, all the resonant electrons' orbits of energies between 1 keV to 100 keV were obtained for that initial position. These processes were repeated for different positions of the coordinates $\left(R,Z\right)$ as well as different values of $N_{\|}$. Here, at the initial positions $\left(f<nf_{ce}\right)$, the down-shifted ECR was occurred and the electrons' initial $v_{\|}$ became negative for $N_{\|}>0$ and the electrons' initial $v_{\|}$ became positive for $N_{\|}<0$. At the initial positions $\left(f>nf_{ce}\right)$, the up-shifted ECR was occurred and the electrons' initial $v_{\|}$ became negative for $N_{\|}<0$ and the electrons' initial $v_{\|}$ became positive for $N_{\|}>0$.

The red and blue contours in figure 4.6 show the guiding center orbits for the initial position $(R,Z)=$(0.47 m, 0.0 m) of fundamental passing resonant electrons. The two figures represent the orbits of the two electrons. The two orbits were obtained separately because of their initial $v_{\|}$. The left figure shows the orbit of the electron of initial positive $v_{\|}$ (initial parallel velocity that is parallel to the magnetic field) and the right figure shows the orbit of the electron of initial negative $v_{\|}$ (initial parallel velocity that is antiparallel to the magnetic field). Additionally, due to mirror forces some electrons were trapped at the low field side region and produced banana orbits. This phenomenon was occurred for both the electrons with initial positive and negative $v_{\|}$. The red and blue color contours in figure 4.7 shows the guiding center orbits of the trapped electrons for the initial position $(R,Z)=$(0.56 m, 0.23 m) of second harmonic resonant electrons. Due to mirror force these electrons were trapped and maintained banana orbits. The left and right figure show the banana orbit of the electron of initial positive $v_{\|}$ and initial negative $v_{\|}$, respectively.

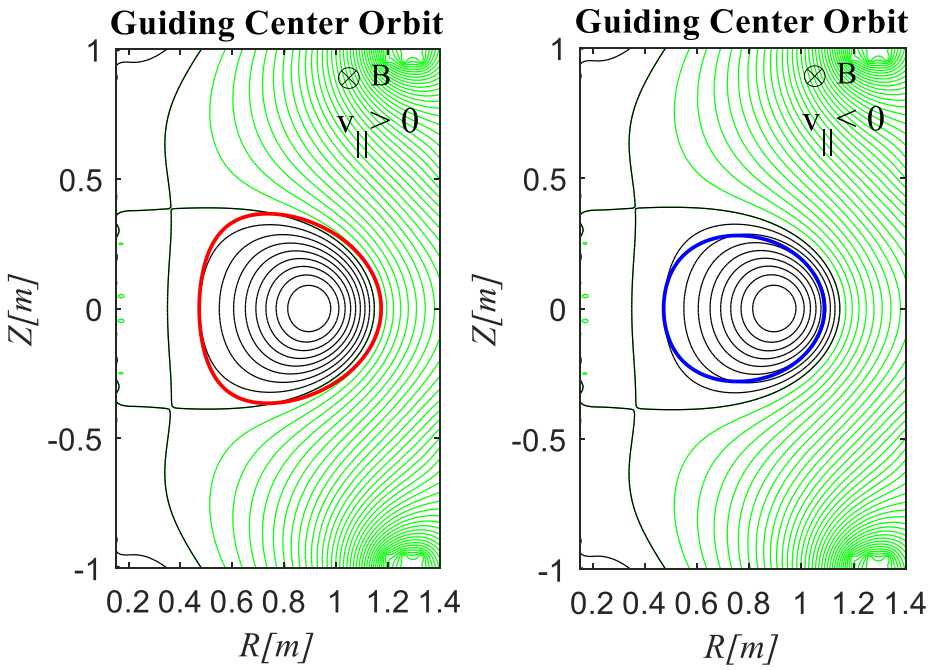

Figure 4.6: The red and blue contours indicate the guiding center orbits of the passing resonant electrons. The black and green contours indicate the closed and opened magnetic surfaces, respectively.

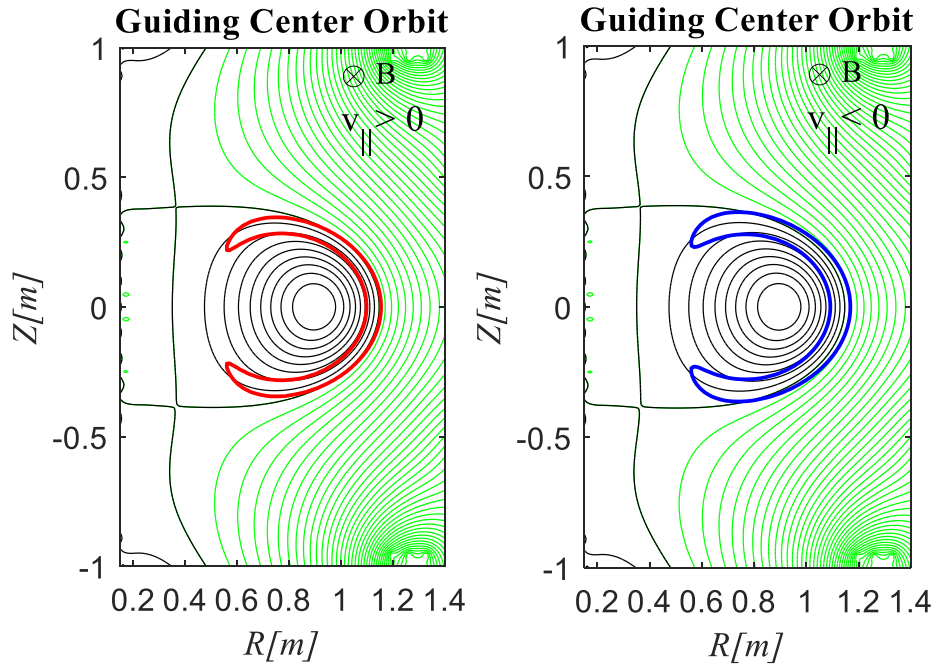

Figure 4.7: The red and blue contours indicate the banana orbits of the trapped resonant electrons. The black and green contours indicate the closed and opened magnetic surfaces, respectively.

However, the characteristics of the resonant electrons' guiding center orbits, the attributes of the confined and lost electrons and their effect on current contribution were analyzed and discussed for the fundamental as well as for the 2nd harmonic resonant electrons separately.

4.2.4 Fundamental Resonant Electrons

The fundamental resonance layer was located at $R_{First} = 0.29\,\text{m}$. The guiding center orbits were calculated from the inboard limiter $R = 0.22\,\text{m}$ to $R = 1.15\,\text{m}$ horizontally and from $Z = 0.00\,\text{m}$ to $Z = \pm 0.40\,\text{m}$ vertically of the (R, Z) plane. The orbits calculations were restricted to those positions because in equilibrium magnetic configuration as shown in figure 3.9, the outboard separatrix of the LCFS was located at $R = 1.15\,\text{m}$ and vertically $Z = \pm 0.40\,\text{m}$ from the mid-plane. Beyond this position, the resonant electrons were lost due to open magnetic field lines and had no contribution on current. The waves' energies were absorbed by the resonant electrons between the regions of $R = 0.22\,\text{m}$ to $R = 0.75\,\text{m}$ of the major radius for $N_{\|} = 0.99$ as shown in the figure 4.2. But the plasma inboard separatrix was located at $R = 0.35\,\text{m}$. Therefore, the resonant electrons from the inboard limiter $R = 0.22\,\text{m}$ to the inboard separatrix $R = 0.35\,\text{m}$ were also lost and had no contribution on current. Thus the electrons with initial positions between the regions $R = 0.35\,\text{m}$ to $R = 0.75\,\text{m}$ were confined and maintained steady-state orbits.

Depending on the initial positions and the value of the parallel refractive index, the ECR electrons were travelled both in the parallel and the antiparallel directions to the magnetic field after the interaction with the ECH waves. The electrons with initial positive $v_{\|}$ (electrons that traveled in the parallel direction to the magnetic field) were maintained spread orbits while the electrons with initial negative $v_{\|}$ (electrons that traveled in the antiparallel direction to the magnetic field) were maintained shrink orbits. Due to the drifts of the guiding centers, these two informative phenomena were observed with the evaluated orbits. Therefore, a large number of resonant electrons with initial positive $v_{\|}$ were maintained orbits outside the LCFS while all of the resonant electrons with initial negative $v_{\|}$ were maintained orbits inside the LCFS. The red and blue color contours in the figure 4.8 shows the guiding center orbits of the resonant electrons between the R positions from 0.35 m to 0.75 m and $Z = 0.00\,\text{m}$, where the black and green contours show the closed and open magnetic surfaces, respectively. The number of the actually calculated orbits were much large than the orbits shown in the figure. The left figure shows the

orbits of the electrons with initial positive $v_{||}$. The right figure shows the orbits of the electrons with initial negative $v_{||}$.

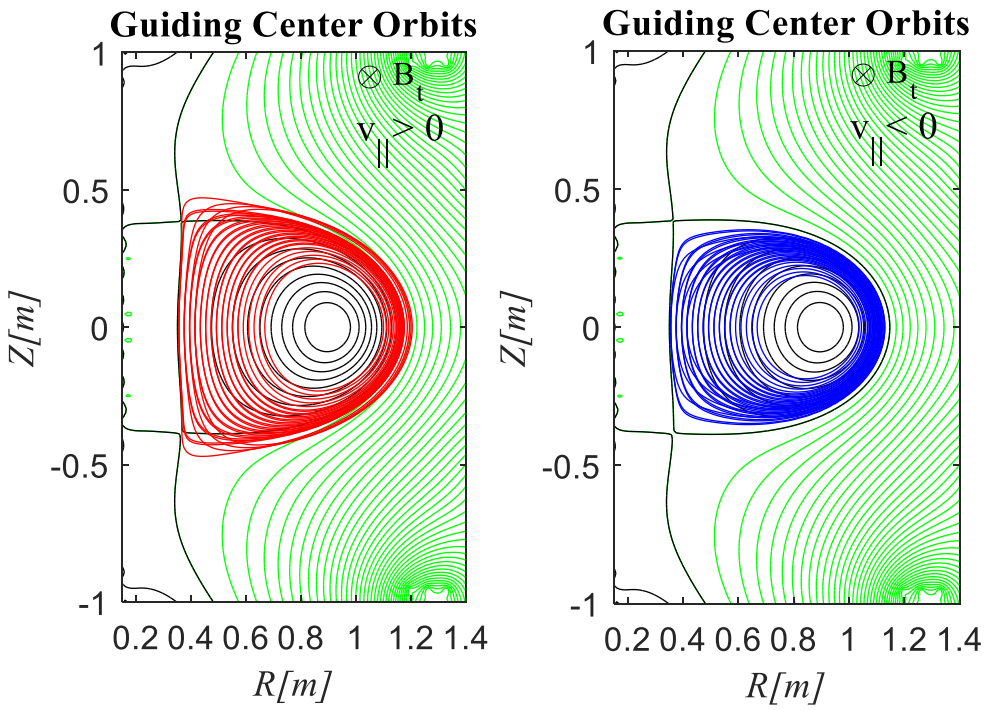

Figure 4.8: The red and blue contours indicate the guiding center orbits of the fundamental resonant electrons between the R positions from 0.35 m to 0.75 m and $Z = 0.00\,\mathrm{m}$ where the black and green contours show the closed and opened magnetic surfaces, respectively. The number of the actually calculated orbits were much large than the orbits shown in the figure. The left and right figures show the orbits of the electrons with initial positive and negative $v_{||}$, respectively.

4.2.5 Second Harmonic Resonant Electrons

The second harmonic resonance layer was located at $R_{\mathrm{Sec}ond} = 0.58\,\mathrm{m}$. The guiding center orbits were also calculated from the inboard limiter $R = 0.22$ m to $R = 1.15$ m horizontally and from $Z = 0.00\,\mathrm{m}$ to $Z = \pm 0.40$ m vertically. Like the fundamental resonance condition, the calculations were restricted to those positions because beyond this position, the resonant electrons were lost due to open magnetic field and had no contribution on current. In 2nd harmonic ECR, the waves' energy was absorbed by the electrons between the regions of $R = 0.36$ m to $R = 1.15$ m of the

major radius for $N_{||} = 0.99$ as shown in the figure 4.3. Thus, the electrons with initial positions between the regions were confined and maintained steady-state orbits. Depending on the initial positions and the value of the parallel refractive index, here the ECR electrons were also travelled both in the parallel and the antiparallel directions to the magnetic field. A large number of resonant electrons with initial positive $v_{||}$ were maintained orbits outside the LCFS while all of the resonant electrons with initial negative $v_{||}$ were maintained orbits inside the LCFS. In the figure 4.9, the red and blue contours show the orbits of the passing resonant electrons between the R positions from 0.60 m to 0.77 m and $Z = 0.00\,\text{m}$. The black and green contours in the figure show the closed and opened magnetic surfaces, respectively. The number of actually calculated orbits were much large than the orbits shown in the figure. The left figure shows the orbits of the electrons of initial positive $v_{||}$ and the right figure shows the orbits of the electrons of initial negative $v_{||}$.

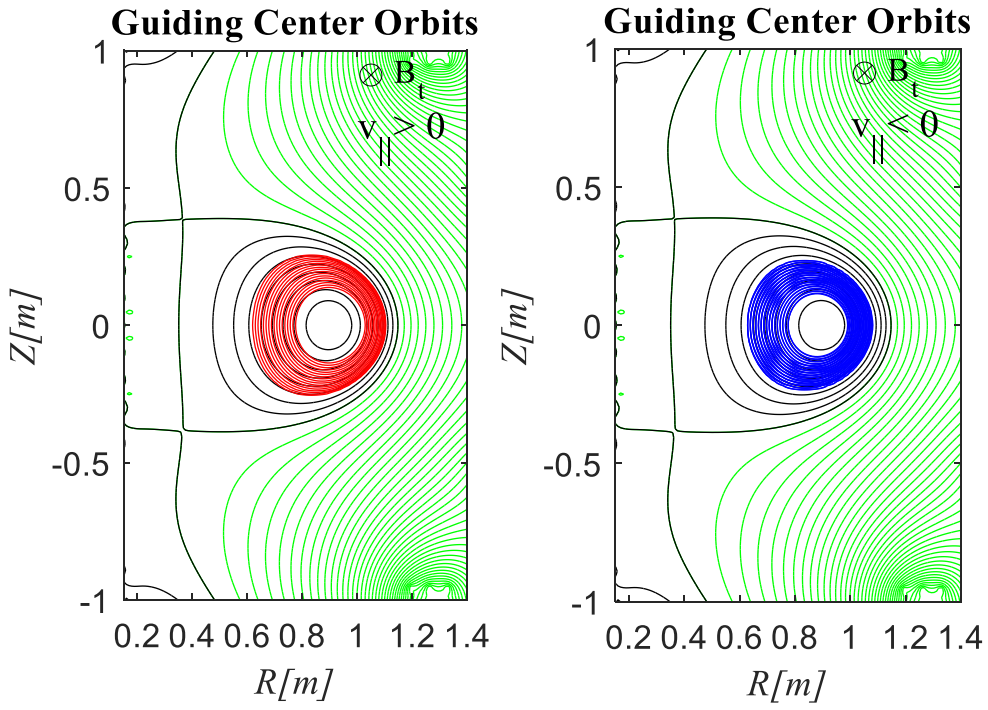

Figure 4.9: The red and blue contours indicate the guiding center orbits of the 2nd harmonic resonant passing electrons between the R positions from 0.60 m to 0.77 m and $Z = 0.00\,\text{m}$. The black and green contours show the closed and open magnetic surfaces, respectively. The left and right figure show the orbits of the electrons with initial positive and negative $v_{||}$, respectively.

In 2nd harmonic ECR, some resonant electrons with relatively low energies were trapped by the mirror forces and maintained banana orbits in the low filed side. The red and blue contours in the figure 4.10 show the banana orbits of the trapped electrons. The left figure shows the orbits of the trapped electrons with initial positive $v_{\|}$ and the right figure shows the orbits of the trapped electrons with initial negative $v_{\|}$.

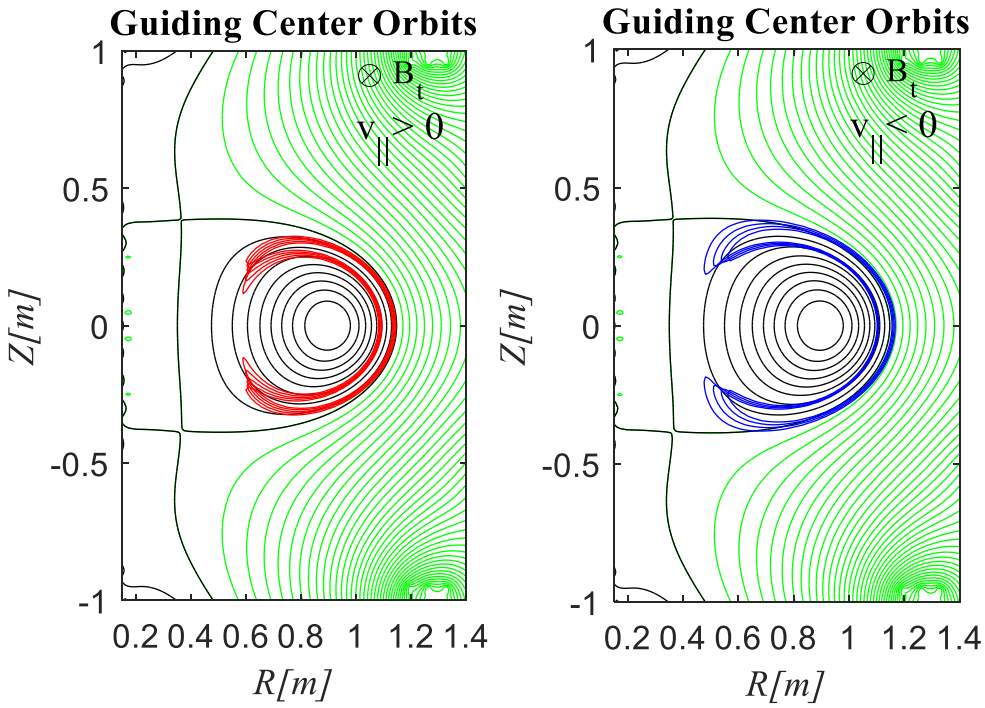

Figure 4.10: The red and blue contours indicate the banana orbits of the 2nd harmonic resonant trapped electrons. The black and green contours show the opened and closed magnetic surfaces, respectively. The left figure shows the banana orbits of the trapped electrons with initial positive $v_{\|}$ and the right figure shows the banana orbits of the trapped electrons with initial negative $v_{\|}$.

4.3 Relativistic Electron Cyclotron Resonance

4.3.1 Wave-electron Resonance

The *n*-th harmonic Doppler-shifted relativistic electron cyclotron resonance (ECR) condition is expressed as,

$$\gamma\left[1-N_{\|}\left(\frac{v_{\|}}{c}\right)\right]=\frac{nf_{ce}}{f} \tag{4.7}$$

Here, γ is the relativistic factor which is expressed as $\gamma=(1+\bar{P}_{\perp}^{2}+\bar{P}_{\|}^{2})^{1/2}$, where $\bar{P}_{\perp}=m_0\gamma v_{\perp}/m_0c$ and $\bar{P}_{\|}=m_0\gamma v_{\|}/m_0c$ are the normalized electron momentums in perpendicular and parallel to the magnetic field, respectively, $v_{\perp}$ and $v_{\|}$ are the perpendicular and parallel velocities of electron, $N_{\|}$ is the parallel refractive index, f is the frequency of the ECH waves, f_{ce} is the electron cyclotron frequency, m_0 is the rest mass of the electron and c is the speed of the light. The resonant ellipse momentum parameters are obtained from the equation (4.7) in $\bar{P}_{\perp}$ and $\bar{P}_{\|}$ momentum space. The resonant momentum range can be characterized by the minimum and the maximum normalized parallel momentum, $\bar{P}_{\|}^{\min}$ and $\bar{P}_{\|}^{\max}$ at $\bar{P}_{\perp}=0$, and the maximum normalized perpendicular momentum $\bar{P}_{\perp}^{\max}$ of the resonant ellipses.

The resonant ellipse momentum parameters are obtained from the equation (4.7) which are expressed as,

$$\begin{aligned}
\bar{P}_{\|}^{\max} &= \left[\frac{nf_{ce}}{f}N_{\|}+\sqrt{n^2\frac{f_{ce}^2}{f^2}-\left(1-N_{\|}^2\right)}\right]/\left[1-N_{\|}^2\right] \\
\bar{P}_{\|}^{\min} &= \left[\frac{nf_{ce}}{f}N_{\|}-\sqrt{n^2\frac{f_{ce}^2}{f^2}-\left(1-N_{\|}^2\right)}\right]/\left[1-N_{\|}^2\right] \\
\bar{P}_{\perp}^{\max} &= \sqrt{\left(n\frac{f_{ce}}{f}\right)^2\cdot\frac{1}{\left(1-N_{\|}^2\right)}-1}
\end{aligned} \tag{4.8}$$

Figure 4.11 shows the resonant ellipses in the normalized parallel and perpendicular momentum space $(\bar{P}_{\|},\bar{P}_{\perp})$ at different points of the major radius, *R* for the 2nd harmonic relativistic ECR, where parallel refractive index is $N_{\|}=+0.5$. The momentums of the electrons that match with the pair of the parallel and perpendicular momentums obtained from the resonant ellipse are

absorbed energy from the waves [44]. This transfer of energy by absorption appears as kinetic energy to the electrons which increased the thermal motion in the plasma and hence plasma heating.

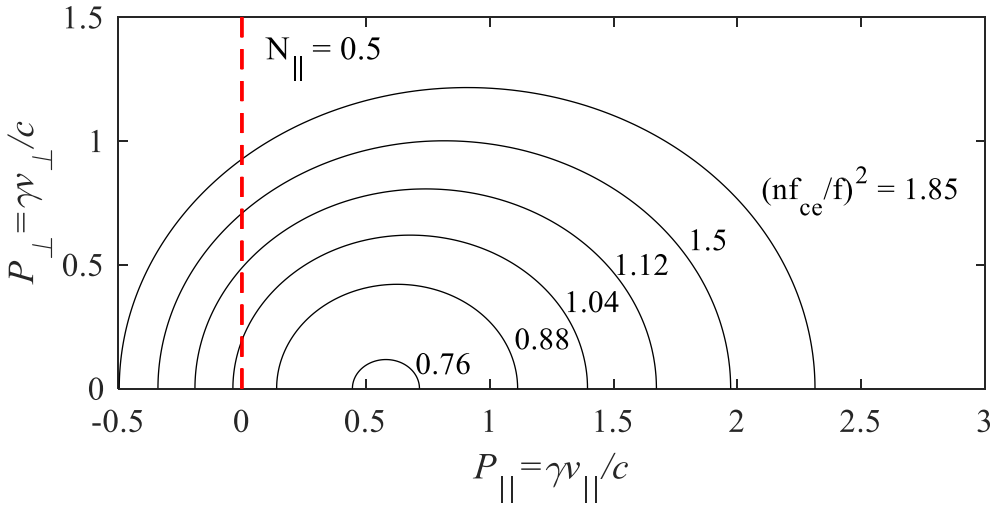

Figure 4.11: The resonant ellipses in the normalized parallel and perpendicular momentum space $(\bar{P}_{\|}, \bar{P}_{\perp})$ at different positions of the major radius, *R* for the 2nd harmonic relativistic ECR, where parallel refractive index is $N_{\|} = +0.5$.

However, If a transverse electric field of a wave is considered along it's propagation, it is observed that due to the variation of f_{ce} and $k_{\|}$ along the trajectory, the energy flux transported by the electric field (as obtained from the velocity space) are absorbed by the electrons whose initial energy are vary from point to point. The initial energy of the electrons steadily increases as the distance from the resonance layer increase. Thus, the waves' energy absorption spectrum is always asymmetric around the resonance layer $\left(f = nf_{ce}\right)$.

In case of oblique propagation, if the condition, $\left(nf_{ce}/f\right)^2 < \left(1 - N_{\|}^2\right)$ is satisfied, the waves' energy is not transferred to the plasma. For this condition the resonant ellipses become imaginary. This region usually located at the low field side of the resonance layer. On the high field side of this critical point, the waves' energy is transferred to the plasma. The real values of $\bar{P}_{\|}$ are obtained only for the condition, $\left(nf_{ce}/f\right)^2 - \left(1 - N_{\|}^2\right) \geq 0$. If the condition, $\left(nf_{ce}/f\right)^2 > 1$ is satisfied, the resonant ellipses take place both in the positive and negative range of the parallel velocities either for the positive and negative values of the parallel refractive index. This resonant

effect is known as “down-shift” Doppler effect. If the condition, $\left(1-N_{\|}^{2}\right)<\left(nf_{ce}/f\right)^{2}<1$ is satisfied, the resonant ellipses take place in the positive range of the parallel velocities for the positive values of the parallel refractive index as well as the resonant ellipses take place in the negative range of the parallel velocities for the negative values of the parallel refractive index in the velocity space. This resonant effect is known as “up-shift” Doppler effect. Figure 4.12 shows the resonant ellipses for the oblique propagation of the electromagnetic waves for the up-shifted absorption. Figure (a) and (b) are obtained for the condition, $\left(1-N_{\|}^{2}\right)<\left(nf_{ce}/f\right)^{2}<1$, where the resonance ellipses take place in the positive range of the parallel velocities for $N_{\|}>0$ and in the negative range of the parallel velocities for $N_{\|}<0$ in normalized parallel and perpendicular momentum space.

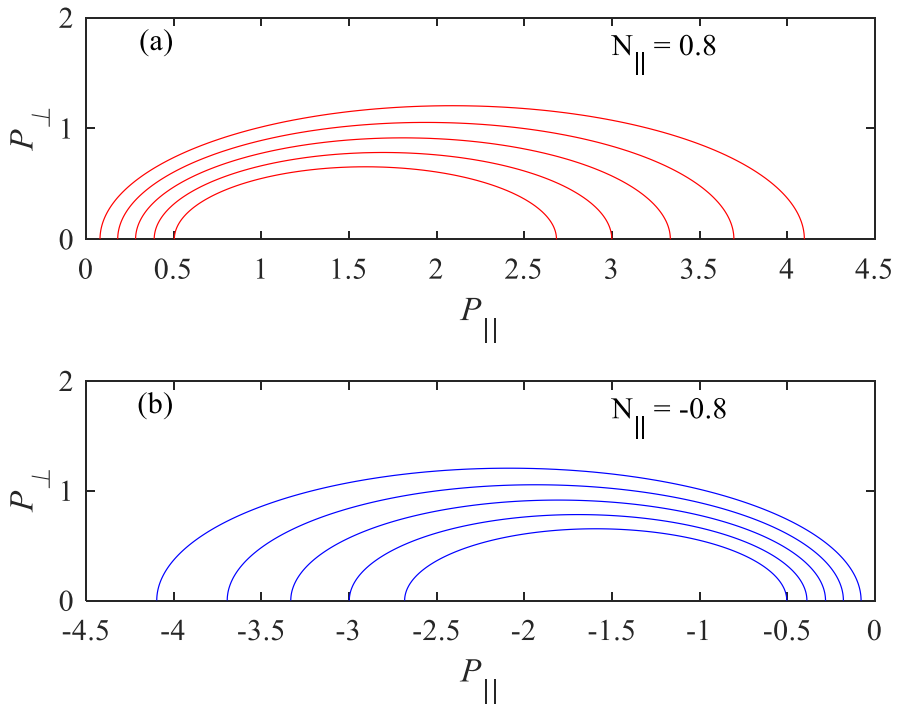

Figure 4.12: The resonant ellipses for the oblique propagation of the electromagnetic waves. Figure (a) and (b) are obtained for the condition, $\left(1-N_{\|}^{2}\right)<\left(nf_{ce}/f\right)^{2}<1$, where the resonance ellipses take place in the positive range of the parallel velocities for $N_{\|}>0$ and in the negative range of the parallel velocities for $N_{\|}<0$ in normalized parallel and perpendicular momentum $(\bar{P}_{\|},\bar{P}_{\perp})$ space.

Figure 4.13 shows the resonant ellipses for the oblique propagation of the electromagnetic waves for the down-shifted absorption. Figures (a) and (b) are obtained for the condition, $\left(nf_{ce}/f\right)^2 > 1$, where the resonance ellipses take place both in the positive and negative range of the parallel velocities either for $N_{\|} > 0$ or $N_{\|} < 0$. However, for the oblique propagation, the resonant ellipses are not symmetric in velocity space and this characteristic is the basis of the electron cyclotron current drive mechanism.

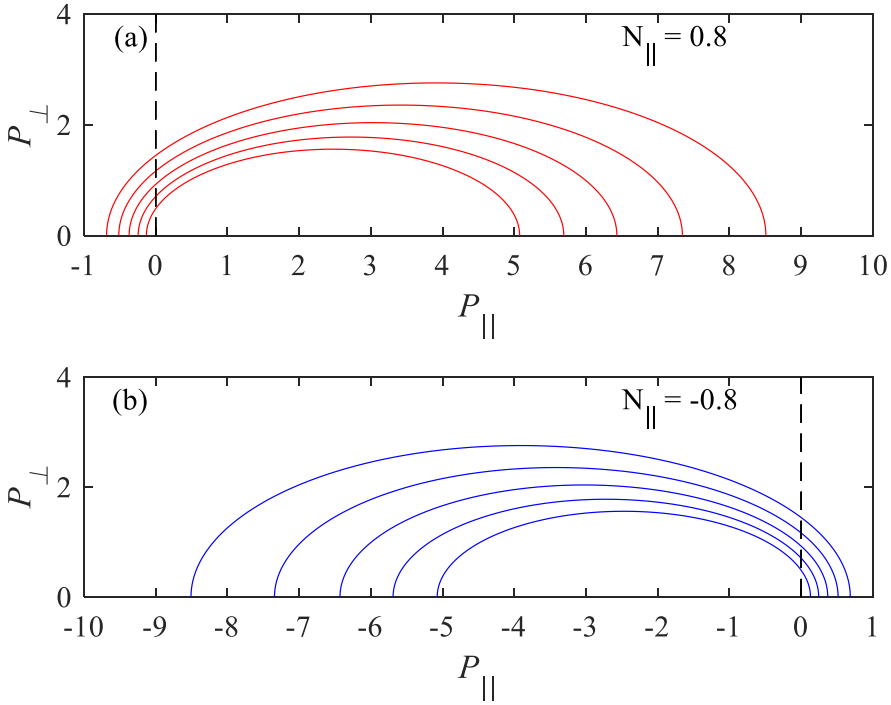

Figure 4.13: The resonant ellipses for the oblique propagation of the electromagnetic waves for the down-shifted absorption. Figure (c) and (d) obtained for the condition, $\left(nf_{ce}/f\right)^2 > 1$, where the resonance ellipses take place both in the positive and the negative range of the parallel velocities either for $N_{\|} > 0$ or $N_{\|} < 0$.

The resonant energy of the electron can be also explained from the resonant ellipses obtained from the relativistic ECR in the normalized perpendicular and parallel momentum ($\bar{P}_{\perp}, \bar{P}_{\|}$) space. Figure 4.14 shows the resonant ellipse for the 8.2 GHz 2nd harmonic ECR at $R = 0.63\,\mathrm{m}$ for $N_{\|} = 0.6$. The required minimum, maximum energy for the electron to be resonant are also shown in the figure. The minimum energy $E_{\min}$ for $\bar{P}_{\|}^{\min}$ at $\bar{P}_{\perp} = 0$ is 3 keV. The energy at $\bar{P}_{\perp}^{\max}$

is also illustrated in the figure. The energy E_{top} at $\bar{P}_{\perp}^{\max}$ is evaluated as 240 keV while the maximum energy $E_{\max}$ for $\bar{P}_{\parallel}^{\max}$ at $\bar{P}_{\perp} = 0$ is evaluated as 476 keV.

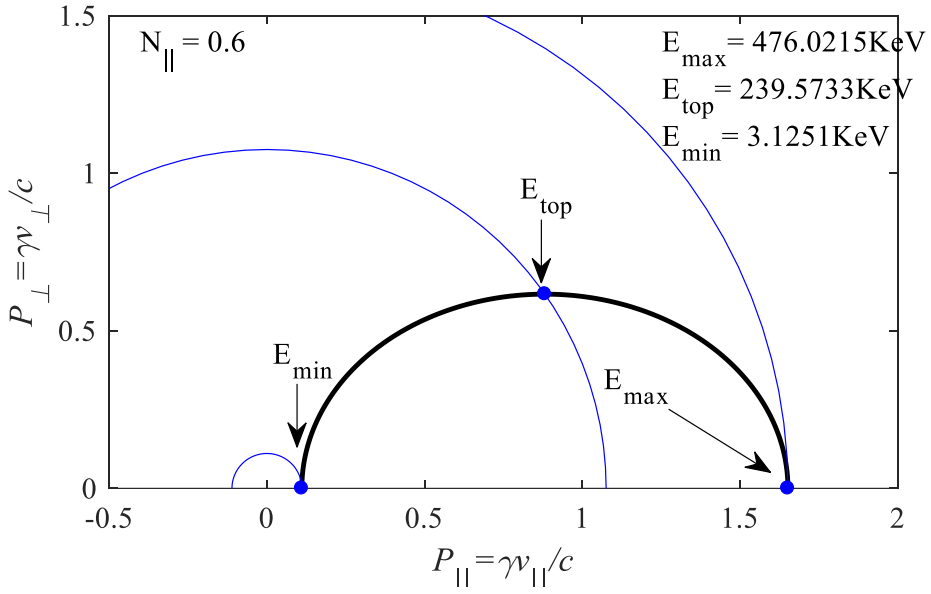

Figure 4.14: The resonant ellipse for the 8.2 GHz 2nd harmonic ECR at $R = 0.63$ m. The momentum contours for energy 3 keV , 240 keV and 476 keV are also shown in the figure. The minimum energy $E_{\min}$ for $\bar{P}_{\parallel}^{\min}$ at $\bar{P}_{\perp} = 0$ is 3 keV while the energy E_{top} for maximum normalized perpendicular momentum is evaluated as 240 keV.

The waves' energy absorption region as well as minimum initial energy of an electron required to be resonant are also explained from the resonant ellipses. The waves' energy absorption regions are increased as the value of the parallel refractive index $N_{\parallel}$ increased. Figure 4.15 and 4.16 show the waves' energy absorption regions and minimum initial energy required to be resonant for the fundamental and 2nd harmonic relativistic ECR, respectively where the absorption regions are evaluated for the parallel refractive index $N_{\parallel} = 0.50$ and $N_{\parallel} = 0.99$ and the maximum energy is restricted at 100 keV. From the figure, it has been observed that the waves' energy absorption region as well as minimum initial energy required to be resonant are increased as the value of the parallel refractive index increase. Compared with the fundamental ECR, the absorption region is larger for the 2nd harmonic ECR for the same parallel refractive index as shown in the two figures. Such phenomenon is also observed for the negative parallel refractive index.

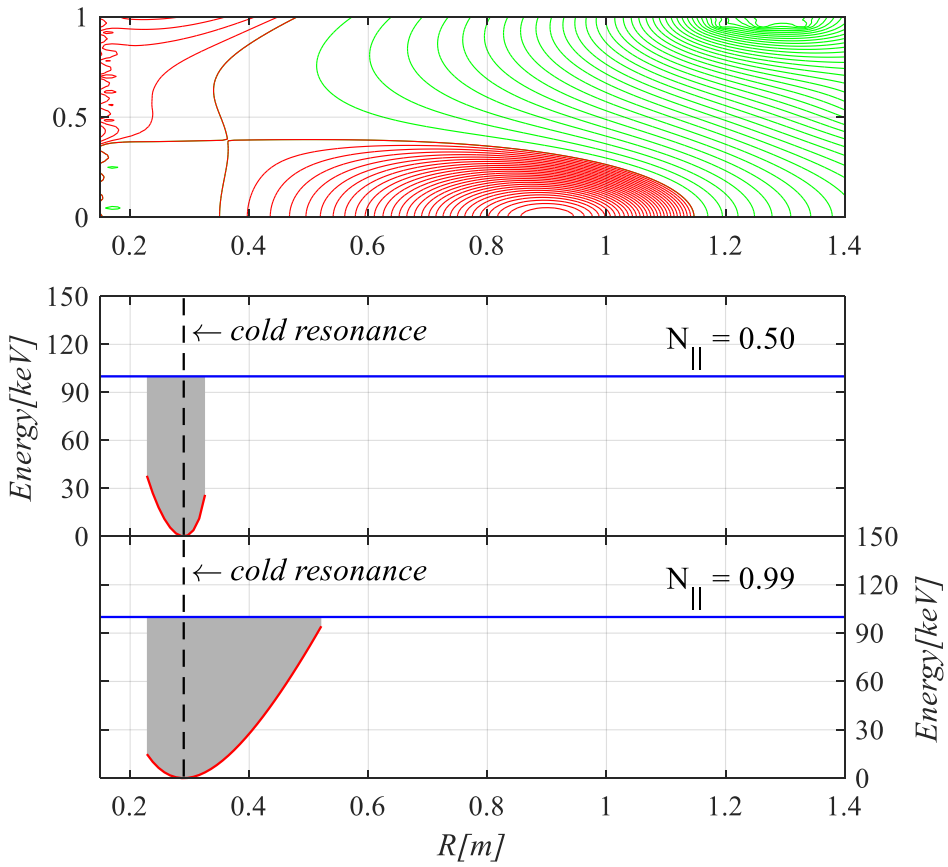

Figure 4.15: The waves' energy absorption regions and minimum initial energy required to be resonant for the relativistic fundamental ECR. The absorption regions are evaluated for the parallel refractive index $N_{||} = 0.50$ and $N_{||} = 0.99$ and the maximum energy is restricted at 100 keV. The waves' energy absorption region is increased as the value of the parallel refractive index $N_{||}$ increased. The top figure shows the upper part of the equilibrium closed and opened flux surfaces on the poloidal cross-section, cutting along the equatorial plane.

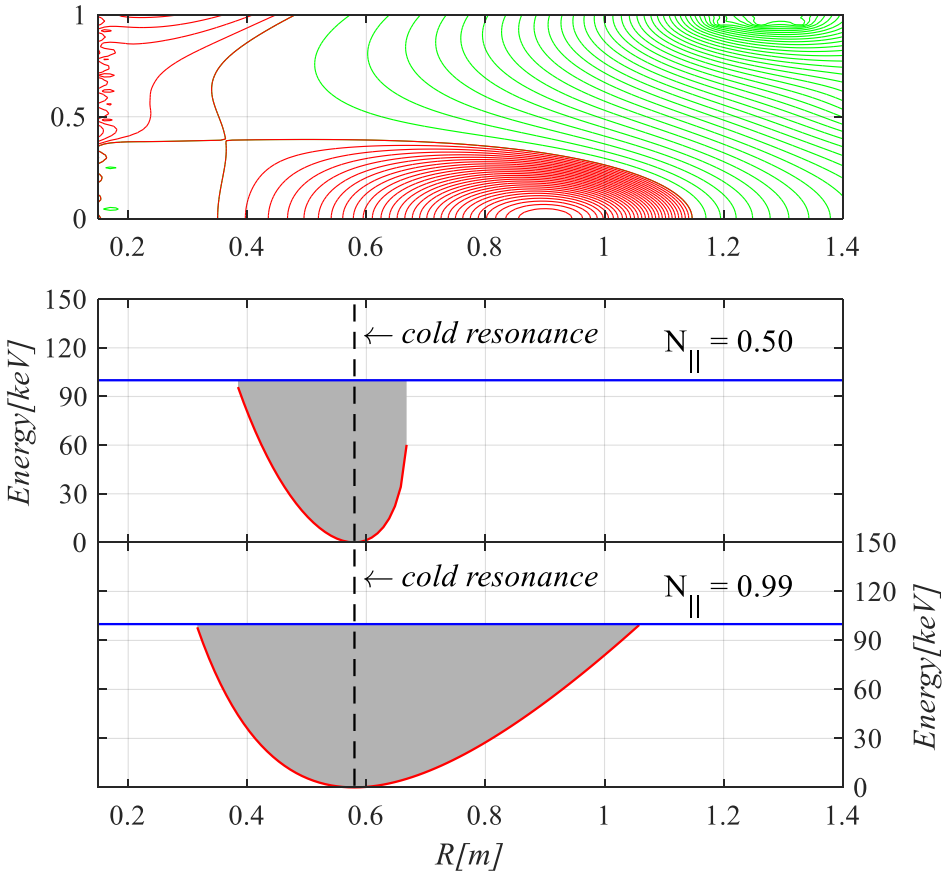

Figure 4.16: The waves' energy absorption regions and minimum initial energy required to be resonant for the relativistic 2nd harmonic ECR. The absorption regions are evaluated for the parallel refractive index $N_{\parallel} = 0.50$ and $N_{\parallel} = 0.99$ and the maximum energy is restricted at 100 keV. The top figure shows the upper part of the equilibrium closed and opened flux surfaces on the poloidal cross-section, cutting along the equatorial plane.

The pitch angles distribution of the resonant electrons can be also explained from the resonant ellipses. Figure 4.17 shows the pitch angles distribution for the different initial energies at the parallel and perpendicular velocity $(v_{\parallel}, v_{\perp})$ space for the 2nd harmonic ECR. The pitch angles distribution is evaluated for the up-shifted and the down-shifted ECR separately. From the evaluated figure, it has been interpreted that the pitch angles distribution are asymmetric in the positive and negative parallel velocities $(+v_{\parallel}, -v_{\parallel})$ direction. This asymmetric structure is stemmed from the relativistic mass effect. Figure 4.18 shows the pitch angles distribution of the energy range 1 keV to 100 keV for the different initial positions on the major radius R for the 2nd harmonic resonance condition, where $R = 0.58$ m is the location of cold resonance.

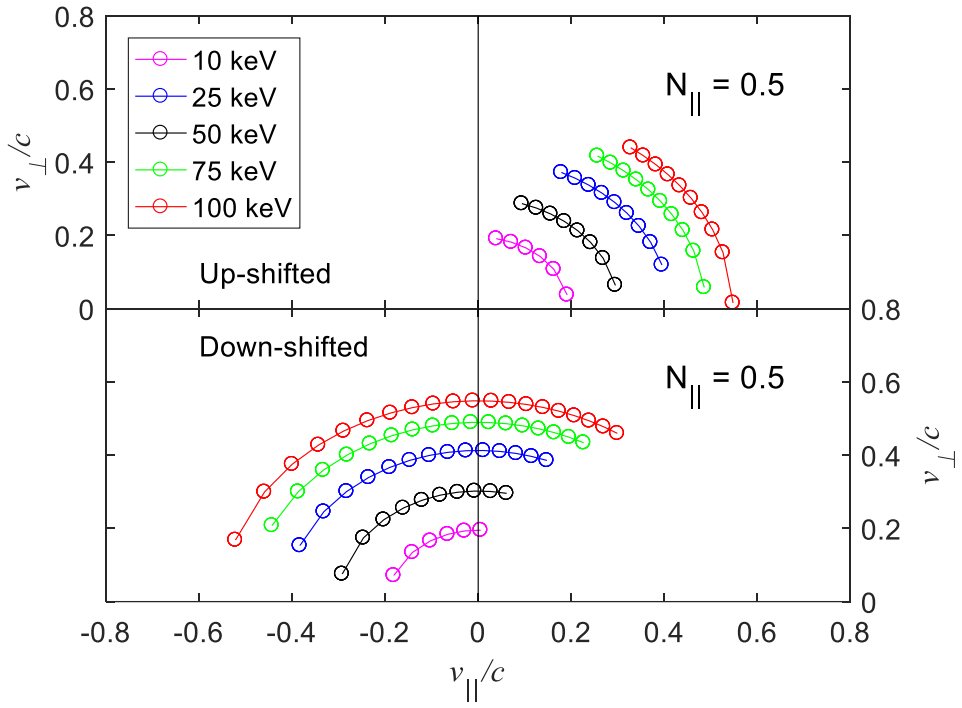

Figure 4.17: The pitch angles distribution for the different initial energies at the $(v_{\|}, v_{\perp})$ space for the 2nd harmonic ECR. The pitch angles distribution is evaluated for the up-shifted and down-shifted resonance separately. The pitch angles distribution are asymmetric in the positive and negative parallel velocities $(+v_{\|}, -v_{\|})$ direction.

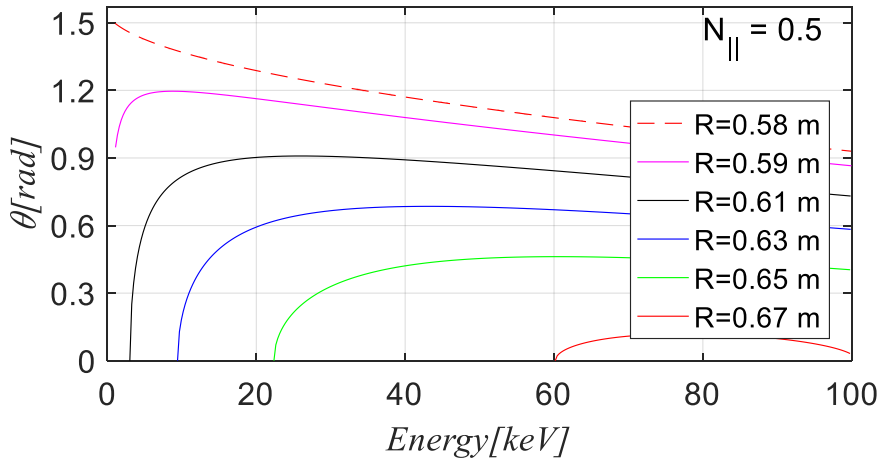

Figure 4.18: The pitch angles distribution of the energy range 1 keV to 100 keV for the different initial position on R for the 2nd harmonic resonance condition. $R = 0.58$ m is the location of cold resonance.

4.3.2 Equations of the Guiding Center Orbit

The guiding center orbits of the electrons were calculated by the guiding center equations of motion where the energy E, magnetic moment μ and toroidal angular momentum p_φ were conserved. The energy was expressed in terms of the relativistic factor, γ and $\gamma = (1+\bar{P}_\perp^2 + \bar{P}_\parallel^2)^{1/2}$ was expressed in terms of the magnetic moment and the toroidal angular momentum, where $\bar{P}_\perp = m_0\gamma v_\perp / m_0 c$ and $\bar{P}_\parallel = m_0\gamma v_\parallel / m_0 c$ were the normalized momentums in perpendicular and parallel to the magnetic field. The equations of the guiding center orbits were expressed as follows,

$$E = (\gamma - 1) m_0 c^2 \tag{4.9}$$

$$\mu = \frac{m_0 c^2 \bar{P}_\perp^2}{2B} \tag{4.10}$$

$$p_\varphi = \gamma m_0 R v_\parallel \left(\frac{B_t}{B}\right) - q\psi \tag{4.11}$$

$$\gamma = \left[1 + \frac{2\mu B}{m_0 c^2} + \left(\frac{(p_\varphi + q\psi)}{m_0 c R}\left(\frac{B}{B_t}\right)\right)^2\right]^{1/2} \tag{4.12}$$

where m_0 and q are the rest mass and elementary charge of an electron, c is the velocity of the light in free space, B and B_t are the total and toroidal magnetic field strengths, respectively, R is initial position of the electron in real space and ψ is the flux function. By substituting the value of γ from equation (4.12) into equation (4.9) the following equation was obtained,

$$E = \left(\left[1 + \frac{2\mu B}{m_0 c^2} + \left(\frac{(p_\varphi + q\psi)}{m_0 c R}\left(\frac{B}{B_t}\right)\right)^2\right]^{1/2} - 1\right) m_0 c^2 \tag{4.13}$$

The energy E in the equation (4.13) was expressed in terms of the magnetic moment and toroidal angular momentum. The contour line of this energy for a specific initial position on the (R, Z) plane under equilibrium magnetic configuration was expressed the orbit trajectory of the electron. Here, the perpendicular momentum specified in the equation (4.10) and the parallel velocity $v_\parallel$ specified in the equation (4.11) were obtained from the resonant ellipse for a specific initial position as the pair of the parallel and the perpendicular momentums $(\bar{P}_\perp, \bar{P}_\parallel)$. The values of the ψ, B and B_t were obtained from the EFIT plasma equilibrium solution.

4.3.3 Fundamental Resonant Electrons

Like non-relativistic fundamental resonant electrons, the guiding center orbits were calculated from the inboard limiter $R = 0.22$ m to $R = 1.15$ m horizontally and from $Z = 0.00$ m to $Z = \pm 0.40$ m vertically. In this resonance, the waves' energy was absorbed between the regions of $R = 0.22$ m to $R = 0.52$ m of the major radius for $N_{\parallel} = 0.99$ as shown in the figure 4.15. The plasma inboard separatrix was located at $R = 0.35$ m of the equilibrium magnetic configuration as shown in figure 3.9. Therefore, the resonant electrons from the inboard limiter $R = 0.22$ m to the inboard separatrix $R = 0.35$ m were lost and had no contribution on current. Only the electrons with initial positions between the regions $R = 0.35$ m to $R = 0.52$ m were confined and maintained steady-state orbits. The waves' energy was absorbed only at the outboard side of the cold resonance layer and only up-shifted Doppler effect resonance was occurred. The resonant ellipses were took place in the positive and negative range of the parallel velocities for $N_{\parallel} > 0$ and $N_{\parallel} < 0$, respectively. As a result, the resonant electrons were travelled both in the parallel and the antiparallel directions to the magnetic. The red and blue contours in the figure 4.19 show the calculated orbits between the R positions from 0.35 m to 0.53 m and $Z = 0.00$ m. The number of the actually calculated orbits was much larger than the orbits shown in the figure. The left and right figures show the orbits of the electrons with initial $+v_{\parallel}$ and $-v_{\parallel}$, respectively.

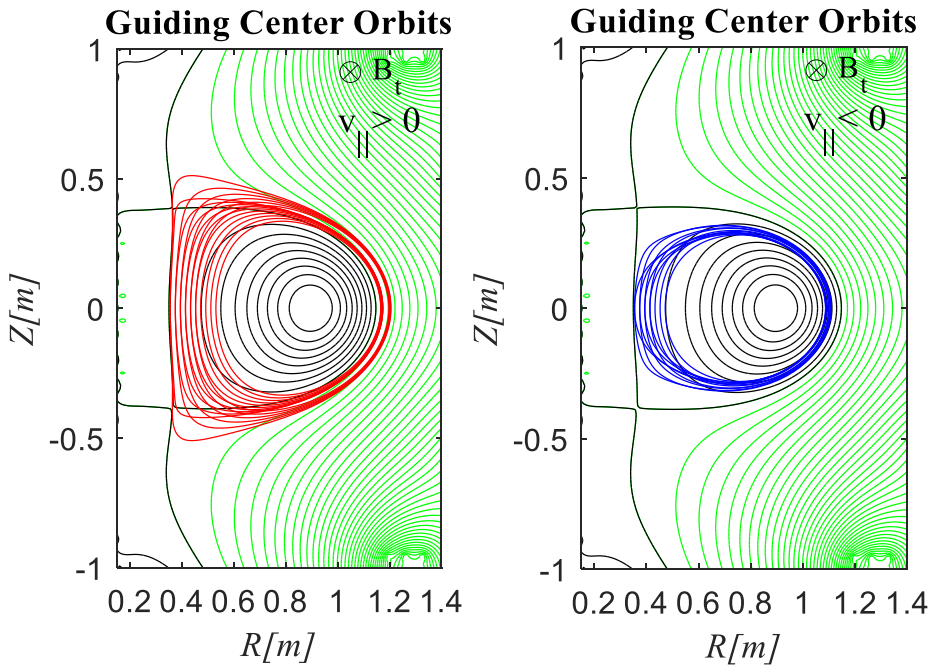

Figure 4.19: The red and blue contours show the orbits of the fundamental resonant electrons. The black and green contours show the closed and opened magnetic surfaces, respectively.

4.3.4 Second Harmonic Resonant Electrons

For the relativistic second harmonic resonant electrons, the guiding center orbits were also calculated from $R = 0.22$ m to $R = 1.15$ m horizontally and from $Z = 0.00$ m to $Z = \pm 0.40$ m vertically. In this resonance, the waves' energy was absorbed by the electrons between the regions of $R = 0.32$ m to $R = 1.05$ m of the major radius for $N_{||} = 0.99$ as shown in the figure 4.16. But the electrons with initial positions between the regions $R = 0.35$ m to $R = 1.05$ m were confined and maintained steady-state orbits. Here depending on resonance, the electrons were also travelled both in the parallel and the antiparallel directions to the magnetic field. The red and blue contours in the figure 4.20 show the guiding center orbits of the passing electrons between the R positions from 0.60 m to 0.73 m and $Z = 0.00$ m. The number of actually calculated orbits were much large than the orbits shown in the figure. The left figure shows the orbits of the electrons of initial positive $v_{||}$ and the right figure shows the orbits of the electrons of initial negative $v_{||}$.

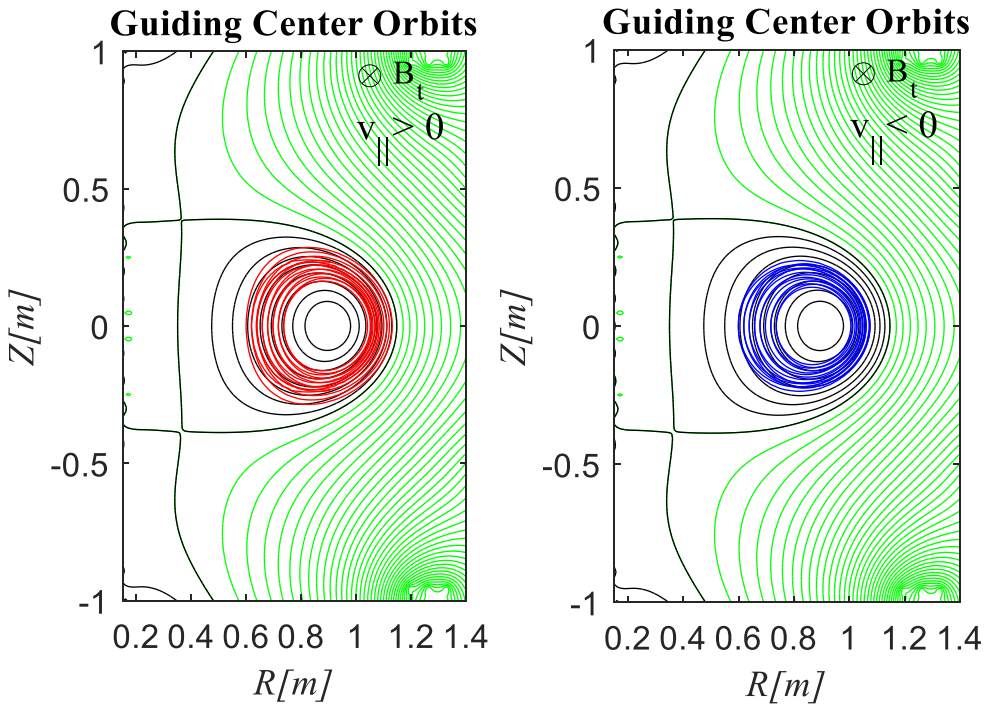

Figure 4.20: The red and blue contours indicate the guiding center orbits of the 2nd harmonic resonant passing electrons between the R positions from 0.60 m to 0.73 m and $Z = 0.00$ m, where the black and green contours show the closed and open magnetic surfaces, respectively. The left and right figure show the orbits of the electrons with initial positive and negative $v_{||}$, respectively.

In second harmonic ECR, some resonant electrons with relatively low energies were trapped by the mirror forces and maintained banana orbits in the low filed side. Figure 4.21 shows the banana orbits of the trapped electrons due to the magnetic mirror. The number of actually calculated orbits was much larger than the orbits shown in the figure. The left figure shows the banana orbits of the trapped electrons with initial positive $v_{||}$. The right figure shows the banana orbits of the trapped electrons with initial negative $v_{||}$.

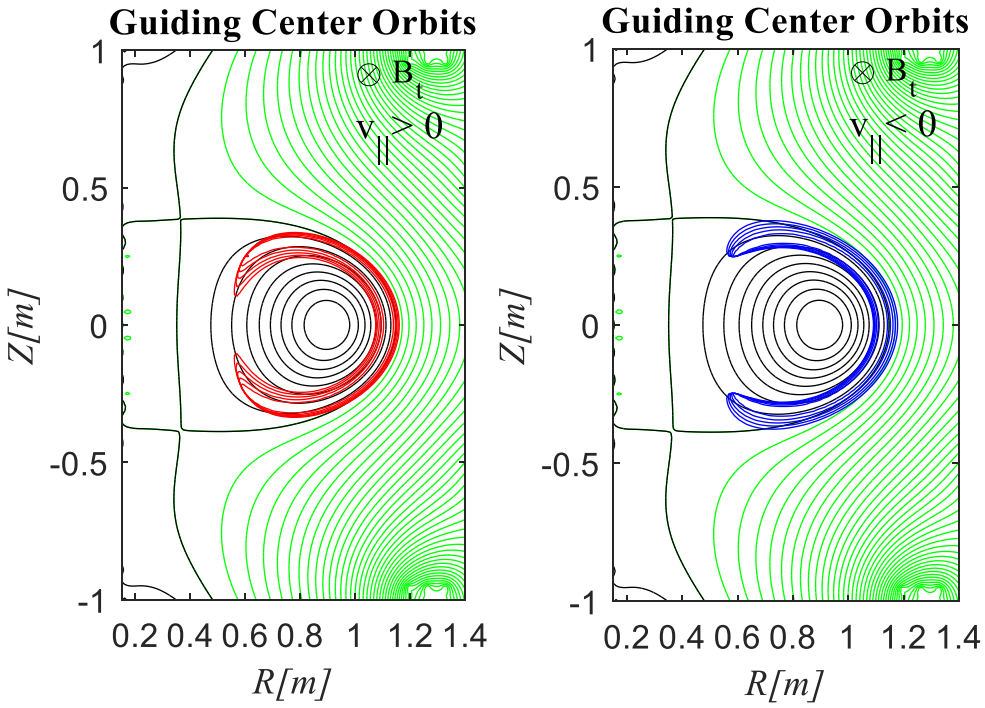

Figure 4.21: The red and blue contours indicate the banana orbits of the 2nd harmonic resonant trapped electrons. The black and green contours show the closed and opened magnetic surfaces. The left and right figure show the orbits of the electrons with initial positive and negative $v_{||}$, respectively.

For the 2nd harmonic relativistic ECR, the waves' energy absorption regions were located both the in high field and the low field sides of the cold resonance layer. In 2nd harmonic non-relativistic ECR, same phenomenon was observed. Therefore, the down-shifted and up-shifted Doppler effect resonances were occurred. In the down-shifted Doppler effect resonance, the resonant ellipses were took place both in the negative and positive range of parallel velocities in the

velocity space both for $N_{||} > 0$ and $N_{||} < 0$. Thus, relatively low energetic resonant electrons were travelled to the antiparallel direction of the magnetic field while relatively high energetic resonant electrons were travelled to the parallel direction of the magnetic field for $N_{||} > 0$. Since the maximum resonant energy of the electrons was settled 100 keV, a significant amount of relatively low energetic resonant electrons were travelled to the antiparallel direction of the magnetic field for $N_{||} > 0$. On the other hand, the resonant ellipses were also took place both in the negative and positive range of parallel velocities in the velocity space for $N_{||} < 0$. As a result, relatively low energetic resonant electrons were travelled to the parallel direction of the magnetic field, while relatively high energetic resonant electrons were travelled to the antiparallel direction of the magnetic field for $N_{||} < 0$. However since the uniform distribution of the parallel refractive index from negative range to positive range was considered in this calculation, the down-shifted Doppler effect had no significant impact in this calculations. Figure 4.22 shows the resonant ellipses for $N_{||} = -0.6$ and $N_{||} = +0.6$ with resonant energies contours. The figure shows that the resonant energy lays in the negative range of the of parallel velocities for $N_{||} = +0.6$ is equivalent to the resonant energy lays in the positive range of the of parallel velocities for $N_{||} = -0.6$.

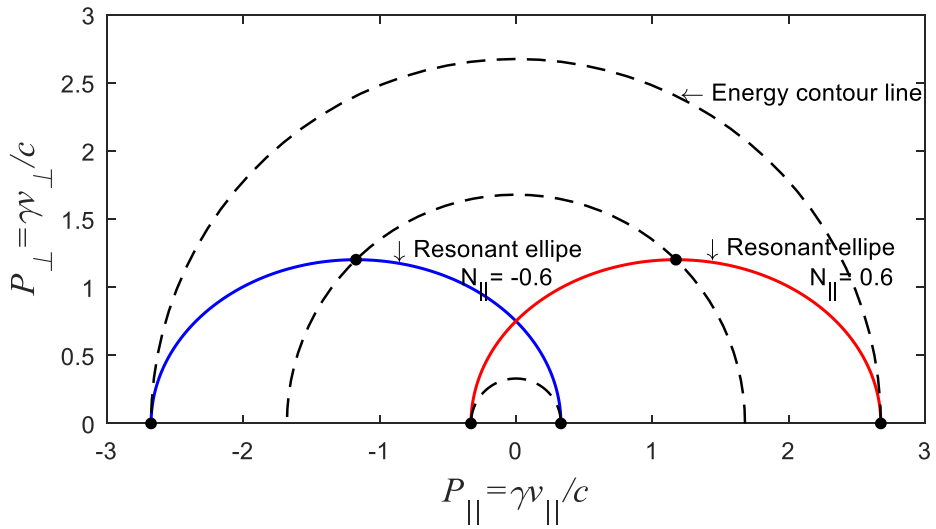

Figure 4.22: The resonant ellipses for $N_{||} = -0.6$ and $N_{||} = +0.6$ with resonant energies contours. The figure shows that the resonant energy lays in the negative range of the of parallel velocities for $N_{||} = +0.6$ is equivalent to the resonant energy lays in the positive range of the of parallel velocities for $N_{||} = -0.6$.

Chapter 5

Evaluation of the Orbit Current Distribution

5.1 Introduction

Orbit current distributions were evaluated from the electrons' orbital distributions along with the drift toroidal velocities v_φ and the elementary charge of the electron. The electrons orbital distribution was calculated by the picture-in-cell method and stored in a cell matrix prepared on the poloidal cross-section. The drift toroidal velocities v_φ throughout the orbit for each resonant electron were obtained from the orbit trajectory. The evaluated orbit current distribution J was also stored in a cell matrix on the poloidal cross-section. The current distribution contour plots on the poloidal cross-section and the current distribution profiles of the equatorial plane current on R were obtained from the J matrix. The surface-averaged current distribution profiles of the closed flux surfaces were also obtained on the square root of the normalized poloidal flux index from the J matrix.

5.2 Electron Orbital Distribution and Drift Toroidal Velocity Calculation

The electron orbital distribution was evaluated from the calculated guiding center orbits of the resonant electrons. As discussed in the previous chapter that the orbits of the resonant passing and trapped electrons were obtained on the poloidal cross-section. So to calculate the electron orbital distribution, a mesh grid containing 129×129 gridlines was considered on the poloidal cross-section which is equivalent to the EFIT grid-size. These 129×129 gridlines was produced 128×128 cells matrix on the poloidal cross-section. An orbit contour line of a resonant electron was plotted on the mesh grid. The intersected points of the orbit and the gridline and the length of the orbit-segment-elements between two intersected points were determined from the coordinate of the orbit contour line. For the orbit-segment-element, the location or the number of the cell of the cells matrix was also determined in where the orbit segment was took place. For the every orbit-segment-element between the two intersected points, the corresponding cells of the cell

matrix as well as the segment length of an orbit were determined. Then every determined cell of the matrix was deposited a value according to the length of the segment-elements of the orbit. Here the segment-element length was normalized by the diagonal length of the cell. These processes were repeated for every calculated orbit. Finally, the total number or summation of all the deposited values in the cells of the matrix resulted as the orbital distribution of the resonant electrons. Figure 5.1 shows the illustrative diagram of the electron orbital distribution calculation process. In the figure, 11×11 gridlines was shown instead of 129×129 gridlines because 129×129 gridlines makes the figure incomprehensible. In the figure intersection between the gridlines and orbit is shown. From these intersected points the orbit-segment length and the cell location in where the orbit-segment was deployed were determined.

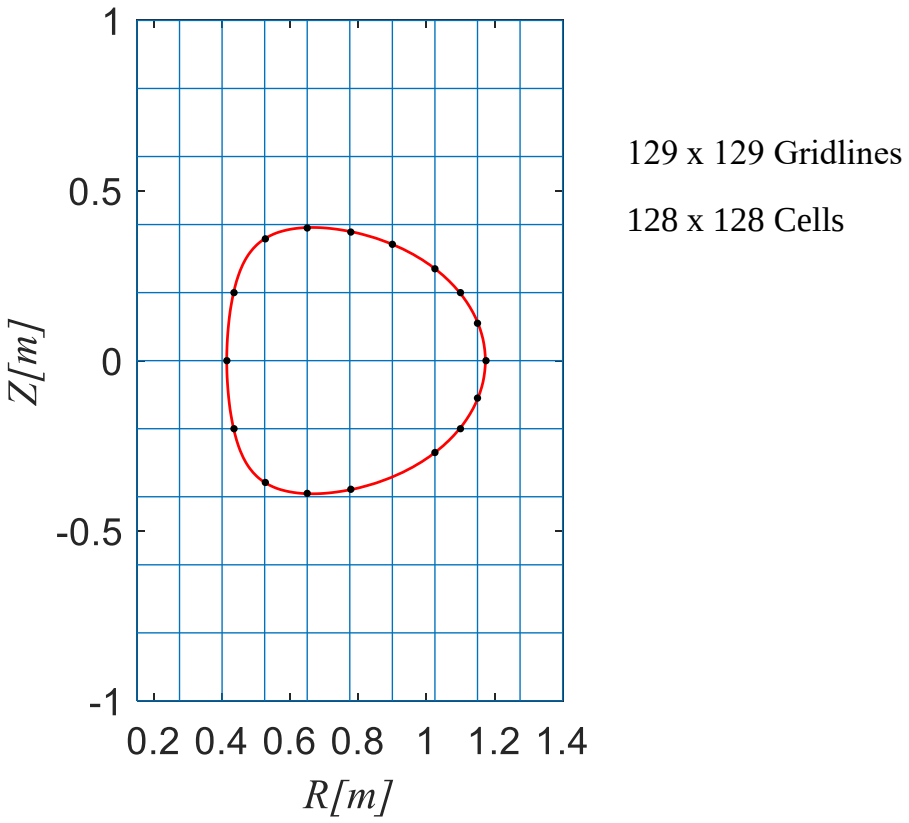

Figure 5.1: The illustrative diagram of the electron orbital distribution calculation process. In the figure, 11×11 gridlines is shown instead of 129×129 gridlines, because 129×129 gridlines make the figure incomprehensible. The red contour line represents the orbit and the black dotted indicates the intersection points between the orbit and gridlines. The orbit-segment-element length between two intersect points of orbit and gridlines and the corresponding cell location is determined.

The drift toroidal velocity was calculated during the orbit calculation. As discussed earlier that the guiding center orbits were calculated from the conservation of energy E, magnetic moment μ and toroidal angular momentum p_φ. This conservation demonstrates that the energy, magnetic moment and toroidal angular moment were constant throughout the orbit. Here, the constancy of p_φ implies that the orbit involves a change in ψ. This change in turn implies a displacement of the guiding center across the flux surfaces. Therefore, as the B field change slowly in time, the perpendicular $v_\perp$ and parallel $v_\parallel$ velocities of the electron also change slowly in time since the energy is conserved. This slowly varying parallel velocity also known as drift toroidal velocity v_φ was calculated throughout the orbit from the equation expressed as follows,

$$v_\varphi = v_\parallel \frac{B_t}{B} = \frac{\sqrt{2E}\cos\theta}{\sqrt{m}} \frac{B_t}{B} \tag{5.1}$$

where E and m are the total energy and mass of the electron, θ is the pitch angles of the guiding center throughout the orbit, B_t and B are toroidal and total magnetic field strengths throughout the orbit, respectively. The pitch angles θ of the guiding center throughout the orbit were obtained from the constancy of the constancy of p_φ.

5.3 Current Distribution Calculation

The current distribution J was evaluated from the electrons orbital distribution along with the electron drift toroidal velocities and the elementary charge of electron by the equation as,

$$J = env_\varphi \tag{5.2}$$

Here, e and v_φ are the elementary charge and drift toroidal velocity of the resonant electrons, respectively and n is the electron orbital distribution stored in the cell matrix. The calculated current distribution was also stored in a cell matrix on the poloidal cross-section. However, the current distributions were evaluated both for the electrons of initial positive $v_\parallel$ (travel in the parallel direction to the toroidal magnetic field) and initial negative $v_\parallel$ (travel in the antiparallel direction to the toroidal magnetic field) separately. In this study, the current distribution obtained for the resonant electrons with initial positive $v_\parallel$ was treated as the positive current. The positive current direction is opposite to the toroidal magnetic field direction i.e. co-current direction of the QUEST plasma current (I_p). The current distribution obtained for the resonant electrons with

initial negative $v_{\|}$ was treated as the negative current. The negative current direction is the same as the toroidal magnetic field direction i.e. counter-current direction of the QUEST plasma current (I_p).

To discuss the various phenomena of the obtained current distributions, the current distribution contour plots on the poloidal cross-section and the current distribution profiles of the equatorial plane current on R were plotted from the J matrix. The surface-averaged current distribution profiles of the closed flux surfaces were also plotted on the square root of the normalized poloidal flux index, s from the J matrix. The square root of the normalized poloidal flux index s was introduced by the equation as,

$$s = \sqrt{\frac{(|\psi - \psi_0|)}{(|\psi_a - \psi_0|)}} \tag{5.3}$$

where ψ_a and ψ_0 are the poloidal flux value at the plasma boundary and the plasma center, respectively [45].

5.4 Results and Discussion

The characteristics and features of the obtained current distribution contour plots, current distribution profiles and surface-averaged current distribution profiles were discussed in this section both for the non-relativistic ECR electrons and relativistic ECR resonant electrons separately.

5.4.1 Non-Relativistic Electrons

5.4.1.1 Fundamental Resonant Electrons

For the non-relativistic fundamental ECR, the resonant electrons were confined and maintained steady-state orbits from $R = 0.35$ m to $R = 0.75$ m of the major radius. Thus, the current distributions were obtained as small-scale width on the outer flux surfaces of the torus and become compact at the low field side of the torus. The figures 5.2 (a) and (b) show the positive and negative currents distributions contour plot on the poloidal cross-section. A significant

amount of positive current distribution appeared outside the last closed flux surface (LCFS) while the negative current distribution appeared inside the LCFS.

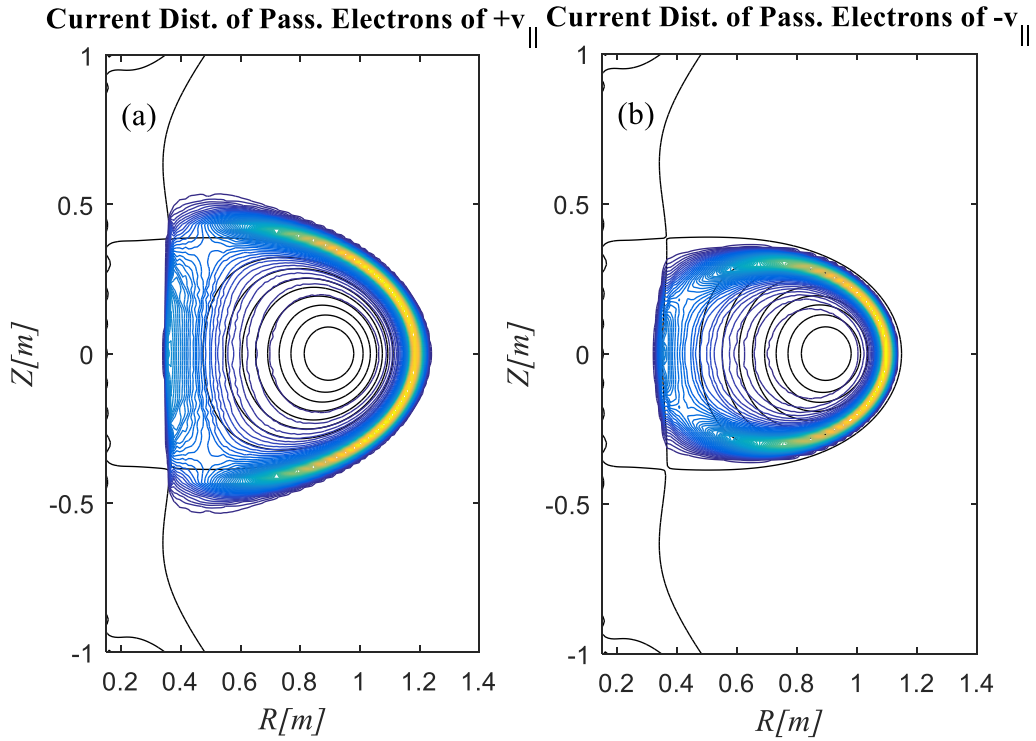

Figure 5.2: The current distribution contour plots on the poloidal cross-section of the fundamental non-relativistic resonant electrons. The black contours inside the figures show the closed flux surfaces. (a) Shows the positive current distribution evaluated for the resonant electrons with initial positive $v_{||}$, and (b) shows the negative current distribution evaluated for the electrons with initial negative $v_{||}$. The positive current distribution appeared outside the LCFS.

Figure 5.3 shows the currents distributions profiles along with the electron orbital distributions profiles of the equatorial plane on R for the fundamental non-relativistic resonant electrons. The figures (a) and (b) show the positive and negative currents distribution profiles along with the electron orbital distribution profiles of the electrons with initial positive $v_{||}$ and initial negative $v_{||}$, respectively. The top part of the figure shows the upper part of the closed and opened magnetic surfaces of the equilibrium magnetic configuration, cutting along the equatorial plane. Due to the drift of the guiding center, a significant amount of positive current distribution appeared outside the LCFS with peak value and all the negative current distribution appeared inside the LCFS. Though the drift directions of the guiding center with initial positive $v_{||}$ and negative $v_{||}$ were

same but due to travelling in the opposite direction, the positive current distribution was shifted outward direction along the LCFS and the negative current was shifted inward direction along the LCFS. As a result, no negative current distribution appeared outside the LCFS. Due to the larger drift toroidal velocities of the higher energetic electrons, both the positive and negative currents distributions were broadened compared with the electron orbital distributions as shown in the figure.

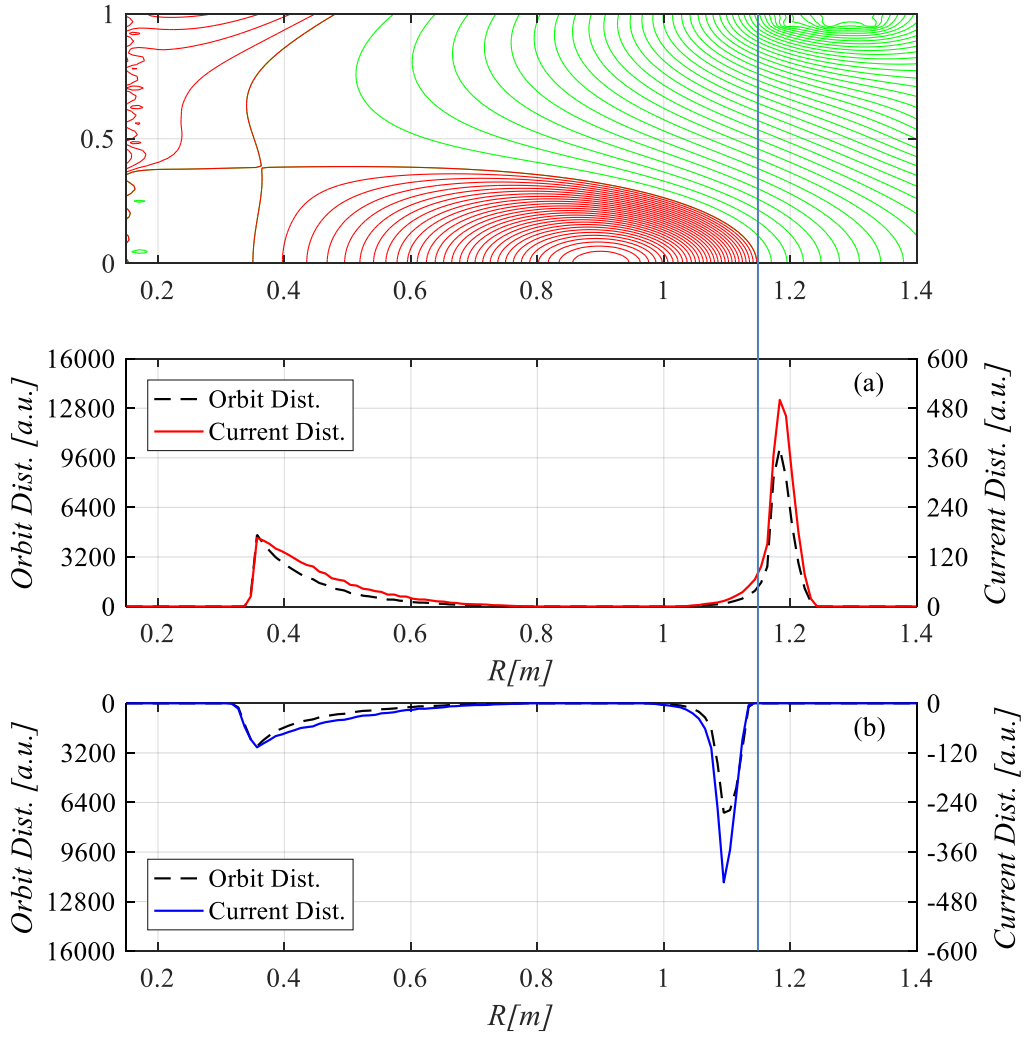

Figure 5.3: The currents and the electron orbital distributions profiles of the passing electrons of the equatorial plane on R for the fundamental non-relativistic resonant electrons. The top figure shows the upper part of the closed and opened magnetic surfaces of the equilibrium magnetic configuration, cutting along the equatorial plane. The figures (a) and (b) show the positive and the negative current distribution profiles along with electron orbital distribution profiles of the passing electrons with initial positive $v_{||}$ and initial negative $v_{||}$, respectively.

Figure 5.4 shows the surface-averaged positive and negative currents distribution profiles of the closed flux surfaces on the square root of the normalized poloidal flux index. Both the positive current distribution appeared only at the larger closed flux surfaces. A significant amount of the positive current distribution which didn't appear in the figure existed outside the LCFS. The entire negative current distribution appeared within the LCFS. The positive current distribution outside the LCFS should be dominant of the orbit current distribution.

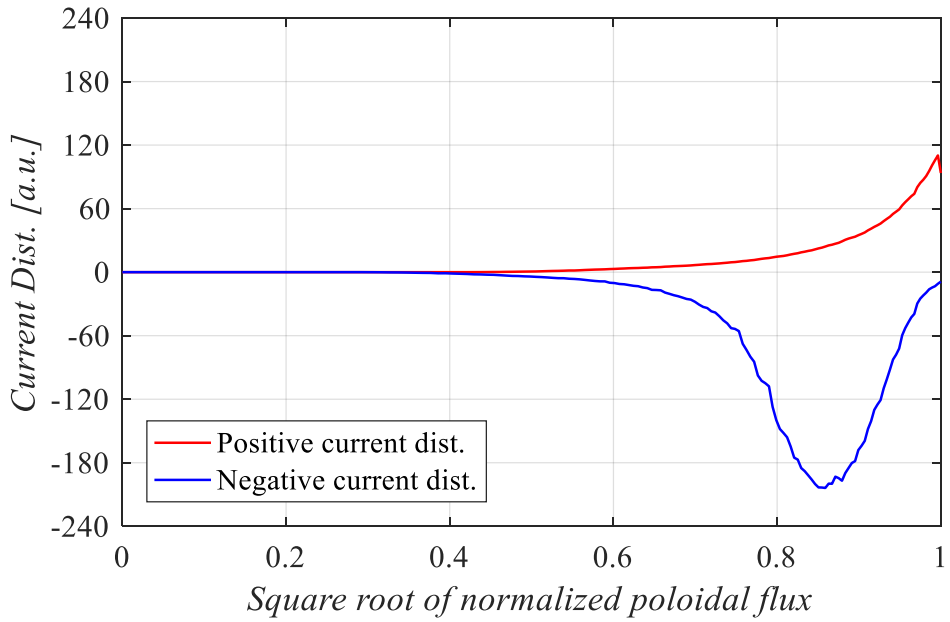

Figure 5.4: The surface-averaged current distribution profiles of the closed flux surfaces on the square root of the normalized poloidal flux index for the fundamental non-relativistic resonant electrons. (a) and (b) show the positive and the negative currents distribution profiles contributed of the electrons with initial positive $v_{||}$ and initial negative $v_{||}$, respectively.

5.4.1.2 Second Harmonic Resonant Electrons

In the 2nd harmonic ECR, both the down-shifted and the up-shifted Doppler effects resonance were occurred and the resonant electrons were confined and maintained steady-state orbits between $R = 0.36$ m to $R = 1.15$ m of the major radius. Since the waves' energy absorption region was larger compared with the fundamental ECR, a large number of electrons were maintained steady-state orbits and contributed currents. Figure 5.5 shows the current distribution contour plots on the poloidal cross-section for the 2nd harmonic non-relativistic passing resonant electrons.

Figure (a) and (b) show the positive and negative current distributions contour plots. A significant amount of the positive current distribution appeared outside the LCFS, while the negative current distribution was shown inside the LCFS.

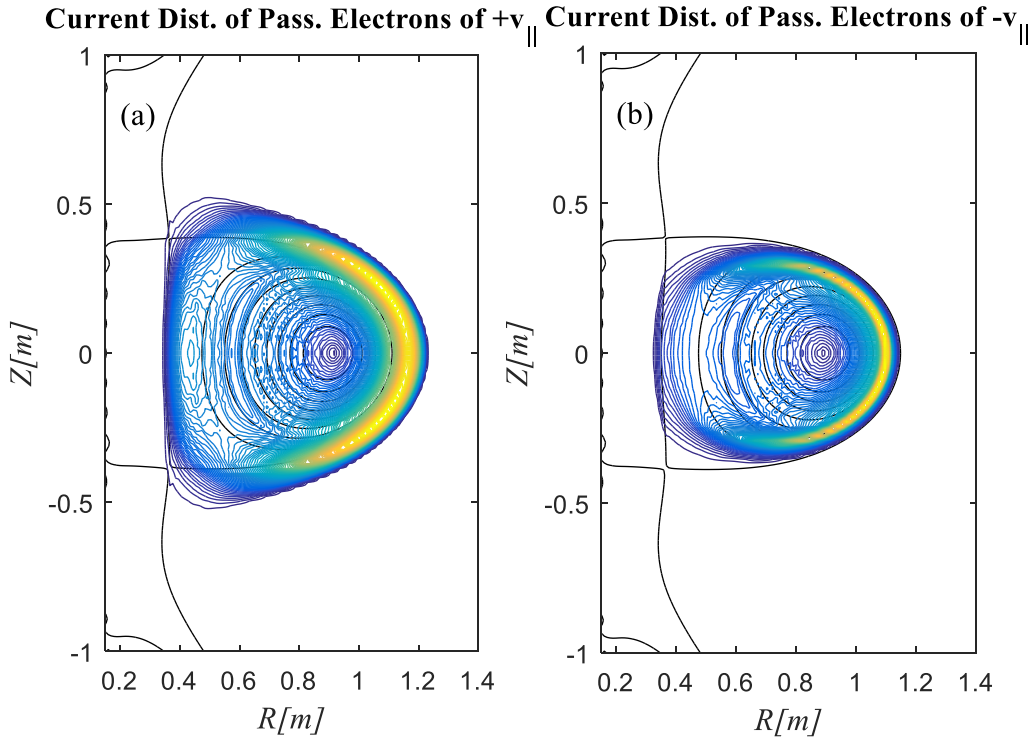

Figure 5.5: The current distribution contour plots on the poloidal cross-section for the 2nd harmonic non-relativistic passing resonant electrons. (a) Shows the positive current distribution contour plot contributed by the electrons with initial positive $v_{\|}$, and (b) shows the negative current distribution contour plot contributed by the electrons with initial negative $v_{\|}$. The black contours inside the figure indicate the closed flux surfaces.

Figure 5.6 shows the current distribution profiles along with the electron orbital distribution profiles of the passing electrons of the equatorial plane on R for the 2nd harmonic non-relativistic resonant electrons. Figure (a) shows the positive current distribution profile along with the electron orbital distribution profile of the passing electrons with initial positive $v_{\|}$. Figure (b) shows the negative current distribution profile along with the electron orbital distribution profile of the passing electrons with initial negative $v_{\|}$. In this resonance, also a significant amount of positive current distribution appeared outside the LCFS while the entire negative current distribution appeared inside the LCFS. Both the positive and negative currents distributions were

decreased at $R = 0.58\,\mathrm{m}$ due to cold resonance. The minimum initial energies of the resonant electrons were increased as the initial positions of the electrons were approached far from the cold resonance layer. As a result, for the higher energetic electrons with larger drift toroidal velocities, both the positive and the negative currents distributions profiles were broadened compared with the electron orbital distributions profiles.

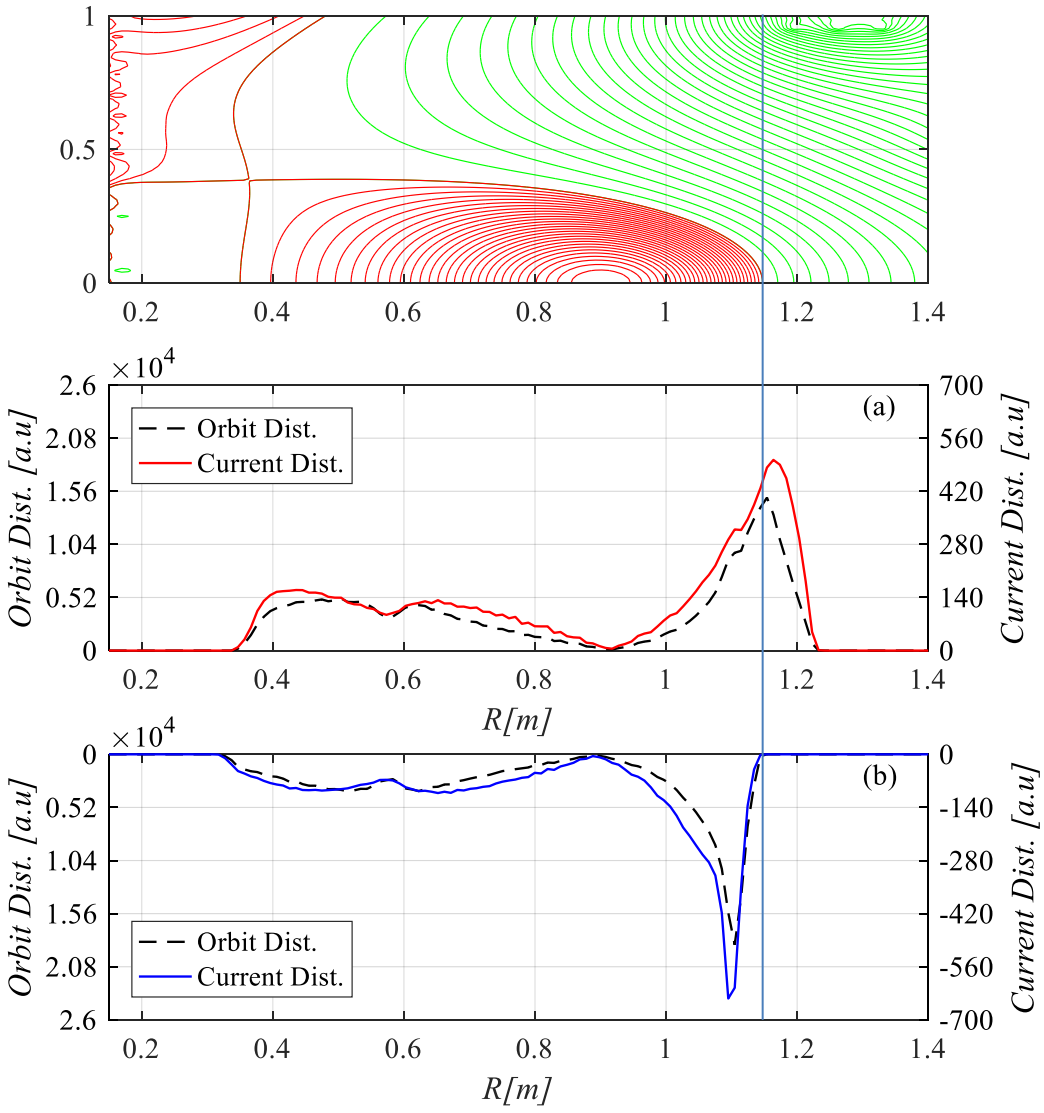

Figure 5.6: The currents distributions and electron orbital distributions profiles of the passing electrons of the equatorial plane on R for the 2nd harmonic non-relativistic resonant electrons. The top figure shows the upper part of the closed and opened magnetic surfaces of the equilibrium magnetic configuration, cutting along the equatorial plane. (a) Shows the positive current and orbital distributions profiles of electrons with initial positive $v_{\|}$, and (b) shows the negative current and orbital distributions profiles of the electrons with initial negative $v_{\|}$.

Figure 5.7 shows the current distribution profile of the equatorial plane on R contributed by the trapped electrons for the 2nd harmonic non-relativistic resonant electrons. As the trapped electrons travelled both in the parallel and antiparallel direction to the magnetic field, they contributed both the positive and negative currents. A significant amount of positive current distribution contributed by the trapped electrons appeared outside the LCFS while the entire negative current distribution appeared only inside the LCFS.

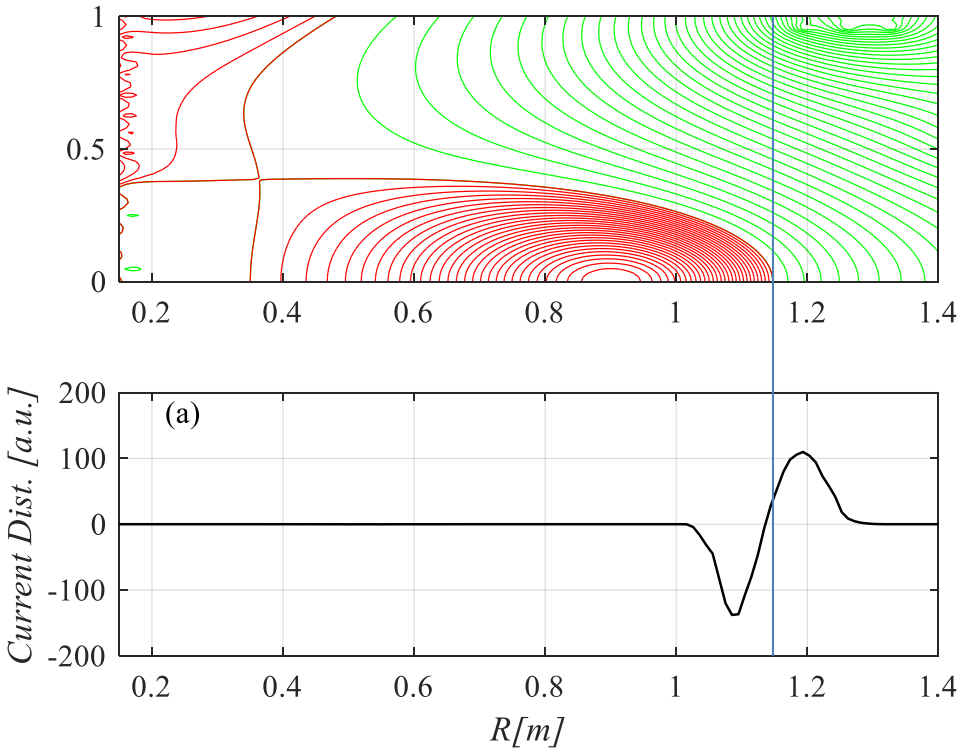

Figure 5.7: The both the positive and negative current distribution profile of the equatorial plane on R, contributed by the trapped electrons for the 2nd harmonic non-relativistic resonant electrons. The top figure shows the upper part of the closed and opened magnetic surfaces of the equilibrium magnetic configuration, cutting along the equatorial plane.

Figure 5.8 shows the surface-averaged positive and negative currents distributions profiles of the passing electrons and trapped electrons of the closed flux surfaces on the square root of the normalized poloidal flux index for 2nd harmonic non-relativistic resonant electrons. Both the positive and negative currents distributions stated to increase from the magnetic axis and the entire negative current distribution was accommodated inside the LCFS while the positive current

distribution appeared outside the LCFS. The positive current distribution of the trapped electrons also appeared outside the LCFS while the entire the entire negative current distribution of the trapped electrons appeared within the LCFS.

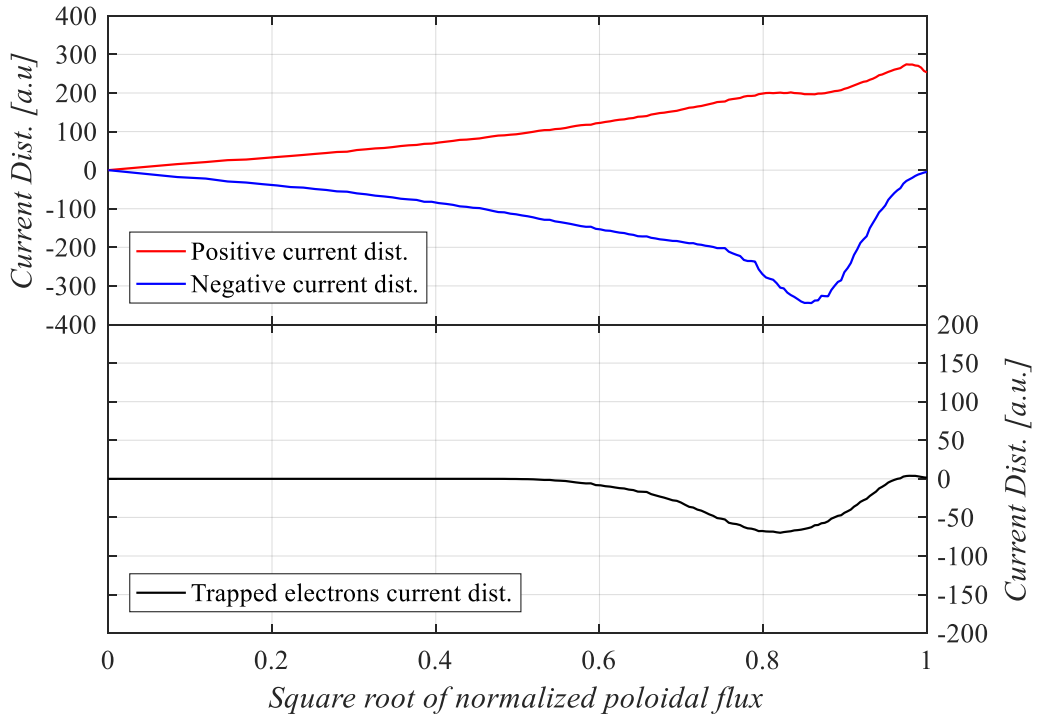

Figure 5.8: The surface-averaged current distribution profiles of the passing and the trapped electrons of closed flux surfaces on the square root of the normalized poloidal flux index for the 2nd harmonic non-relativistic resonant electrons.

5.4.2 Relativistic Electrons

For the relativistic resonant electrons, the current distribution contour plots, the current distribution profiles and the surface-averaged current distribution profiles were obtained both for the fundamental and second harmonic resonant electrons separately.

5.4.2.1 Fundamental Resonant Electrons

Since for the fundamental relativistic ECR, the resonant electrons were confined and maintained steady-state orbits between the region of $R = 0.35\,\mathrm{m}$ and $R = 0.52\,\mathrm{m}$ of the major radius, the

evaluated current distributions also appeared only at the outer flux surfaces of the torus. Figure 5.9 shows the current distribution contour plots on the poloidal cross-section for the fundamental relativistic resonant electrons. Figures (a) and (b) show the positive and negative currents distributions contour plot on the poloidal cross-section, respectively. A significant amount of positive current distribution was shown outside LCFS. Though a small amount of negative current distribution appeared outside of the LCFS at the inboard side of the plasma torus but most of the negative current distribution was shown inside the LCFS.

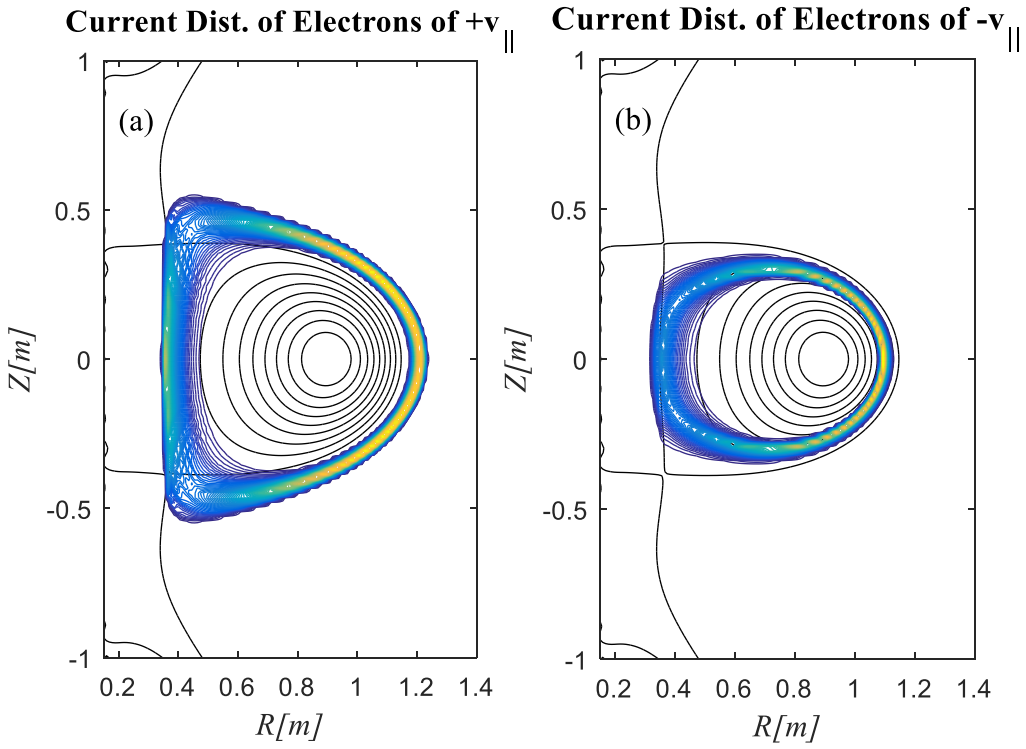

Figure 5.9: The current distributions contour plots on the poloidal cross-section of the fundamental relativistic resonant electrons. The black contours inside the figures represent the closed flux surfaces. (a) Shows the positive current distribution, and (b) shows the negative current distribution. A significant amount of positive current distribution appeared outside of the LCFS while most of the negative current distribution appeared inside the LCFS.

Figure 5.10 shows the currents distributions profiles along with the electron orbital distributions profiles of the equatorial plane on R for the fundamental relativistic resonant electrons. Figure (a) shows the positive current and orbit distributions profiles of the electrons with initial positive $v_{||}$ and (b) shows the negative current and orbit distributions profiles of the electrons with initial

negative $v_{\|}$, respectively. The top figure shows the upper part of the closed and opened magnetic surfaces of the equilibrium magnetic configuration, cutting along the equatorial plane. Due to the drift of the guiding center of the electrons, a significant amount of positive current distribution appeared outside the LCFS with peak value and all the negative current distribution appeared inside the LCFS. Though the drift directions of the guiding center with initial positive $v_{\|}$ and negative $v_{\|}$ were same but due to travelling in the opposite direction, the positive current distribution was shifted outward direction along the LCFS and the negative current was shifted inward direction along the LCFS. No negative current distribution appeared outside the LCFS.

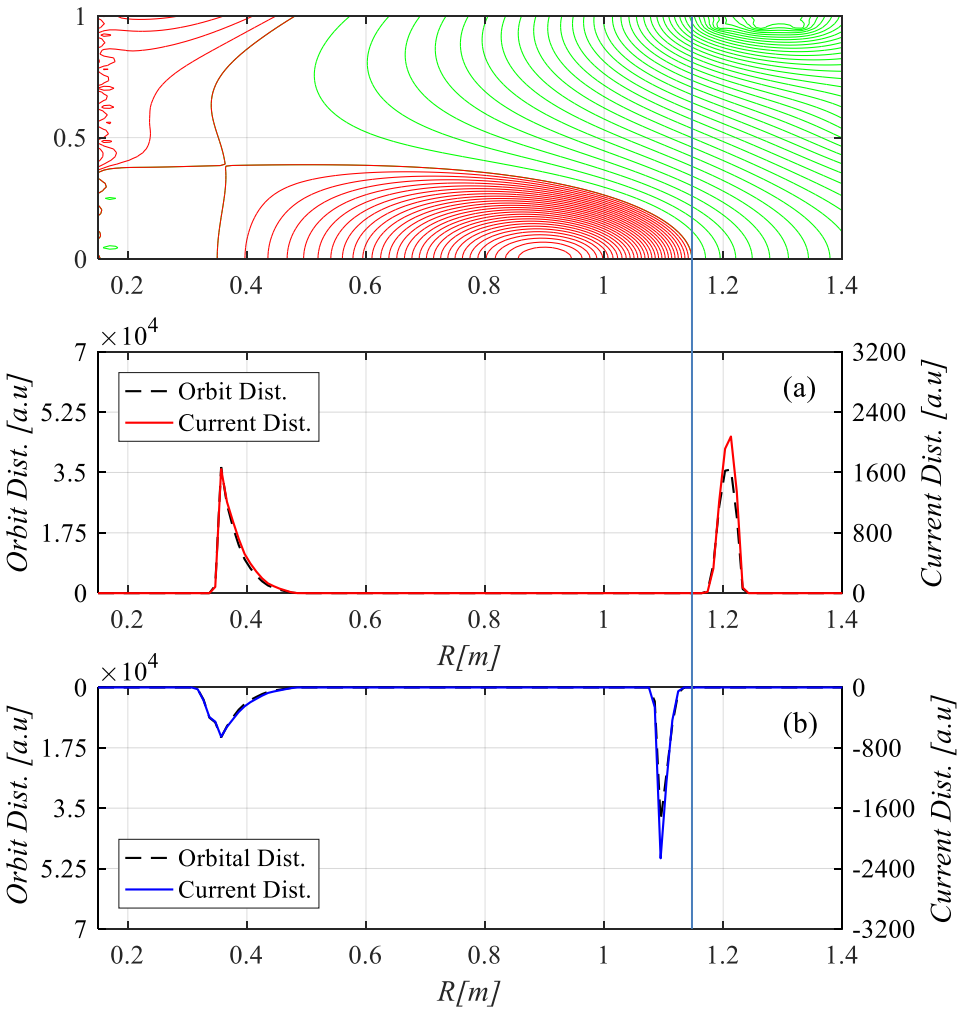

Figure 5.10: The currents distributions and the electron orbital distributions profiles of the equatorial plane on R for the passing fundamental relativistic resonant electrons. The top figure shows the upper part of the closed and opened magnetic surfaces of the equilibrium magnetic configuration, cutting along the equatorial plane. (a) and (b) show the positive and negative currents and electrons orbital distribution profiles, respectively.

Figure 5.11 shows the surface-averaged positive and negative currents distribution profiles of the closed flux surfaces on the square root of the normalized poloidal flux index. The positive current distribution appeared only near the LCFS. A significant amount of the positive current distribution not appeared in the figure existed outside the LCFS. The entire negative current distribution appeared within the LCFS. The positive current distribution outside the LCFS should be dominant of the orbit driven current distribution.

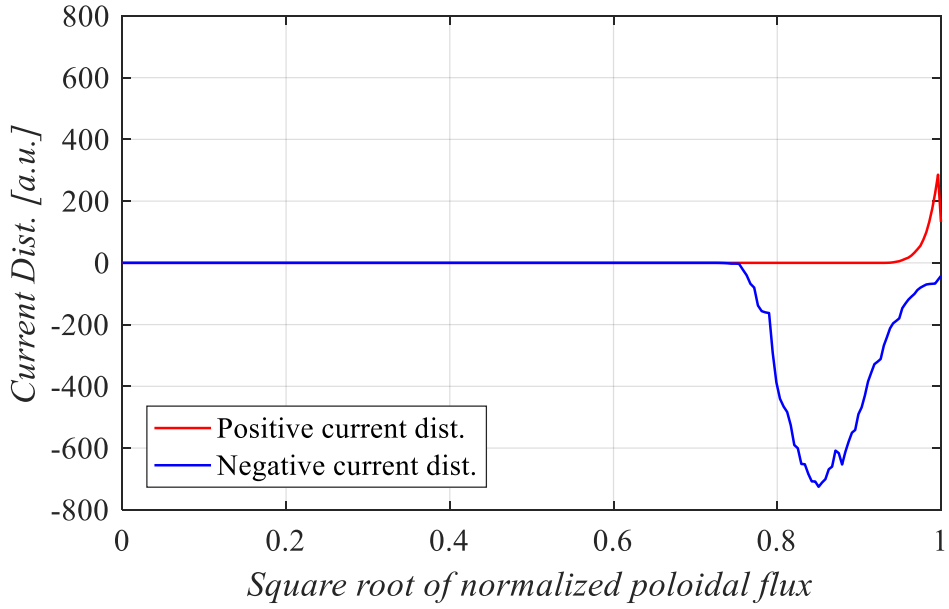

Figure 5.11: The surface-averaged current distribution profiles of the closed flux surfaces on the square root of the normalized poloidal flux index for the fundamental relativistic resonant electrons. The figures (a) and (b) show the positive and the negative current distribution profiles contributed by the electrons with initial positive $v_{\|}$ and initial negative $v_{\|}$, respectively.

5.4.2.2 Second Harmonic Resonant Electrons

In the 2nd harmonic relativistic ECR, both the down-shifted and the up-shifted resonance were occurred and the resonant electrons were confined and maintained steady-state orbits between $R = 0.35\,\text{m}$ to $R = 1.05\,\text{m}$ of the major radius. Since, the waves' energy absorption region was larger compared with the fundamental resonance condition, a large number of electrons were maintained steady-state orbits and contributed currents. Figure 5.12 shows the current distribution contour plots on the poloidal cross-section for the 2nd harmonic relativistic resonant electrons. Figure (a) and (b) show the positive and negative currents distributions contour plots. A significant amount of the positive current distribution was shown outside the LCFS, while the negative current distribution was shown only inside the LCFS.

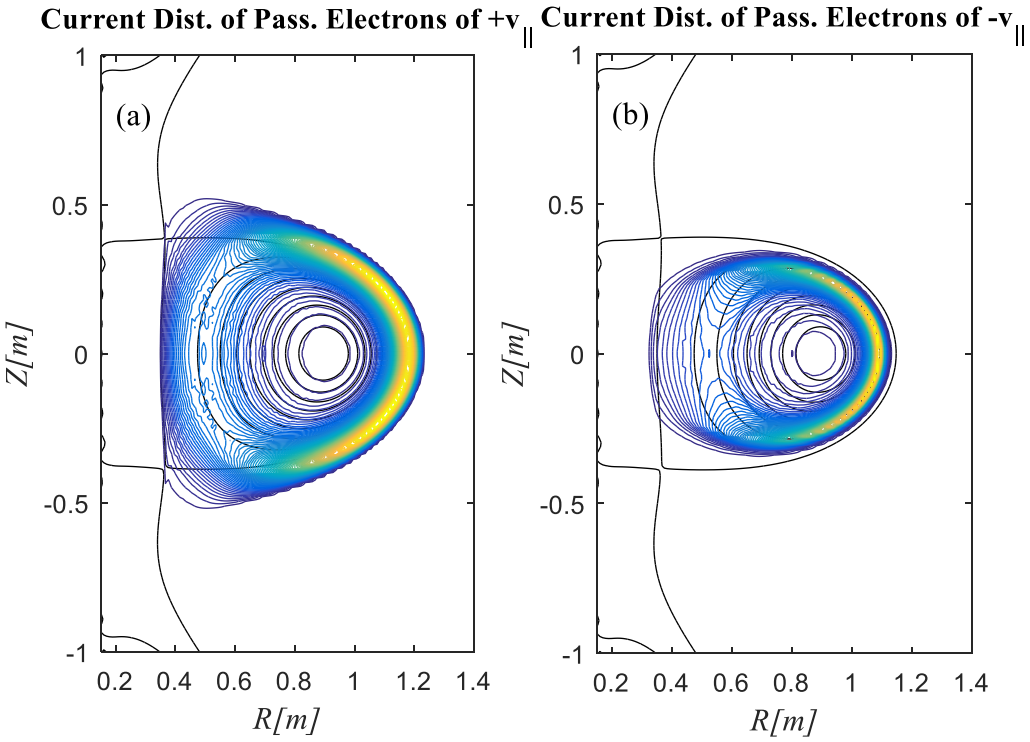

Figure 5.12: The current distribution contour plots on the poloidal cross-section for the 2nd harmonic relativistic resonant electrons. (a) Shows the positive current distribution contour plot contributed by the electrons with initial positive $v_{\|}$, and (b) shows the negative current distribution contour plot contributed by the electrons with initial negative $v_{\|}$. The black contours inside the figure indicate the closed flux surfaces.

Figure 5.13 shows the current distribution profiles along with the electron orbital distribution profiles of the passing electrons of the equatorial plane on R for the 2nd harmonic relativistic resonant electrons. Figure (a) shows the positive current distribution profile along with the electron orbital distribution profile of the passing electrons with initial positive $v_{\|}$. Figure (b) shows the negative current distribution profile along with the electron orbital distribution profile of the passing electrons with initial negative $v_{\|}$. In this resonance, also a significant amount of positive current distribution appeared outside the LCFS while the entire negative current distribution appeared inside the LCFS. Both the positive and negative currents distributions were decreased at $R = 0.58\,\mathrm{m}$ due to cold resonance. As the minimum initial energies of the resonant electrons were increased while the initial positions of the electrons were approached far from the cold resonance layer, both the positive and the negative current distributions profile were broadened compared with the electron orbital distributions profiles due to the higher energetic electrons with larger drift toroidal velocities.

Figure 5.14 shows the current distribution profile of the equatorial plane current on R contributed by the trapped electrons for the 2nd harmonic relativistic resonant electrons. The trapped electrons contributed both the positive and negative currents. The figure (a) shows both the positive and negative currents distribution profile of the equatorial plane current on R. A significant amount of positive current distribution appeared outside the LCFS while the entire negative current distribution appeared only inside the LCFS.

Figure 5.15 shows the surface-averaged positive and negative currents distributions profiles of the passing electrons and trapped electrons of closed flux surfaces on the square root of the normalized poloidal flux index. Most of the positive current distribution appeared outside the LCFS, while the entire negative current distribution appeared within the LCFS. In addition, the positive current distribution of the trapped electrons also appeared outside the LCFS and the entire the entire negative current distribution appeared within the LCFS.

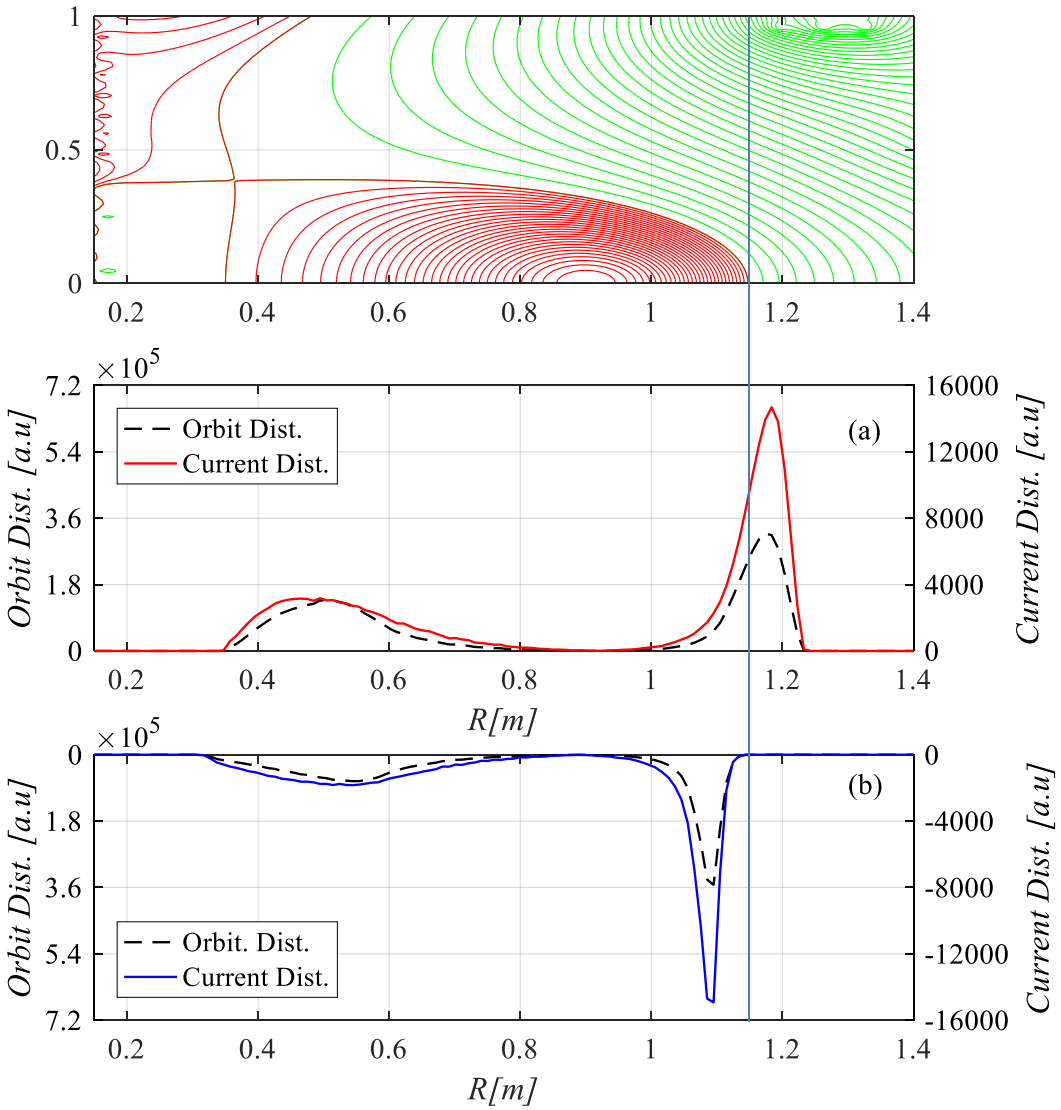

Figure 5.13: The currents distribution profiles along with the electron orbital distributions profiles of the passing electros of the equatorial plane on R for the 2nd harmonic relativistic resonant electrons. The top figure shows the upper part of the closed and opened magnetic surfaces of the equilibrium magnetic configuration, cutting along the equatorial plane. (a) Shows the positive current distribution profiles along with the electron orbital distribution profile of the passing electrons with initial positive $v_{\parallel}$, and (b) shows the negative current distribution profile along with the electron orbital distribution profile of the passing electrons with initial negative $v_{\parallel}$.

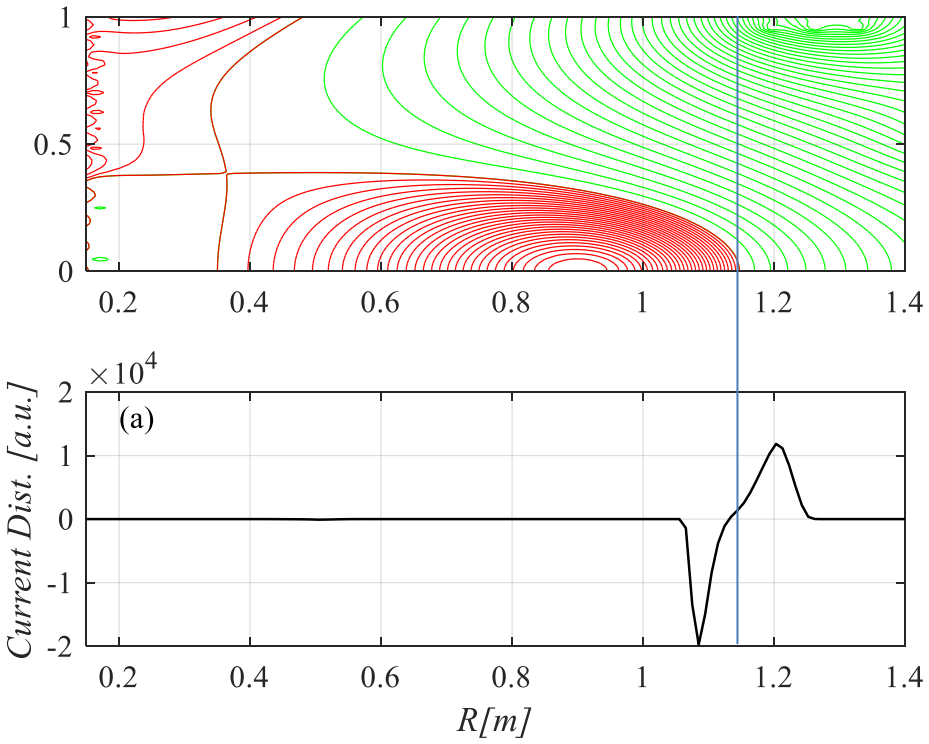

Figure 5.14: The current distribution profile of the equatorial plane current on R contributed by the trapped electrons for the 2nd harmonic relativistic resonant electrons. The top figure shows the upper part of the closed and opened magnetic surfaces of the equilibrium magnetic configuration, cutting along the equatorial plane. (a) Shows both the positive and negative current distribution profile.

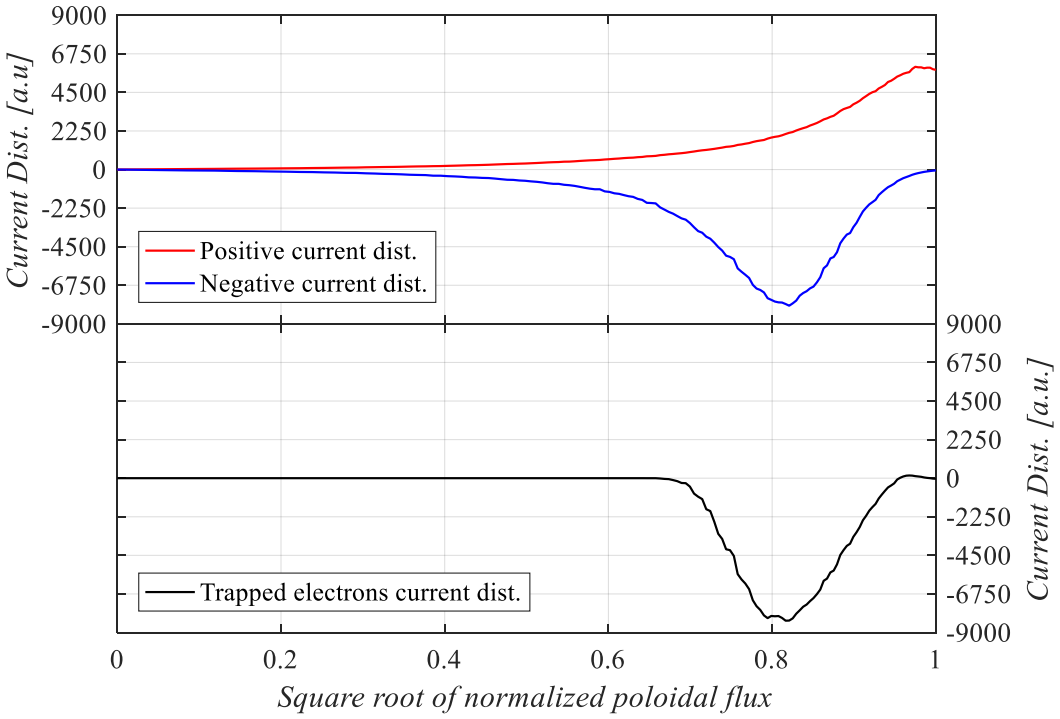

Figure 5.15: The surface-averaged current distribution profiles of the passing electrons and the trapped electrons of closed flux surfaces on the square root of the normalized poloidal flux index for the 2nd harmonic relativistic resonant electrons.

Chapter 6

Summary and Future Scopes

6.1 Summary

The guiding center orbits of the electron cyclotron resonance (ECR) electrons were calculated and analyzed under equilibrium magnetic configuration to consider the current distribution outside the LCFS. A framework with several sets of calculation codes accordingly for various theoretical models was developed with EFIT (Equilibrium Fitting) plasma equilibrium to calculate and analyses guiding center orbits as well as to evaluate orbit current distribution. The plasma equilibrium and shaping were properly taken into account for the orbit analyses and the current evaluation, but the evaluated current was not included in the plasma equilibrium and shaping self-consistently.

The equilibrium magnetic configuration was obtained from the plasma equilibrium solution using 129×129 (129 grid points in the R direction and 129 grid points in the Z direction) spatial resolutions EFIT code. The poloidal flux ψ and toroidal current density of plasma J_T were calculated by the EFIT code on the rectangular grid with the external magnetics for constraint of a discharge that satisfy the model provided by the Grad-Shafranov equation.

The guiding center orbits of the resonant electrons were calculated and analyzed for the 8.2 GHz electron cyclotron heating and current drive (ECH/CD) waves in non-relativistic and relativistic Doppler-shifted ECR. The down-shifted and up-shifted fundamental and second (2^{nd}) harmonic resonances were considered separately. Various parallel and perpendicular velocities to the magnetic field, $v_{||}$ and $v_{\perp}$, were considered from the Doppler-shifted ECR condition for the electrons to be resonant with the ECH waves. The parallel refractive index $N_{||}$ from -1 to $+1$ with step 0.1 was taken into account in the multiple-wall reflection model. The maximum energy of the resonant electrons was restricted at 100 keV and calculated the orbits of those electrons whose initial energies were between 1 to 100 keV. The orbit trajectory of the ECR electron was obtained as contour plot of the resonant electron's energy under the equilibrium magnetic

configuration on the poloidal cross-section. The energy was expressed in terms of magnetic moment and toroidal angular momentum. The energy, magnetic moment, and toroidal angular momentum were conserved in the orbit trajectories. All the resonant and confined electrons' orbits trajectories were obtained for various positions of the coordinates (R,Z), pitch angles and parallel refractive index. The number of the step parameters was more than 5,200000. Depending on the ECR for various conditions, the resonant electrons were travelled both in the parallel and the antiparallel directions to the magnetic field. The resonant electrons with initial positive $v_{\|}$ were travelled in the parallel direction to the magnetic field, while the resonant electrons with initial negative $v_{\|}$ were travelled in the antiparallel direction to the magnetic field.

The orbit current distributions were evaluated from the electrons' orbital distributions along with the drift toroidal velocities, v_{φ} throughout the orbit. The orbital distribution was calculated by the picture-in-cell method where 128×128 cells were prepared by 129×129 gridlines on the (R,Z) plane. Each orbit-segment-element between two intersected gridlines of an orbit and their corresponding cell locations were determined and deposited values in the cells of the cell matrix according to the orbit-segment-element length. This process was repeated for every calculated orbits and finally the total number of all deposited values in the cells of the matrix resulted as the orbital distribution of the resonant electrons. The drift toroidal velocities corresponding to the orbit-segments were calculated from the orbit trajectories. Then the current distributions were evaluated and stored in the cell matrix of J. The electrons with initial positive $v_{\|}$ were contributed positive current while the electrons with initial negative $v_{\|}$ were contributed negative current. The trapped electrons with initial positive and negative $v_{\|}$ were contributed both the positive and negative currents. The direction of the positive current was opposite to the toroidal magnetic field i.e. co-current direction of QUEST plasma current while the direction of the negative current was parallel to the toroidal magnetic field i.e. counter-current direction of QUEST plasma current. The current distribution contour plots on the poloidal cross-section and the current distribution profiles of the equatorial plane current on R, and the surface-averaged current distribution profiles of the closed flux surfaces on the square root of the normalized poloidal flux index were obtained from the J matrix.

Accordingly, this thesis concludes with the following points:

(1) A large number of passing resonant electrons with initial positive $v_{\|}$ starting from the high field side were maintained their orbits outside the LCFS, while all the passing resonant

electrons with initial negative $v_{\|}$ starting from the high field side were maintained their orbits inside the LCFS.

(2) The trapped resonant electrons only being the 2nd harmonic ECR were maintained banana orbits at the low field side of the torus where most of the portions of the banana orbits of positive $v_{\|}$ were placed outside the LCFS.

(3) A significant amount of the positive current by the passing resonant electrons with initial positive $v_{\|}$ appeared outside the LCFS, while the entire negative current by the passing resonant electrons with initial negative $v_{\|}$ appeared inside the LCFS.

(4) The trapped electrons contributed both the positive and negative currents. The positive current portion was distributed outside the LCFS while the negative current portion was evaluated inside the LCFS.

These phenomena were observed for both the non-relativistic and the relativistic ECR as well for the fundamental and the 2nd harmonic ECR.

In the summary, several codes required to evaluate the orbits have been developed with the EFIT code. Various criteria of non-relativistic and relativistic ECR conditions were properly taken into consideration for the orbit analysis. The current contribution appeared outside the LCFS could be qualitatively explained by the developed codes.

Additionally, in thermonuclear magnetic fusion or D-T burning plasmas, about 3.5 MeV energies are carried by the α-particles. Being charged, the α-particles are confined by the magnetic field and then transfer their energy to the plasma. Thus α-particles heat the plasma as an increasing fraction of the total heating. At ignition the external heating can be switched off and the burning process becomes self-sustainable without further heating due to the α-particle heating. Thus α-particles play a vital role in the D-T burning plasmas. However, still a wide range of unsolved theoretical as well as experimental issues remain to solve associate with the role of the α-particles. In order to review the state-of-art and to identify new issues or problems for further research related to α-particles, the developed framework as well as theoretical model and calculation mechanisms for the particle orbits analysis described in this thesis can be applied to the orbits analyses of the α-particles in burning plasma.

6.2 Future Scopes

In this thesis, the analyses of the guiding center orbits and evaluations of the current distributions were carried under equilibrium magnetic configuration which was obtained from the EFIT plasma equilibrium solution. The EFIT plasma equilibrium solution was calculated using EFIT code for the QUEST plasma discharge where 8.2 GHz electron cyclotron heating and current drive (ECH/CD) was used to heat and drive plasma current. Recently, 28 GHz ECH/CD was reinstalled in QUEST. The plasma current was built up to $I_p = 70$ kA fully non-inductively for the 28 GHz discharge. As a next step of this research, EFIT plasma equilibrium solution can be updated for 28 GHz QUEST plasma discharge and orbits analyses and evaluation of current distributions can be performed on the updated equilibrium magnetic configuration.

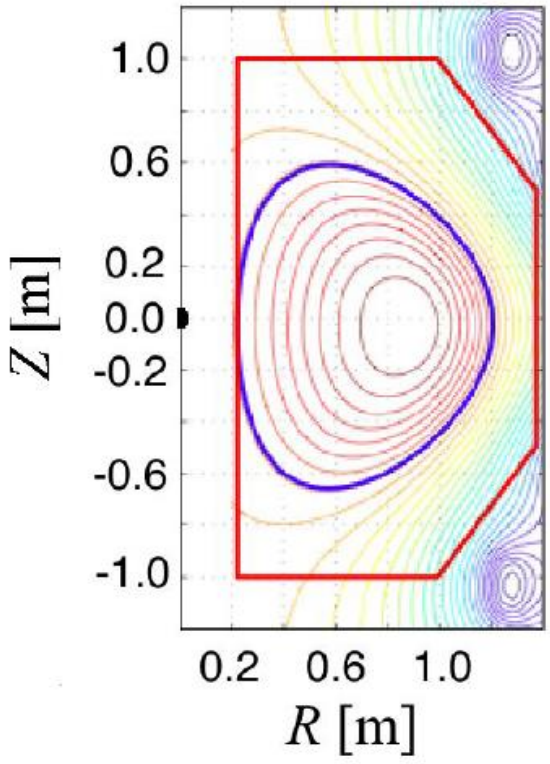

Figure 6.1: Plasma equilibrium solution for the 28 GHz ECH/CD.

List of Publications/Presentations

Peer Reviewed Journals:

1. **Md Mahbub Alam**, Kazuo Nakamura, Hiroshi Idei, Makoto Hasegawa, Kazutoshi Tokunaga, Kuniaki Araki, Kazuaki Hanada, Akihide Fujisawa, Yoshihiko Nagashima, Shoji Kawasaki, Hisatoshi Nakashima, Aki Higashijima, Fan Xia, and Osamu Mitarai. "*Guiding Center Orbit Calculation for Evaluating the Current Density Distributions of the Electrons in Electron Cyclotron Heating on QUEST*." **IEEE Transactions on Plasma Science,** vol. 44, no. 9, pp. 1666-1671, Sep. 2016.

2. **Md Mahbub Alam**, Kazuo Nakamura, Fan Xia, Osamu Mitarai, Makoto Hasegawa, Kazutoshi Tokunaga, Kuniaki Araki, Hideki Zushi, Kazuaki Hanada, Akihide Fujisawa, Hiroshi Idei, Yoshihiko Nagashima, Shoji Kawasaki, Hisatoshi Nakashima, Aki Higashijima, Takahiro Nagata. "*Comparison of current density profiles based on particle orbit-driven current in steady-state plasma on QUEST*." **Fusion Engineering and Design,** vol. 109-111, part B, pp. 1624-1630, Nov. 2015.

3. K. Nakamura, **M. M. Alam**, YZ. Jiang, O. Mitarai, K. Kurihara, Y. Kawamata, M. Sueoka, M. Takechi, M. Hasegawa, K. Tokunaga, K. Araki, H. Zushi, K. Hanada, A. Fujisawa, H. Idei, Y. Nagashima, S. Kawasaki, H. Nakashima, A. Higashijima, T. Nagata, A. Fukuyama. "*Analysis of plasma equilibrium based on orbit-driven current density profile in steady-state plasma on QUEST*." **Fusion Engineering and Design,** vol. 109-111, part B, pp. 1528-1533, Dec. 2015.

4. K. Nakamura, **M. M. Alam**, YZ. Jiang, O. Mitarai, K. Kurihara, Y. Kawamata, M. Sueoka, M. Takechi, M. Hasegawa, K. Tokunaga, K. Araki, H. Zushi, K. Hanada, A. Fujisawa, H. Idei, Y. Nagashima, S. Kawasaki, H. Nakashima, A. Higashijima, T. Nagata, A. Fukuyama. "*Plasma Equilibrium Based on RF-Driven Current Profile without Assuming Nested Magnetic Surfaces on QUEST*", **Fusion Engineering and Design** (Accepted 16 May 2017). http://dx.doi.org/10.1016/j.fusengdes.2017.05.070

5. Idei, Hiroshi; Kariya, Tsuyoshi; Imai, Tsuyoshi; Mishra, Kishore ; Onchi, Takumi; Watanabe, Osamu; Zushi, Hideki; Hanada, Kazuaki; Qian, Jinping; Eiri, Akira; **Alam, Mahbub**; Nakamura, K; Fujisawa, Akihide; Nagashima, Yoshihiko; Hasegawa, Makoto; Matsuoka,

Keisuke; Fukuyama, Atsushi; Kubo, Shin; Shimozuma, Takashi; Yoshikawa, M; Sakamoto, Mizuki; Kawasaki, Shoji; Nakashima, Hisatoshi; Higashijima, Aki; Ide, Shunsuke; Maekawa, Takashi; Takase, Yuichi; Toi, Kazuo. "*Fully non-inductive second harmonic electron cyclotron plasma ramp-up in the QUEST spherical tokamak.*" **Nuclear Fusion** (Accepted)

Non-Reviewed Paper:

1. **Md Mahbub Alam**, Kazuo Nakamura, Fan Xia, Osamu Mitarai, Makoto Hasegawa, Kazutoshi Tokunaga, Kuniaki Araki, Hideki Zushi, Kazuaki Hanada, Akihide Fujisawa, Hiroshi Idei, Yoshihiko Nagashima, Shoji Kawasaki, Hisatoshi Nakashima, Aki Higashijima et al. "*Current density calculation from particle orbit in RF-driven divertor plasma on QUEST*." Proceedings in **2015 IEEE 26th Symposium on in Fusion Engineering (SOFE)**, pp. 1-6. IEEE, 2015.

Conference Presentations:

1. Kazuo Nakamura, **Md. Mahbub Alam**, Fan Xia, Osamu Mitarai, Makoto Hasegawa, Kazutoshi Tokunaga, Kuniaki Araki, Kazuaki Hanada, Akihide Fujisawa, Hiroshi Idei, Yoshihiko Nagashima, Shoji Kawasaki, Hisatoshi Nakashima, Aki Higashijima. "*Shape Reproduction and Particle Orbit in RF-Driven Divertor Plasma on QUEST*", 24th International TOKI Conference (ITC-24), Nov. 4-7, 2014, Ceratopia Toki, Japan.

2. **Md. Mahbub Alam**, Kazuo Nakamura, Fan Xia, Osamu Mitarai, Makoto Hasegawa, Kazutoshi Tokunaga, Kuniaki Araki, Hideki Zushi, Kazuaki Hanada, Akihide Fujisawa, Hiroshi Idei, Yoshihiko Nagashima, Shoji Kawasaki, Hisatoshi Nakashima, Aki Higashijima. "*Particle Orbit in RF-Driven Divertor Plasma on QUEST*." 3rd A3 Foresight Workshop on Spherical Torus (ST), Dec. 15-17, 2014, Kisarazu, Chiba, Japan.

3. Kazuo Nakamura, **Md. Mahbub Alam**, Fan Xia, Yanzheng, Osamu Mitarai, Kenichi Kurihara, Youchi Kawamata, Michiharu Sueoka, Makoto Hasegawa, Kazutoshi Tokunaga, Kuniaki Araki, Hideki Zushi, Kazuaki Hanada, Akihide Fujisawa, Hiroshi Idei, Yoshihiko Nagashima, Shoji Kawasaki, Hisatoshi Nakashima, Aki Higashijima. "*Shape Reproduction in RF-Driven Divertor Plasma on QUEST*." 3rd A3 Foresight Workshop on Spherical Torus (ST), Dec. 15-17, 2014, Kisarazu, Chiba, Japan.

4. **Md. Mahbub Alam**, Kazuo Nakamura, Fan Xia, Osamu Mitarai, Makoto Hasegawa, Kazutoshi Tokunaga, Kuniaki Araki, Hideki Zushi, Kazuaki Hanada, Akihide Fujisawa, Hiroshi Idei, Yoshihiko Nagashima, Shoji Kawasaki, Hisatoshi Nakashima, Aki Higashijima. "*Current Density Calculation from Particle Orbit in RF-Driven Divertor Plasma on QUEST*." 26th IEEE Symposium on Fusion Engineering (SOFE-2015), May 31-June 4, 2015, Austin, Texas, USA.

5. **Md. Mahbub Alam**, Kazuo Nakamura, Fan Xia, Osamu Mitarai, Makoto Hasegawa, Kazutoshi Tokunaga, Kuniaki Araki, Hideki Zushi, Kazuaki Hanada, Akihide Fujisawa, Hiroshi Idei, Yoshihiko Nagashima, Shoji Kawasaki, Hisatoshi Nakashima, Aki Higashijima. "*Simulation of Particle Orbits and the Current Density Calculation in RF-Driven Divertor Plasma on QUEST*." A3 Foresight Summer School, July 20-24, 2015, Chengdu, China.

6. **Md Mahbub Alam**, Kazuo Nakamura, Fan Xia, Osamu Mitarai, Makoto Hasegawa, Kazutoshi Tokunaga, Kuniaki Araki, Hideki Zushi, Kazuaki Hanada, Akihide Fujisawa, Hiroshi Idei, Yoshihiko Nagashima, Shoji Kawasaki, Hisatoshi Nakashima, Aki Higashijima , Takahiro Nagata. "*Comparison of Current Density Profiles Based on Particle Orbit-Driven Current in Steady-State Plasma on QUEST*." 12th International Symposium on Fusion Nuclear Technology (ISFNT-12), September 14 to 18, 2015, Jeju Island, Korea.

7. K. Nakamura, **M. M. Alam**, F. Xia, YZ. Jiang, O. Mitarai, K. Kurihara, Y. Kawamata, M. Sueoka, M. Takechi, M. Hasegawa, K. Tokunaga, K. Araki, H. Zushi, K. Hanada, A. Fujisawa, H. Idei, Y. Nagashima. "*Analysis of Plasma Equilibrium Based on Orbit-Driven current Density Profile in Steady-State Plasma on QUEST*." 12th International Symposium on Fusion Nuclear Technology (ISFNT-12), September 14 to 18, 2015, Jeju Island, Korea.

8. K. Nakamura, **M. M. Alam,** F. Xia, YZ. Jiang, O. Mitarai, K. Kurihara, Y. Kawamata, M. Sueoka, M. Takechi, M. Hasegawa, K. Tokunaga, K. Araki, H. Zushi, K. Hanada, A. Fujisawa, H. Idei, Y. Nagashima, S. Kawasaki, H. Nakashima, A. Higashijima, T. Nagata, A. Fukuyama. "*Analysis of Plasma Equilibrium Based on Orbit-Driven current Density Profile in Steady-State Plasma on QUEST*." Workshop at NIFS, August 18-19, 2015, Toki, Gifu, Japan.

9. **Md Mahbub Alam**, Kazuo Nakamura, Makoto Hasegawa, Fan Xia, Osamu Mitarai, Kazutoshi Tokunaga, Kuniaki Araki, Hideki Zushi, Kazuaki Hanada, Akihide Fujisawa, Hiroshi Idei, Yoshihiko Nagashima, Shoji Kawasaki, Hisatoshi Nakashima, Aki Higashijima, Takahiro Nagata. "*Real-Time Display System of the Equilibrium Reconstruction for Long*

Time Discharge in QUEST." 25th International Toki Conference (ITC-25), November 3-6, 2015, Toki-city, Gifu, JAPAN.

10. **Md Mahbub Alam**, Kazuo Nakamura, Hiroshi Idei, Makoto Hasegawa, Kazutoshi Tokunaga, Kuniaki Araki, Kazuaki Hanada, Akihide Fujisawa, Yoshihiko Nagashima, Shoji Kawasaki, Hisatoshi Nakashima, Aki Higashijima, Fan Xia, and Osamu Mitarai. "*Guiding Center Orbits Calculation for Evaluating the Current Density Distribution of the Electrons in Electron Cyclotron Heating on QUEST*." Schevchenko Workshop, 24-25 March, 2016, QUEST Building, Kyushu University, Fukuoka, Japan.

11. **Md Mahbub Alam**, Hiroshi Idei, Kazuo Nakamura, Kazuaki Hanada, Akihide Fujisawa, Yoshihiko Nagashima, Makoto Hasegawa , Kuzmin Arseniy, Ohwada Hiroaki, Fan Xia, Osamu Mitarai and QUEST team. "*Evaluation of Surface Averaged Current Density Distribution of Orbit-driven Current in Electron Cyclotron Heating on QUEST*." 4th A3 Foresight Summer School and Workshop on Spherical Torus (ST), Kyushu University (Chikushi Campus), Fukuoka, Japan, Aug. 2-5, 2016.

12. **Md Mahbub Alam**, Hiroshi Idei, Kazuo Nakamura, Kazuaki Hanada, Akihide Fujisawa, Yoshihiko Nagashima, Makoto Hasegawa , Kuzmin Arseniy, Ohwada Hiroaki, Fan Xia, Osamu Mitarai and QUEST team. "*Evaluation of Orbit-driven Current in Electron Cyclotron Heating on QUEST*." 8th Korea-Japan Seminar on Advanced Diagnostics for Steady-State Fusion Plasmas, August 24-27, 2016, Busan, Korea

Bibliography

[1]. M. Asif and T. Muneer, "Energy supply, its demand and security issues for developed and emerging economies," *Renewable and Sustainable Energy Reviews*, vol. 11, no. 7, pp. 1388–1413, Sep. 2007.

[2]. G. Verbong and F. Geels, "The ongoing energy transition: Lessons from a socio-technical, multi-level analysis of the Dutch electricity system (1960–2004)," *Energy Policy*, vol. 35, no. 2, pp. 1025–1037, Feb. 2007.

[3]. N. Armaroli and V. Balzani, "The Future of Energy Supply: Challenges and Opportunities," *Angewandte Chemie International Edition*, vol. 46, no. 1-2, pp. 52–66, Nov. 2006.

[4]. G. McCracken and P. Stott, "Man-Made Fusion," in *Fusion: the energy of the universe*, Amsterdam: Elsevier, 2012.

[5]. J. Wesson, "Fusion," in *Tokamaks*, Oxford: Oxford University Press, 2004.

[6]. J. P. Freidberg, "Fusion and world energy," in *Plasma physics and fusion energy*, Cambridge: Cambridge University Press, 2008.

[7]. Y. Wu, "Conceptual design and testing strategy of a dual functional lithium–lead test blanket module in ITER and EAST," *Nuclear Fusion*, vol. 47, no. 11, pp. 1533–1539, Oct. 2007.

[8]. V.P. Smirnov, "Tokamak foundation in USSR/Russia 1950–1990," *Nuclear Fusion*, vol. 50, no. 1, p. 014003 (8pp), Dec. 2009.

[9]. M. Kikuchi, "A Review of Fusion and Tokamak Research Towards Steady-State Operation: A JAEA Contribution," *Energies*, vol. 3, no. 11, pp. 1741–1789, Oct. 2010.

[10]. "ITER Timeline," *ITER*. [Online]. Available: https://www.iter.org/proj/inafewlines. [Accessed: 08-Feb-2017].

[11]. F. Troyon, R. Gruber, et al., "MHD-Limits to Plasma Confinement," *Plasma Physics and Controlled Fusion*, vol. 26, no. 1A, pp. 209–215, Jan. 1984.

[12]. "ITER EDA Agreement and Protocol 2," ITER Document Series No. 5, IAEA, Vienna, 1994.
[Online].Available:http://www.iaea.org/inis/collection/NCLCollectionStore/_Public/25/064/25064794.pdf. [Accessed: 02-March-2017].

[13]. Y-K. M. Peng and D.J. Strickler, "Features of spherical torus plasmas," *Nuclear Fusion*, vol. 26, no. 6, pp. 769–777, Jan. 1986.

[14]. Z. Gao, “Compact magnetic confinement fusion: Spherical torus and compact torus,” *Matter and Radiation at Extremes*, vol. 1, no. 3, pp. 153–162, May 2016.

[15]. Y-K. M. Peng, “The physics of spherical torus plasmas,” *Physics of Plasmas*, vol. 7, no. 5, pp. 1681–1692, Apr. 2000.

[16]. M. Ono, et al., "Exploration of spherical torus physics in the NSTX device," *Nuclear Fusion*, vol. 40, no.3Y, p. 557, Mar. 2000.

[17]. B. Lloyd, et al., "Overview of recent experimental results on MAST," *Nuclear fusion*, vol. 43, no. 12, p. 1665, Dec. 2003.

[18]. A. Sykes, "Overview of recent spherical tokamak results," *Plasma physics and controlled fusion*, vol. 43, no.12A, p. A127, Nov. 2001.

[19]. T. Watari, "Plasma Heating and Current Drive," *Frontier of Physics in Fusion-Relevant Plasmas: Proceedings of the Asian Science Seminar*, World Scientific, 1998.

[20]. M. Greenwald, et al., "Priorities, Gaps and Opportunities: Towards A Long-Range Strategic Plan For Magnetic Fusion Energy. 2007," A Report to the USDoE Fusion, Energy Sciences Advisory Committee, October 2007.

[21]. J.E. Menard, L. Bromberg, et al., “Prospects for pilot plants based on the tokamak, spherical tokamak and stellarator,” *Nuclear Fusion*, vol. 51, no. 10, p. 103014, Aug. 2011.

[22]. R. I. Pinsker, “Introduction to wave heating and current drive in magnetized plasmas,” *Physics of Plasmas*, vol. 8, no. 4, pp. 1219–1228, Apr. 2001.

[23]. N. J. Fisch, "Methods of Radio-Frequency Current Drive," *Fusion Science and Technology*, vol. 65, no. 1, pp.1-9, Jan. 2014.

[24]. S. J. Wukitch, "RF Sustainment Simulation Opportunities for Steady State Fusion Reactor Plasmas," [Online]. Available: https://burningplasma.org/resources/ref/Workshops2015/IS/B_wukitch_s.pdf

[25]. M. Uchida, et al., "Start-up of Spherical Torus by ECH without Central Solenoid in the LATE Device," *Journal of Plasma and Fusion Research*, vol. 80, no. 2, pp. 83-84, 2004.

[26]. C. B. Forest, Y. S. Hwang, et. al., “Internally generated currents in a small-aspect-ratio tokamak geometry,” *Physical Review Letters*, vol. 68, no. 24, pp. 3559–3562, Jun. 1992.

[27]. R. Majeski, et al., “Ion cyclotron range of frequency experiments in the Tokamak Fusion Test Reactor with fast waves and mode converted ion Bernstein waves,” *Physics of Plasmas*, vol. 3, no. 5, pp. 2006–2012, May 1996.

[28]. T. Shinya, Y. Takase, et al., “Non-inductive plasma start-up experiments on the TST-2 spherical tokamak using waves in the lower-hybrid frequency range,” *Nuclear Fusion*, vol. 55, no. 7, p. 073003, Jun. 2015.

[29]. K. Hanada, et al., “Steady-State Operation Scenario and the First Experimental Result on QUEST,” *Plasma and Fusion Research*, vol. 5, p. S1007, 2010.

[30]. S. Tashima, et al., “Role of energetic electrons during current ramp-up and production of high poloidal beta plasma in non-inductive current drive on QUEST,” *Nuclear Fusion*, vol. 54, no. 2, p. 023010 (11pp), Feb. 2014.

[31]. M. Ishiguro, K. Hanada, et al., “Non-inductive current start-up assisted by energetic electrons in Q-shu University experiment with steady-state spherical tokamak,” *Physics of Plasmas*, vol. 19, no. 6, p. 062508(11pp), Jun. 2012.

[32]. H. Idei et al., “Fully non-inductive current drive experiments using 28 GHz and 8.2 GHz electron cyclotron waves in QUEST,” Proc. 25th Fusion Energy Conf., Saint Petersburg, Russia, EX/P1-38, 13 -18 October 2014.

[33]. Onchi, Takumi, et al. "Non-inductive current built-up by local electron cyclotron heating and current drive with a 28 GHz focused beam on QUEST." *APS Meeting Abstracts*. 2016.

[34]. K. Nakamura, et al., “Shape Reconstruction of RF-Driven Divertor Plasma on QUEST,” *IEEE Transactions on Plasma Science*, vol. 42, no. 9, pp. 2309–2312, Sep. 2014.

[35]. L. L. Lao, et al., “Reconstruction of current profile parameters and plasma shapes in tokamaks,” *Nuclear Fusion*, vol. 25, no. 11, pp. 1611–1622, 1985.

[36]. L. Jia-Rong, “Review of the Equilibrium Fitting for Non-Circular Tokamak,” *Plasma Science and Technology*, vol. 4, no. 2, pp. 1183–1192, 2002.

[37]. J. R. Ferron, et al., “Real time equilibrium reconstruction for tokamak discharge control,” *Nuclear Fusion*, vol. 38, no. 7, pp. 1055–1066, 1998.

[38]. J. Havlicek and J. Urban, "A magnetic equilibrium reconstruction in tokamak," in *WDS’07 Proceedings of Contributed Papers Part II—Physics of Plasmas and Ionized Media*, pp. 234-239, 2007.

[39]. K. Nakamura, et al., "Shape reconstruction of RF-driven divertor plasma on QUEST," *Proceedings of 2013 IEEE 25th Symposium on Fusion Engineering (SOFE)*, IEEE, 2013.

[40]. H. Idei, “Fully non-inductive second harmonic electron cyclotron plasma ramp-up in the QUEST spherical tokamak,” *Nuclear Fusion*. [Accepted]

[41]. F. F. Chen, “Single-particle motions,” in *Introduction to plasma physics and controlled fusion*, vol. 1, New York: Springer, 1984.

[42]. G. N. Sabri and T. Benouaz, “Study of energy transfer by electron cyclotron resonance in tokamak plasma,” *Energy Procedia*, vol. 6, pp. 194–201, Jun. 2011.

[43]. M. M. Alam, et al., “Comparison of current density profiles based on particle orbit-driven current in steady-state plasma on QUEST,” *Fusion Engineering and Design*, vol. 109-111, pp. 1624–1630, Nov. 2016.

[44]. V. Erckmann and U. Gasparino, “Electron cyclotron resonance heating and current drive in toroidal fusion plasmas,” *Plasma Physics and Controlled Fusion*, vol. 36, no. 12, pp. 1869–1962, 1994.

[45]. M. M. Alam, et al., “Guiding Center Orbit Calculation for Evaluating the Current Density Distributions of the Electrons in Electron Cyclotron Heating on QUEST,” *IEEE Transactions on Plasma Science*, vol. 44, no. 9, pp. 1666–1671, Sep. 2016.

Acknowledgements

First and foremost I would like to express my special thanks to my advisors Prof. Hiroshi Idei and Prof. Kazuo Nakamura for their continuous supervision and guideline of my doctoral study and related research. Their contribution of encouragements, motivations, ideas and times are highly appreciable and build a deep foundation of knowledge and research capabilities for me. During their supervision era, I get the real art of the research and knowledge that makes me thirsty to find new knowledge and research issues. I am very thankful to them for their excellent and remarkable guidance and for successfully completing of my doctoral study and research.

Besides my advisors, I would like to express my thanks to Prof. Kazuaki Hanada, Prof. Akihide Fujisawa, Prof. Yoshihiko Nagashima, Prof. Makoto Hasegawa, Prof. Osamu Mitarai, Dr. Takumi Onchi and all of the QUEST members for their continuous guidelines and support for my study and research. They always open opportunities to me to acquire new knowledge and various dimension of my researches. Without their precious support, it would be very difficult to conduct this research.

I would also like to express my sincere thanks to the honorable Prof. Kiichiro Uchino and Prof. Shigeru Inagaki for their insightful comments and valuable guidelines to widen my research from various perspectives. Their kind commentaries help me to upgrade my thesis.

I thank to all of my labmates for their time, suggestions and for participating a lot of discussion concerning my research and study during my study period. Their tremendous supports help to continue my study and research. Sometimes they help me as interpreters, sometimes as instructors, sometimes as a companion while working at night. I am very grateful to all of them.

Finally, I would like to give my special thanks to my parents, my wife Mst. Tania Rahman and my sweetest two little kids Tasneem Alam and Tahmeed Alam for their support and accompany. They give me a lot of enjoyable moments and refresh my mind to continue my study and research with effective manner.

Md Mahbub Alam
Kyushu University
August, 2017